Summary of Large-Scale C-shaped Reinforced Concrete Wall Tests

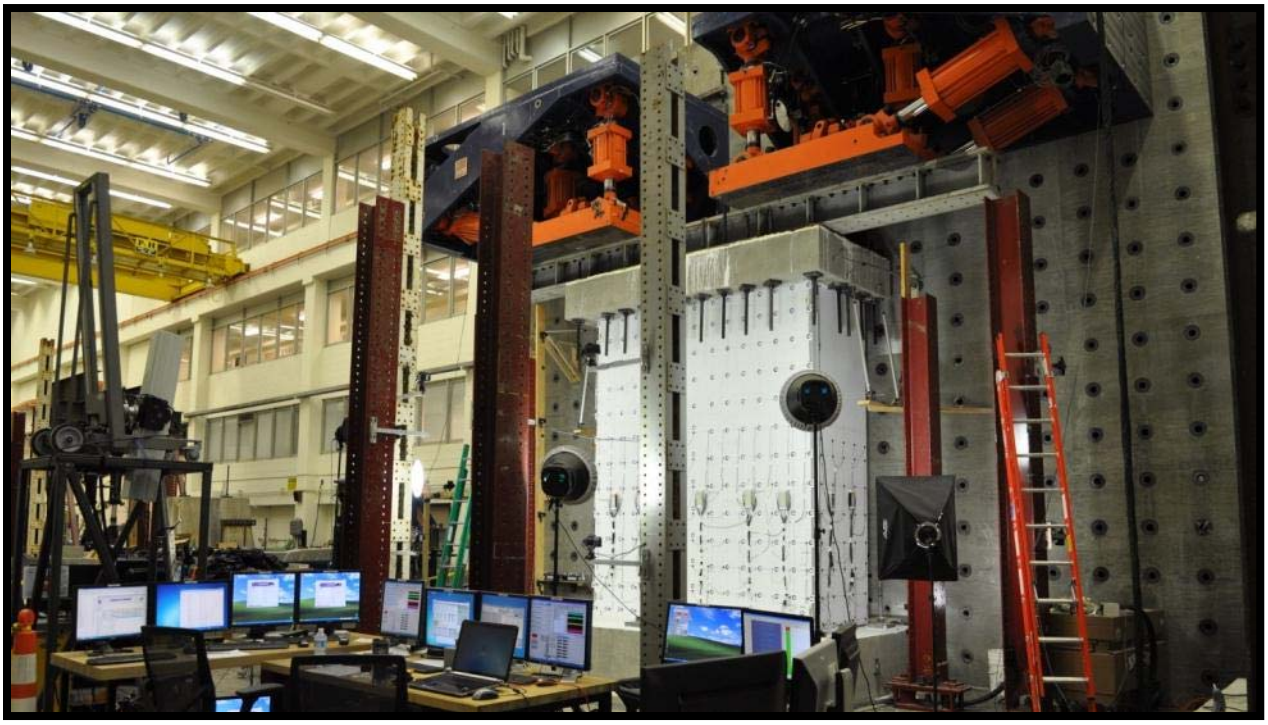

Anahid Behrouzi, Tufts University
Andrew Mock, SCA Consulting Engineers
Dr. Laura Lowes, University of Washington
Dr. Dawn Lehman, University of Washington
Dr. Daniel Kuchma, Tufts University

Funding provided by the **National Science Foundation** and the **Charles Pankow Foundation**

CHARLES PANKOW
FOUNDATION

Contents

List of Figures

List of Tables

1. Introduction

Flexural concrete walls (i.e., walls the yield in flexural prior to failure) are used commonly as the lateral load resisting system for mid- and high-rise buildings on the West Coast. They are relatively stiff under service-level loading, can take on various configurations to accommodate architectural constraints, and are generally assumed to exhibit ductile response under severe earthquake loading. Despite heavy reliance on concrete walls, relatively little research has been done to investigate the earthquake performance of walls with modern design details. Few data exist characterizing the performance of modern walls under variable levels of earthquake loading or the impact of various design parameters on this performance. Few data exist to support evaluation and validation of numerical models for modern walls.

In 2004 a research study funded by the National Science Foundation (NSF), through the Network for Earthquake Engineering Simulation Research (NEESR) program, was initiated to investigate the earthquake performance of slender modern walls. This study is being conducted primarily by faculty and graduate students at the Universities of Washington and Illinois, with experimental testing conducted using the NSF-funded NEES laboratory at the University of Illinois, Urbana-Champaign (UIUC). The objectives of this study are to generate experimental data characterizing the seismic response and performance of modern concrete walls, develop numerical models for simulating wall response to support design and research, and develop recommendations for performance-based seismic design of these systems.

The NSF-funded study included experimental testing of planar rectangular walls, a planar coupled wall, and a C-shaped wall, with experimental testing limited to unidirectional lateral loading and constant axial loading. In 2009 the Charles Pankow Foundation (CPF) provided supplemental funding to expand the scope of this study to include investigation of the impact of bidirectional loading on the earthquake performance of isolated C-shaped walls and C-shaped walls in coupled core-wall systems.

This document presents the results of the three C-shaped wall tests conducted as part of the NSF and CPF funded study. All three specimens had nominally the same design. The specimens were designed to represent C-shaped walls in a coupled core-wall system in a modern mid-rise building. Specifically, specimens represented the bottom three stories of a C-shaped wall in a ten-story core-wall building; loads were applied to the top of the specimen to achieve a load pattern at the base of the specimen representative of that which would develop in the ten-story building. All three specimens were subjected to quasi-static cyclic lateral loading in combination with axial loading. The first specimen, identified as Wall 6 of the NSF-CPF project, was subjected to unidirectional lateral loading in the direction of the web of the C-shaped wall and a constant axial load. The second specimen, Wall 7, was subjected to a cruciform lateral load pattern (i.e. loading in the direction of the web of the wall followed by loading in the direction of the wall flanges) as well as bidirectional lateral loading and a constant axial load. The third specimen, Wall 8, was subjected to a cruciform lateral load pattern, bidirectional loading and varying axial load. For Wall 8, a constant axial load was applied when the wall was subject to lateral loading in the direction of the web of the wall; a varying axial load was applied when the wall was subjected to lateral loading in the direction of the wall flanges to simulate the variation in axial load resulting from coupling action in the core-wall system.

The response of test specimens was monitored using multiple instrumentation systems. Multiple fixed and roaming still cameras were used to document damage. A close range photogrammetric system and

a Nikon metrology / Krypton system were used to generate displacement field data. Displacement transducers were used to measure specimen deformation and specimen displacement. External concrete strain gages and embedded steel strain gages were used to monitor local strains. Load cells were used to monitor applied loads. This report employs data from load cells and displacement transducers as well as still camera images to characterize wall behavior and provide a preliminary assessment of performance. In the future, data from other instrumentation systems will be employed to refine the preliminary characterization and performance assessment. All data will be archived and made available to the public via NEEShub (http://www.neeshub.org).

The presentation of the C-shaped wall tests is organized as follows. Section 2 presents the specimen design and construction. Section 3 presents material data for the concrete and steel used in specimen construction. Section 4 presents the test setup and the loading protocol used for the tests. Section 5 presents the instrumentation systems and data collection protocol. Section 6, 7, and 8 presents results for the individual wall tests. Section 9 compares the observed behavior of the three specimens. Section 10 presents preliminary conclusions of the experimental investigation.

2. Specimen design and construction

A total of three C-shaped wall specimens were tested. The specimens were nominally identical in design, with the same geometry and reinforcement layout; differences in the specimens resulted solely from construction and material properties. The specimens were subjected to different load patterns in the laboratory, as discussed in Chapter 4. The following sections describe the design and construction of the specimens.

2.1. Specimen design

The C-shaped wall specimens were designed to represent the C-shaped walls in a coupled core wall system in a modern ten-story building. The design process was as follows (1) size walls to represent modern construction on the West Coast, (2) assume walls will carry the maximum shear stress allowed by the ACI 318-08 $\left(V_n = 8\sqrt{f_c}A_{cv}\right)$, (3) determine required flexural strength at the base of the wall given a base shear demand of $\varphi 8\sqrt{f_c}A_{cv}$, assuming the ASCE 7-07 equivalent lateral force (ELF) distribution is employed for design, and assuming a degree of coupling (percentage of total base moment resulting from coupling action) of approximately 50%, (4) design horizontal reinforcement to achieve $V_n = 8\sqrt{f_c}A_{cv}$, and (5) detail boundary element confining reinforcement per ACI 318-08. The following paragraphs provide a detailed discussion of this process. A nominal compressive strength for concrete of 5 ksi and a nominal yield strength for reinforcing steel of 60 ksi were used.

The full-scale dimensions for the wall specimens were determined considering (1) the average dimensions found from a review of 13 walled buildings designed for construction on the West Coast from 1991 through 2007 (details of this building inventory review are provided in Turgeon 2011 and Mohr 2009), (2) input from practicing engineers, (3) geometry and loading constraints of the UIUC NEES facility, and (4) the configuration of other wall specimens tested as part of the NSF-CPF project (www.nees.org/project/104). The full-scale wall had 12.0 ft. story heights, a 30.0 ft. total length, 12.0 ft. long flanges, and was 18.0 in. thick. Figure 2.1 shows dimensions for the 1/3-scale specimen tested in the laboratory at UIUC.

C-shaped wall specimens were designed for the maximum shear stress demand allowed by the ACI Code; this was considered to represent a plausible upper bound for modern construction. A review 13

walled buildings designed for construction on the West Coast (Stringer 2006) indicated that large shear stress demands can develop in walls if the walls yield in flexure at the base and the earthquake load distribution is approximately equal to the equivalent lateral load distribution defined in ASCE 7. Additionally, analyses of walled buildings subjected to earthquake loading (Birely 2012, Pugh 2012, Brown et al., 2006) indicate that nonlinear wall response may result in the effective height of the lateral load distribution dropping well below that of the ASCE 7 ELF distribution and, thus, the maximum shear demand increasing beyond that associated with the ASCE 7 ELF distribution. Finally, input from practicing engineers indicated that it is not uncommon for shear stress capacities in mid- to high-rise walls to reach the maximum allowed by the ACI Code.

With the base shear strength of the wall defined as $V_n = 8\sqrt{f_c}A_{cv}$, the base shear stress demand was defined per ACI 318-08 as $V_u = \varphi 8\sqrt{f_c}A_{cv} = 4.8\sqrt{f_c}A_{cv}$ with $\varphi = 0.6$ for walls that are not capacity designed. Assuming the ASCE 7 ELF distribution, the base moment demand is defined as $M_u = V_u H_{eff} = 0.71 V_u H$ where H is the total building height and the 0.71 factor follows from the ASCE ELF distribution for a building of uniform mass and stiffness. For loading in the direction of the web of the wall, the wall was designed such that $\varphi M_n > M_u$. An axial load due to gravity loading of $0.05 f_c A_g$ was assumed; this is less than the axial load applied for previous walls tested as part of the NSF-CPF project but ensured that wall capacity would not exceed the capacity of the UIUC laboratory equipment. As is common in modern construction, wall longitudinal reinforcement was arranged with heavily reinforced boundary elements and lightly reinforced interior elements.

For loading in the direction of the wall flanges, coupling between the two C-shaped wall piers comprising the core-wall system was considered. For a coupled wall system subjected to lateral loading, activation of the coupling beams that link the individual wall piers results in axial tensile loading of one wall pier and axial compressive loading of the other wall pier. Total base moment is the sum of the moment due to the axial force couple and the base moments that develop in the individual wall piers. Harries (2001) recommends that to achieve desirable performance from a coupled-wall system the degree of coupling, which is defined as the percentage of the total base moment carried by the tension-compression couple, be less than 55%. Here a target degree of coupling of 50% was used for design. Thus, flexural strength for lateral loading in the direction of the wall webs was designed using the same process as was used in the orthogonal direction, but with wall reinforcement designed for only 50% of the total base moment.

To complete the wall designs, horizontal reinforcement was designed to achieve $V_n = 8\sqrt{f_c}A_{cv}$ and boundary element confinement was designed per ACI 318-08. Figure 2.1 shows the reinforcement layout. Figure 2.2 and Figure 2.3 show boundary element details for Wall 6 and Walls 7 and 8, respectively. An error in construction of Wall 6 resulted in failure to place a required hook in the boundary element (Figure 2.2). This error was not expected to significantly affect the response of Wall 6, which was loaded such that the boundary element in question was not subjected to large compressive demands; this error was corrected in construction of Walls 7 and 8 (Figure 2.3), as these walls were loaded in such a way that the boundary element in question was subjected to large compressive demands. An error in construction of Wall 6 also resulted in all boundary element confining reinforcement being spaced vertically at 2.25 in. rather the ACI Code required maximum spacing of 2.0 in.; this error was not corrected in construction of Walls 7 and 8 as it was not expected to significantly affect response and to preserve consistency in specimen design.

Figure 2.4 shows a schematic of the wall footing and wall. The footing was 14 ft. by 8.75 ft. by 2 ft. and heavily reinforced with two horizontal mats of #4 bars and vertical #4 bars. The footing was post-tensioned to the strong floor with approximately 100 kips per point of anchorage. A void was left for each post-tensioning rod using PVC tubing with spiral reinforcement in the surrounding concrete. In addition, two lifting ducts were left open through the depth of the footing to allow the specimen to be lifted into place using an overhead crane.

The wall cap was constructed similarly to the footing using two heavily reinforced mats of #4 horizontal and vertical bars. To provide for connection to the loading device, PVC tubing was again used to leave voids for post-tensioning rods. The wall cap is 18 inches high. A schematic drawing of the cap is shown in Figure 2.5.

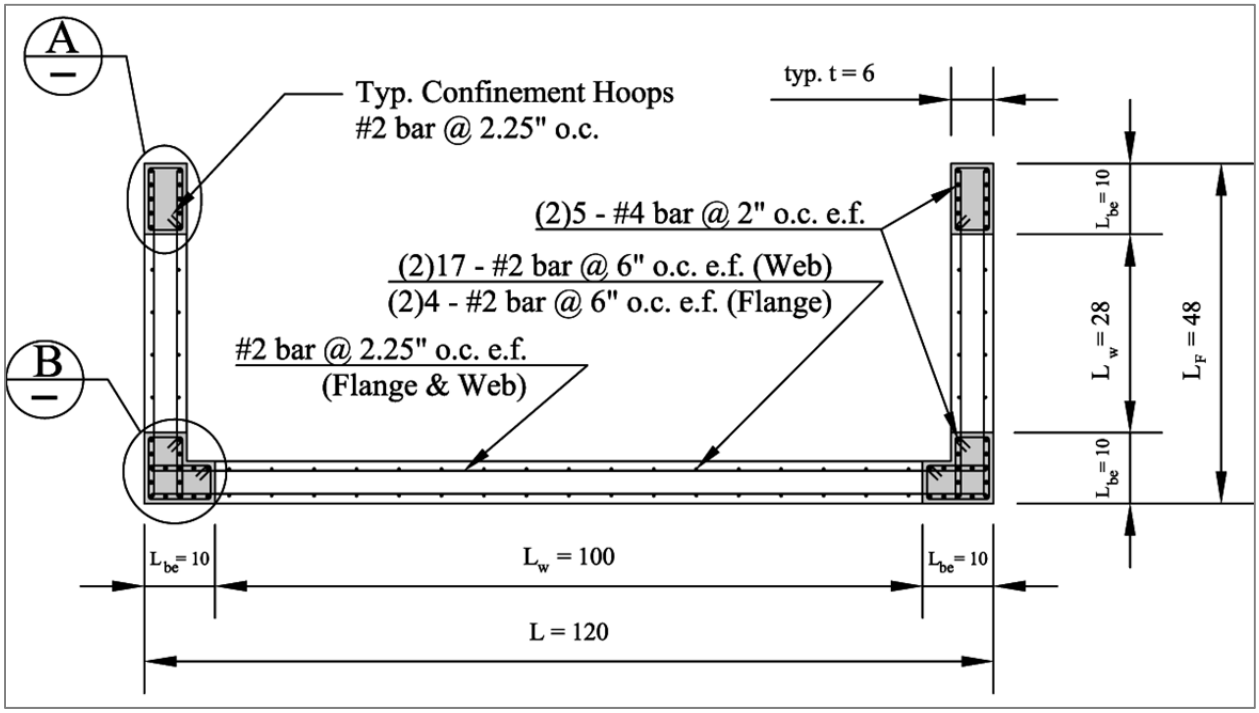

Figure 2.1: Wall 6/7/8 overall wall geometry and reinforcing (dimensions are provided in inches)

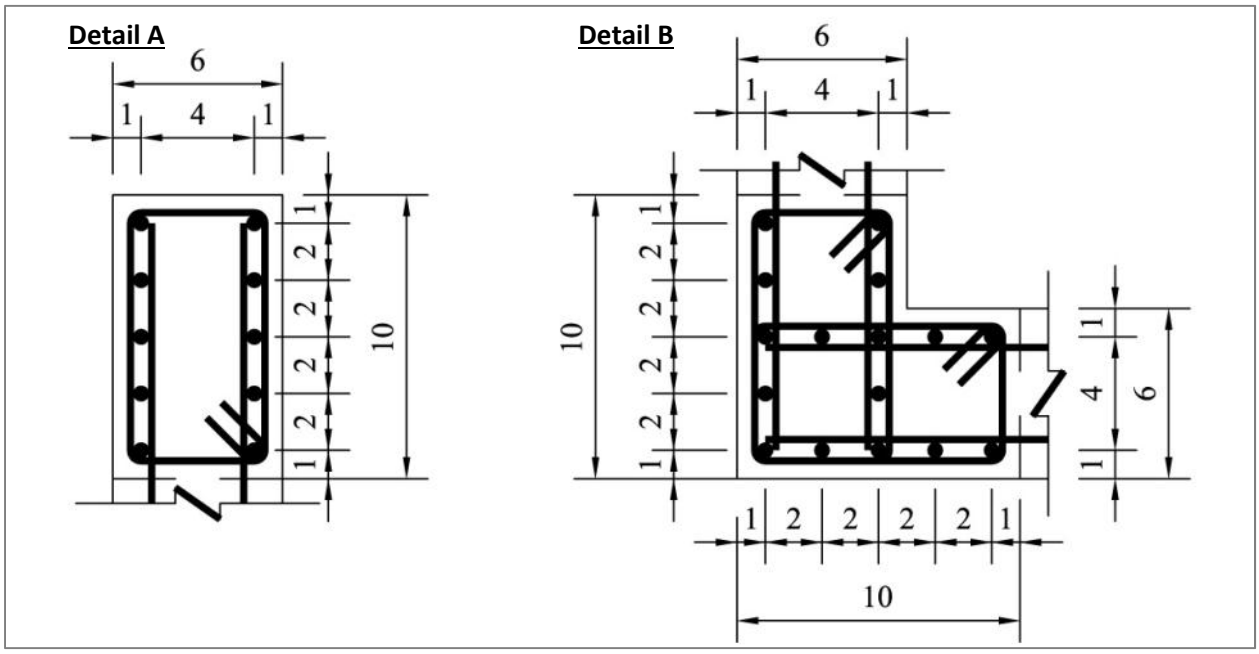

Figure 2.2: Wall 6 boundary element details without hooks (dimensions are provided in inches)

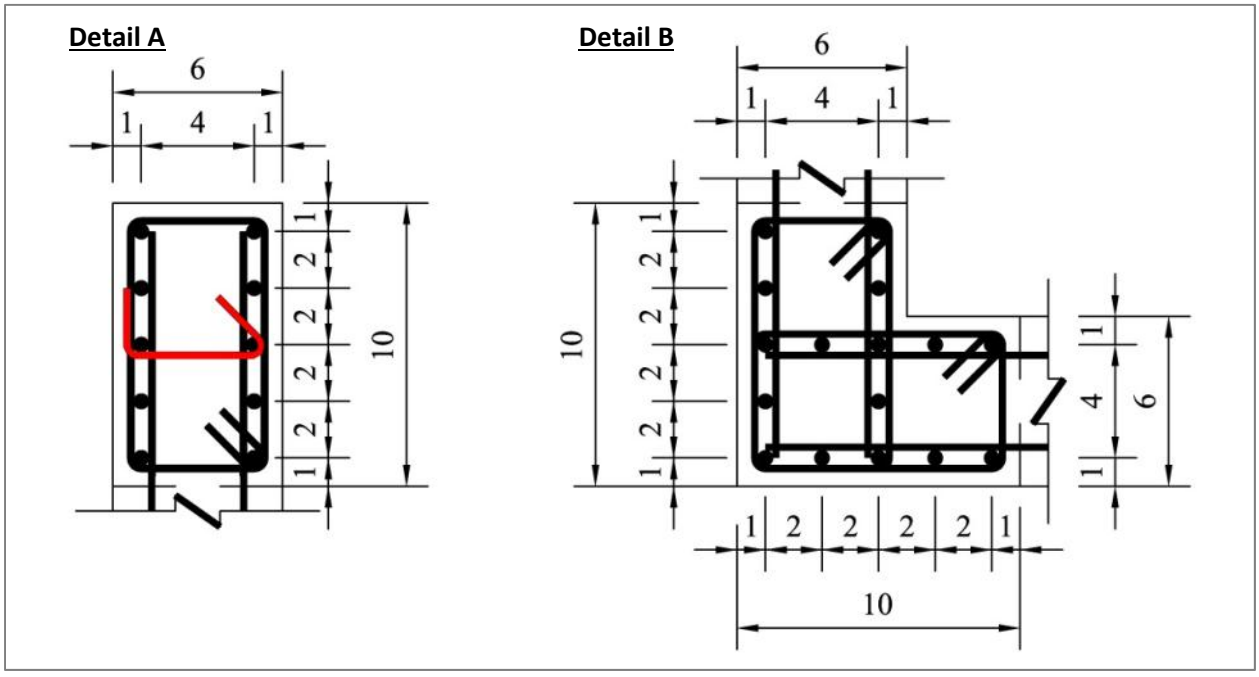

Figure 2.3: Wall 7/8 boundary element details with hooks (dimensions are provided in inches)

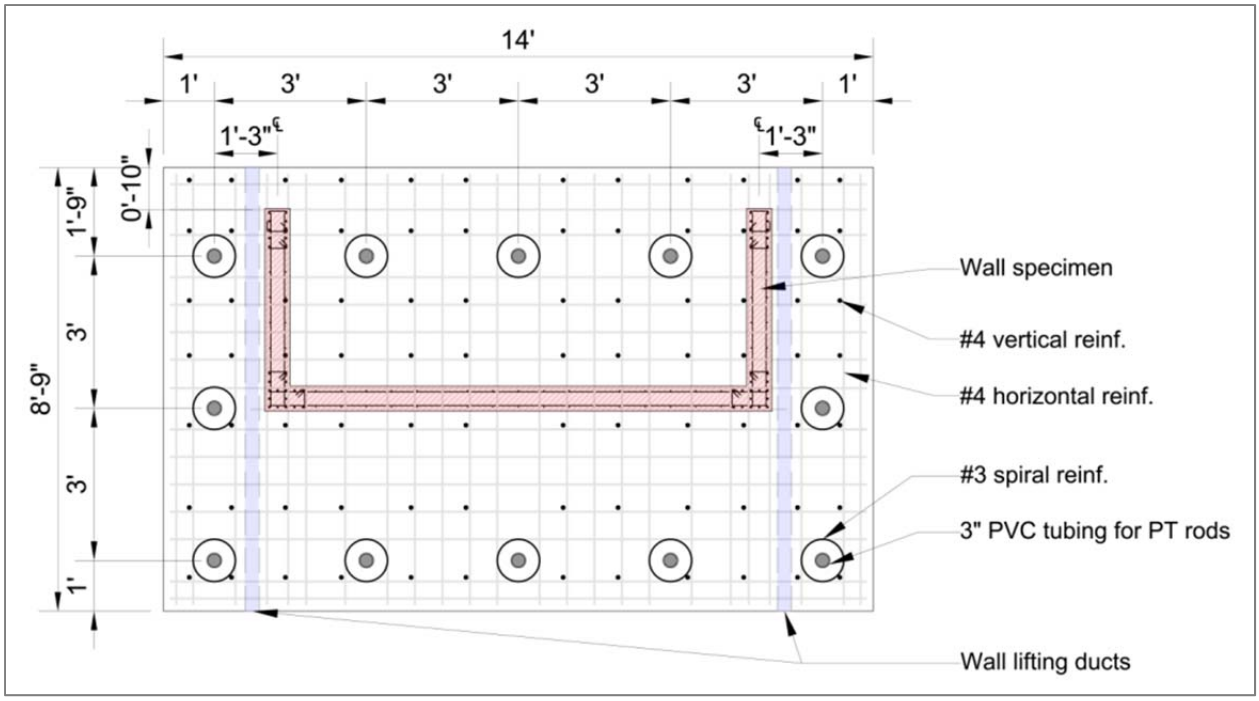

Figure 2.4: Footing construction drawing

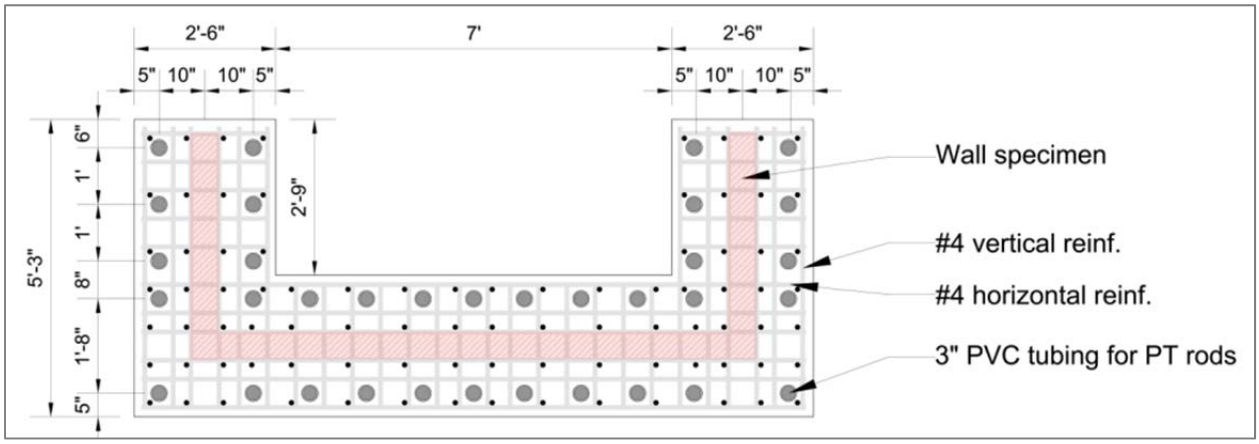

Figure 2.5: Cap construction drawing

2.2. Construction process

Construction and casting of the three wall specimens was completed at UIUC. The foundation was constructed by machine shop employees using wooden formwork, tied rebar mats and PVC tubing as previously described. The longitudinal rebars for the wall specimen were placed continuous from the bottom of the footing through the specimen and terminating in the wall cap without splice. The wall specimen rebar cage was constructed and tied by students in the laboratory as shown in Figure 2.6. Steel formwork was used to maintain the six-inch thickness and cover distances to the reinforcing bars. The wall cap was constructed similar to the footing using wooden formwork, tied rebar mats and PVC tubing as shown in Figure 2.8. The concrete was cast in three separate pours (foundation, specimen and cap) after completing each respective stage of the process. Casting of the wall specimen in pictured in Figure 2.7

Figure 2.6: Near completion of Wall 8 rebar cage

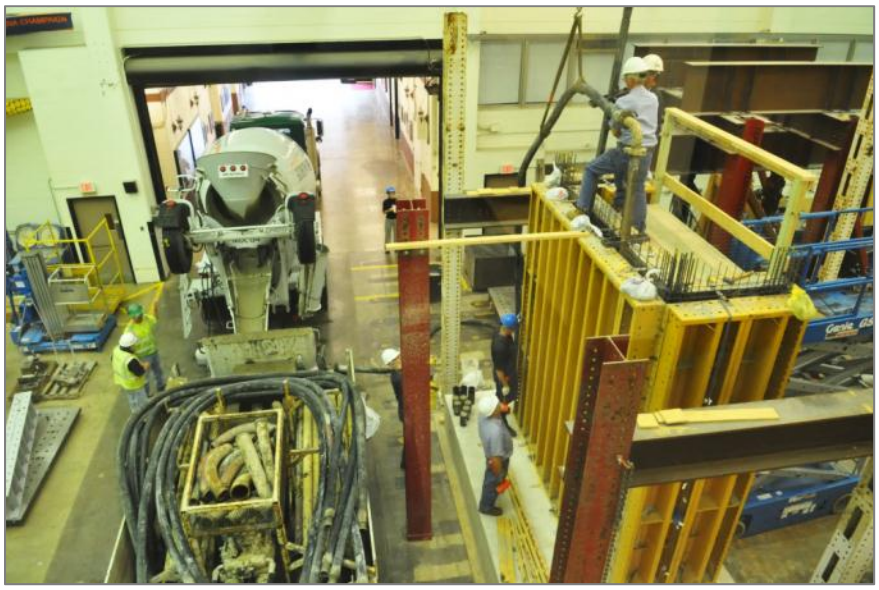

Figure 2.7: Casting of Wall 8 specimen

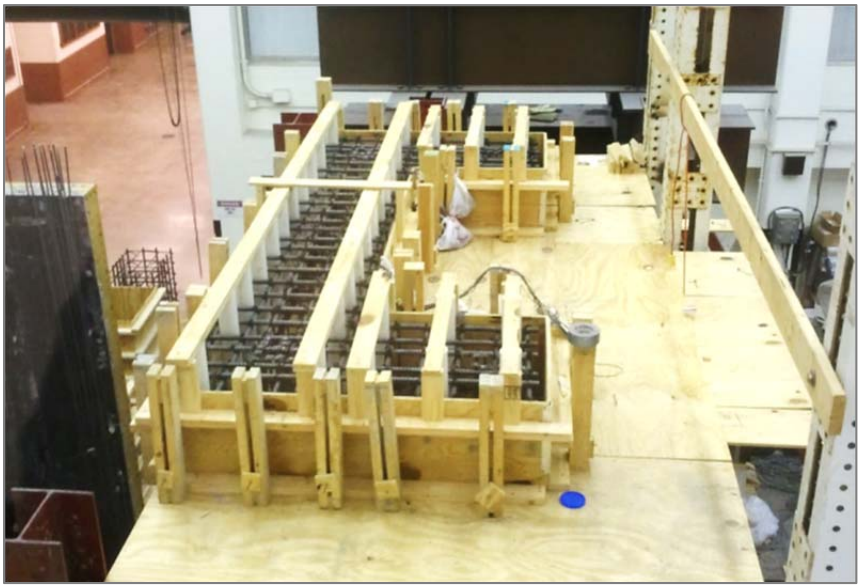

Figure 2.8: Rebar mats and completed formwork for Wall 7 cap

2.3. Wall Specimen Conditions

2.3.1. *Wall 6 Condition*

During the casting of Wall 6, a brace for the formwork split after approximately 11 feet of the wall specimen had been poured. Consequently, the casting was completed in two separate pours with a two hour time gap. There was no indication of a cold joint forming, but a line was visible after removing the formwork as shown in Figure 2.9. The wall exhibited a modest amount of segregation but no significant honeycombing. No patchwork was needed.

Figure 2.9: Wall 6 after formwork removal

2.3.2. ***Wall 7 Condition***

A significant amount of segregation and honeycombing was present after removing the forms of Wall 7. Patchwork was completed in a few areas around the mid-height of the web as shown in Figure 2.10. Additional patching was needed along one flange near the top of the specimen.

Figure 2.10: Wall 7 after patchwork near mid-height of web

2.3.3. ***Wall 8 Condition***

A significant amount of segregation and honeycombing was present on Wall 8 as well as some voids at the bottom of the wall in the corner boundary elements as shown in Figure 2.11. The voids were limited to the cover and did not extend into the confined core of the boundary element. Patchwork was completed using a high-strength grout.

Figure 2.11: Voids in Wall 8 boundary element corner before patchwork

3. Material properties

3.1. Concrete Properties

The concrete mix design used to cast all the C-shaped wall specimens, inclusive of the foundation and cap, was a highly fluid self-consolidating concrete (SCC) that could be poured around a tight rebar cage. In an effort to reflect construction practice the target design strength was 5000 psi with maximum aggregate size limited to 3/8 inch due to space limitations for clear cover and distance between rebar. Since more cement, flyash, and fines were substituted for typical coarse aggregate, reaching the low compressive strength was difficult and as a result a water-to-cement ratio (w/c) of 0.50 was employed in the mix. The batch weights for the concrete mix design are shown in Table 3-1.

Table 3-1: SCC Mix Design (1 cubic yard)

Sand (FA-01)	1383	lb
Coarse (Chips CM-16)	1340	lb
Cement	450	lb
Water	36.7	gal
Flyash	150	lb
Admixtures		
Air	15	oz
WRDA 82	4-6oz/100 cwt	
Properties		
w/c	0.50	

Both 4 inch by 8 inch (4x8) and modulus of rupture (MOR) beams were cast with every wall pour. All compressive cylinder tests were conducted in a Forney testing machine according to ASTM specification C39. The compressive strengths for the concrete used in the walls are shown in Table 3-2; each value represents the average of multiple cylinder breaks. These material tests were performed following testing of the walls; the duration of time between the both the casting of each wall and first day of wall testing to the date of compressive cylinder test are noted.

Table 3-2: Summary of Concrete Compressive Strength

Wall ID	Avg Compressive Strength, f_c' (psi)	Casting to Cylinder Test (days)	Initial Loading to Cylinder Test (days)
Wall 6	4937	513	423
Wall 7	5254	471	175
Wall 8	5119	129	28

3.2. Steel Properties

The primary longitudinal reinforcement used to construct the three C-shaped walls was standard #4 grade 60 (ASTM A706) deformed bars. This type of steel is frequently used in seismic regions on the West Coast and must meet both minimum and maximum yield stress as well as ultimate stress criteria. To maintain similitude in the construction of a one-third scale specimen, it was necessary to use 0.25

inch diameter bars or "#2 bar", rather than a larger #3 bar as it would not meet the geometry, spacing and bending constraints of the design.

Deformed #2bar is not a commonly fabricated construction material, and while researchers tend to use smooth bar stock for small-scale specimens they are not ribbed like typical reinforcing bars nor do they usually exhibit the same steel properties. As round bar stock tends to have a cold rolled response, without a defined yield plateau and having relatively low ductility compared to what is common in hot-rolled reinforcing steel, the research team decided to use a deformed #2 bar with heat treatment to obtain a hot-rolled response. The #2 deformed bar was stamped with external deformation in a helical pattern to have a relative rib area comparable to conventional reinforcing steel; these bars were then treated at a temperature of 1024 degrees for one hour to achieve the desired stress-strain response.

Standard tension tests were carried out for the steel used in the C-shaped walls to determine the as-built properties of the reinforcement. These were performed using a MTS uniaxial testing frame with hydraulic grips. A calibrated extensometer with 4 or 8-inch gauge length was attached to each side of the specimen to measure strain in the bars; only if the specimen ruptured within the gauge length was the measurement considered valid. The measured stress-strain response of the reinforcement used in the construction of the walls can be seen in Figure 3.1.

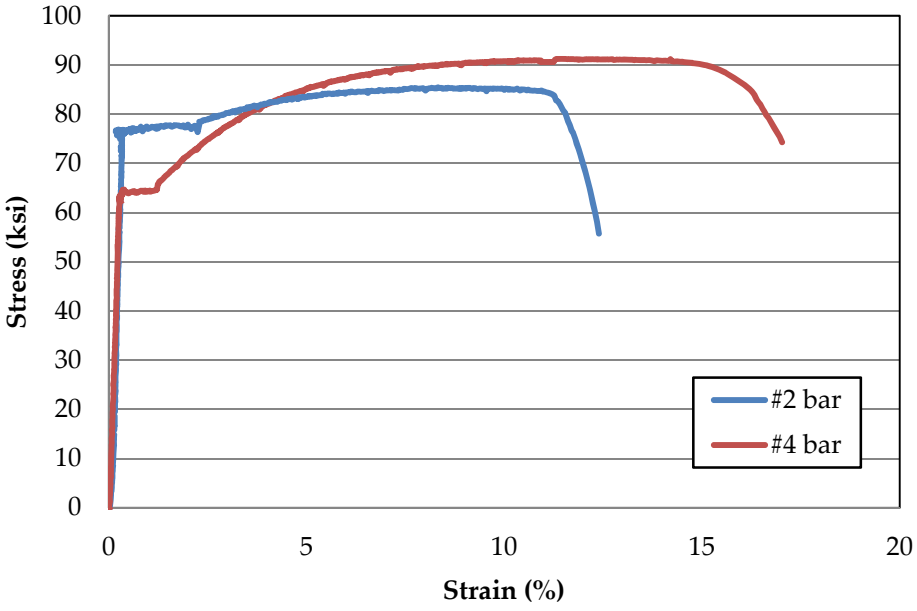

Figure 3.1: Stress-strain plot of rebar for C-shaped Walls

The measured parameters that correspond to the plots in the preceding figure are summarized in Table 3-3, where F_y is the yield stress, ε_y is the yield strain, ε_h is the strain at the onset of strain hardening, F_u is the ultimate stress, and ε_u is the strain at ultimate stress.

Table 3-3: Summary of Steel Properties

Wall ID	Bar Size	F_y ksi	ε_y %	ε_h %	F_u ksi	ε_u %
Wall 6 Wall 7 Wall 8	#2	77.0	0.27	2.3	85.9	11.6
Wall 6 Wall 7 Wall 8	#4	64.0	0.22	1.17	91.3	17.2

4. Test setup & loading protocol

4.1. Introduction

The experimental testing was carried out in the NEES MUST-SIM facility at UIUC. The strong floor consists of a 17 foot (5.2m) deep reinforced concrete box girder that provides approximately 100 kips of anchorage capacity every three feet on center. The L-shaped strong wall dimensions are 50 ft (15.2m) long x 30 ft (9.1m) wide x 28 ft (8.5m) high x 5 ft (1.5m) deep. The strong wall has anchorage points at every two feet on center. The C-wall testing was conducted at the Northwest end of the strong wall along the long portion of the L. To apply the six degree-of-freedom loading, two "Load and Boundary Condition Boxes" (LBCB) were post-tensioned to the strong wall 22 feet above the floor. The LBCBs are spaced approximately 36 inches apart. The test specimen was placed beneath the LBCBs and a series of steel connection plates and beams were utilized to attach the LBCB and wall specimen together. The following section details the test setup connection and the method of loading each wall test.

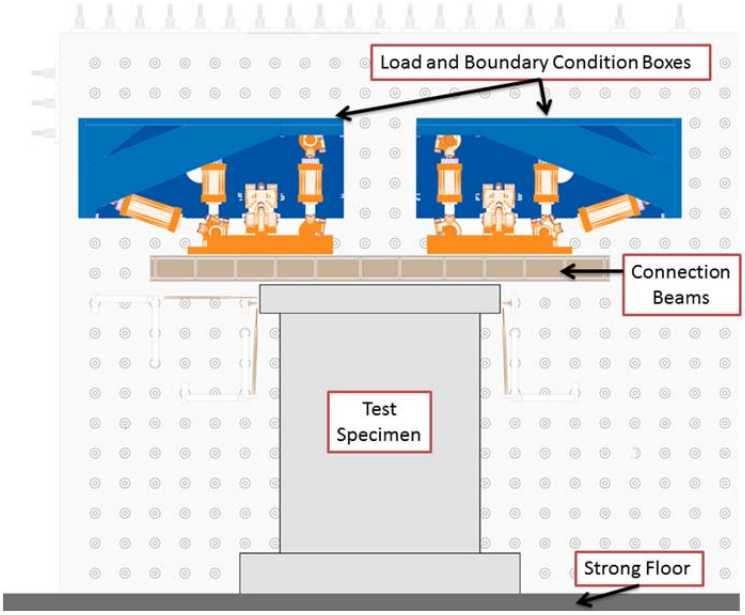

Figure 4.1: LBCB and specimen location on strong wall

4.2. Connection beams description

The footing of the wall specimen is post-tensioned to the strong floor using (12) 2" diameter rods with approximately 100 kips of clamping force in each rod. An assembly of steel beams and plates are used to

mate the wall specimen cap to the LBCB platens. Three wide flange beams (W14x211) are connected to the LBCB platens using (84) 1” diameter high-strength bolts, each with a clamping force of approximately 40 kips. The beams are connected to 2” thick steel plates using (60) 1” diameter high-strength bolts, each with a clamping force of approximately 40 kips. The plates were countersunk to allow the bolt heads to lay flush with the face of the plate. To complete the connection, the plates are connected to the specimen wall cap using (34) 1.5” diameter steel rods, each with a clamping force of approximately 45 kips. Figure 4.2 diagrammatically depicts the connection beam assembly.

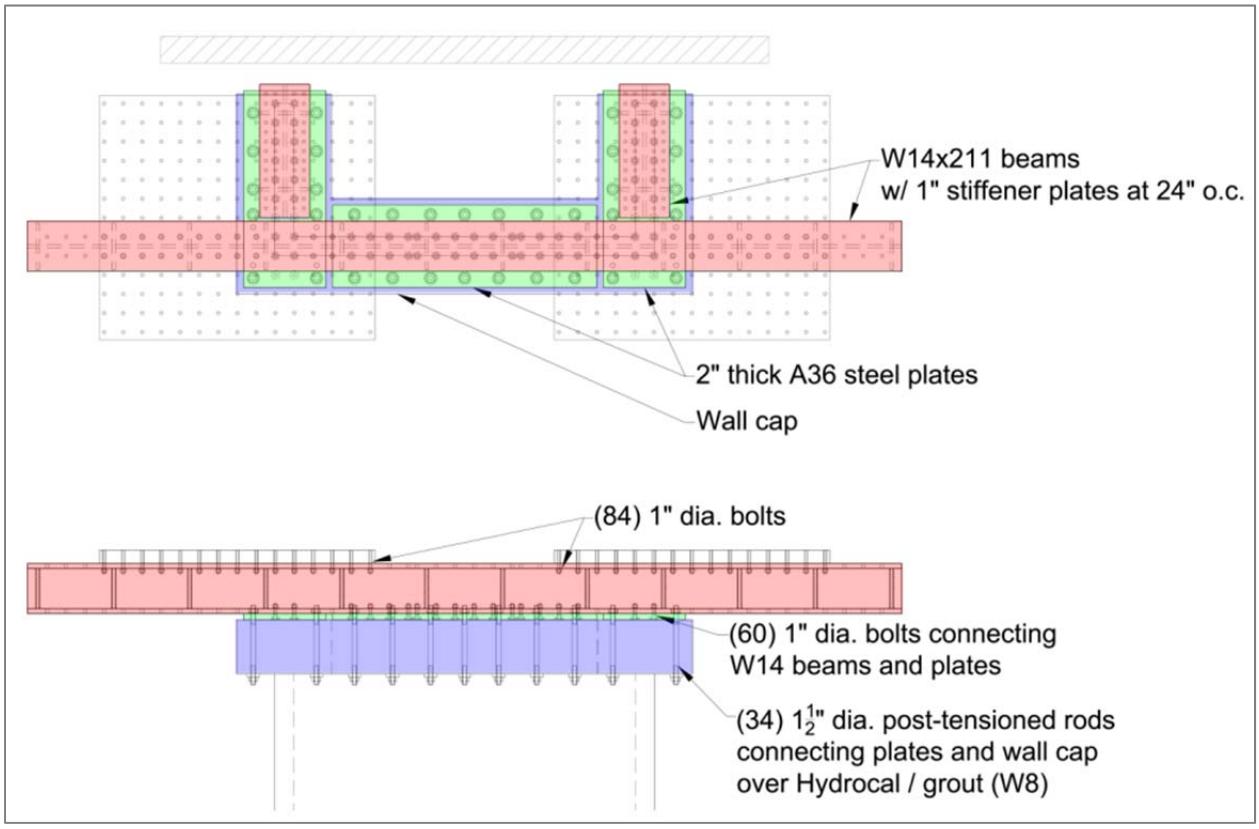

Figure 4.2: Connection beam diagram

The connection assembly is attached to the LBCB platens and then lowered down onto a mixture of Hydrocal/grout on specimen wall cap as shown in Figure 4.3. The Hydrocal/grout creates a flat and even surface for uniform transfer of load between the steel plates and wall cap. Hydrocal is a gypsum cement and was used for connection of Wall 6 and Wall 7. A high-strength grout was used in Wall 8. Grout was used on Wall 8 to allow more working time in making the connection. The mix was allowed to cure prior to connecting and post-tensioning the 1.5” diameter steel rods as shown in Figure 4.4. The completed connection is pictured in Figure 4.5.

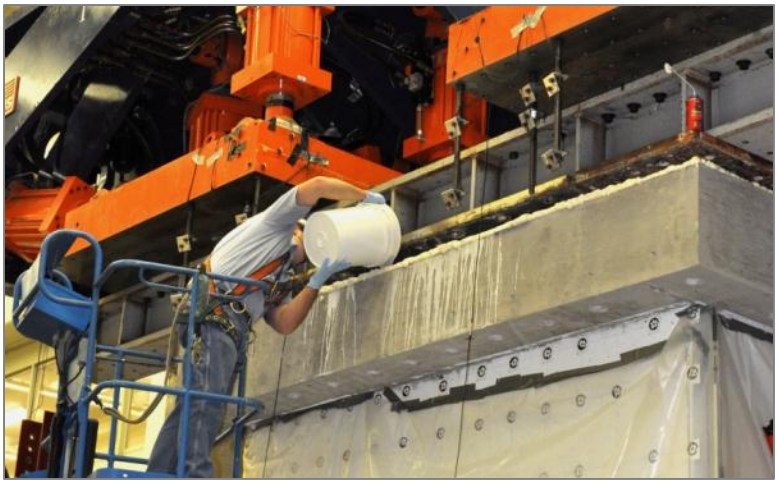

Figure 4.3: Pouring Hydrocal for connection of Wall 7

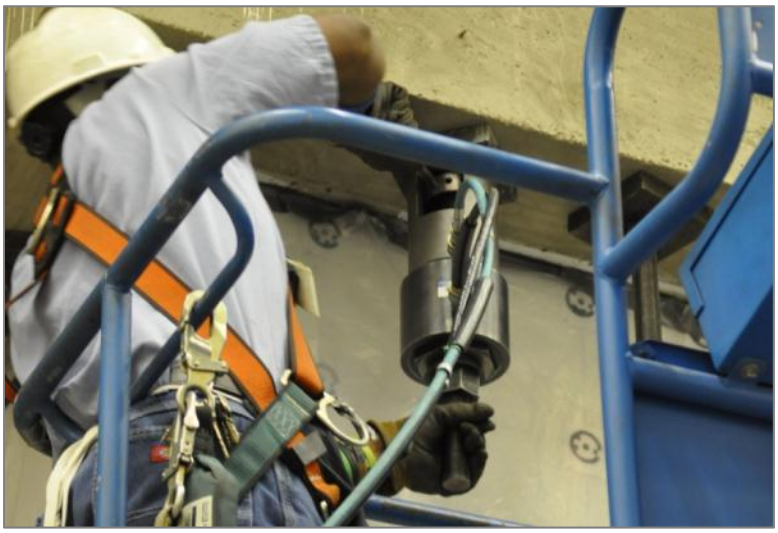

Figure 4.4: Hydraulic tensioning of Wall 8 cap rods

Figure 4.5: Completed connection of Wall 7

4.3. Application of loading

The LBCB described introduced in Section 4.1 is a six DOF loading device that imposes the displacements and forces on the test specimen. The LBCB consists of six 330 kip actuators attached to a steel reaction frame (blue) and steel platen (orange) shown in Figure 4.6. Each actuator has a linear displacement transducer and load cell that provides that position and force carried in each of the six actuators. Mathematical transformation allows the six DOF position of the platen to be determined in Cartesian coordinates from the displacement transducer readings. Similarly, the forces and moments being imposed by the platen can also be determined in the six DOF Cartesian coordinates from the load cell readings. The Cartesian force and moment readings are the sole means of determining the loads imposed on the test specimen. Figure 4.6 shows the LBCB platen and each of the six actuators identified as "X1" and "X2" for the X-direction, "Y1" for the Y-direction, and "Z1","Z2", and "Z3" for the Z-direction.

The LBCB "Mixed-mode" control software allows the LBCBs to be controlled in both displacement and force simultaneously. This enables the control a selection of the six DOFs to be in displacement control and other DOFs in force control.

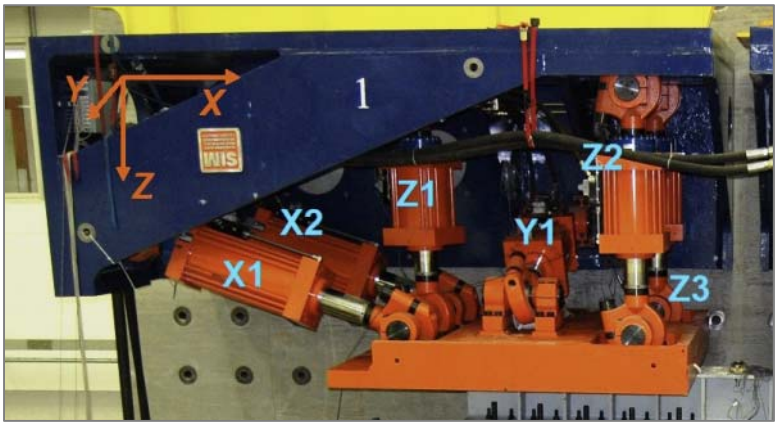

Figure 4.6: LBCB actuator nomenclature

4.4. Loading protocol

The primary study variable for the test program was displacement history, as illustrated in Table 4-1. Wall 6 was tested under unidirectional lateral loading and subjected to a constant axial load of $0.05f'_cA_g$. Wall 7 was subjected to bidirectional lateral loading and a constant axial load of $0.05f'_cA_g$. Wall 8 was tested using a loading protocol that simulated a C-shaped wall constructed as part of a coupled wall system. Like Wall 7, the Wall 8 was subjected to a bidirectional lateral load history. For Wall 8, the axial load was determined from a computational model of a fully coupled core wall system. The axial load place on the system depended on the level of drift and direction of movement, as the C-shaped wall itself simulated one pier of the core wall system.

Table 4-1: Test Matrix and Loading Protocol for Walls 6,7 and 8

Wall ID	X-direction Lateral Loading	Y-direction Lateral Loading	Axial Load
Wall 6	Cyclic, Symmetric	None	Constant
Wall 7	Cyclic, Symmetric	Cyclic, Asymmetric	Constant
Wall 8	Cyclic, Symmetric	Cyclic, Asymmetric	Varies

The loading protocol for all three C-shaped wall specimens was based on the prototype ten-story core-wall system subjected to the ASCE 7-07 equivalent lateral force (ELF) distribution for design for earthquake loading and gravity load. The test specimens represent the bottom three stories of this ten-story prototype structure at one-third scale. The performance of the upper stories of the wall was assumed to be non-critical to the global system performance, and thus the upper stories were not tested in the laboratory. The effects of the gravity and lateral loads acting on the upper seven stories of the wall were simulated in the laboratory through application of an overturning moment, shear force, and axial force on the top of the test specimen.

Each specimen was subjected to a quasi-static cyclic displacement history along one or both horizontal principal axes of the test specimen. Each step of the displacement history represented application of a lateral translation as well as an axial force and overturning moment. The target axial force and overturning moment were a function of the measured lateral shear from the applied displacement, thus requiring an incremental-iterative approach for determining the converged state of the wall at the end of each step. The displacement history was discretized into thousands of displacement steps to facilitate convergence at each step. The displacement step size varied from approximately five thousands of an inch (0.005 in.) in the elastic range to four hundredths of an inch (0.04 in.) in the post-yielding regime. The loading rate also varied but did not exceed one hundredth of an inch per second (0.01 in/sec).

The coordinate system for controlling the test about the two principal axes of the test specimen is given in Figure 4.7. The control point corresponds to the geometric centroid of un-cracked wall specimen at the top of the third story. Using the LBCB control all translations and rotations are commanded about this point and the resulting forces and moments are measured about this point. The command DOFs for the three separate wall tests are given in Table 4.2 The following sections provide a detailed description of each test's loading protocol.

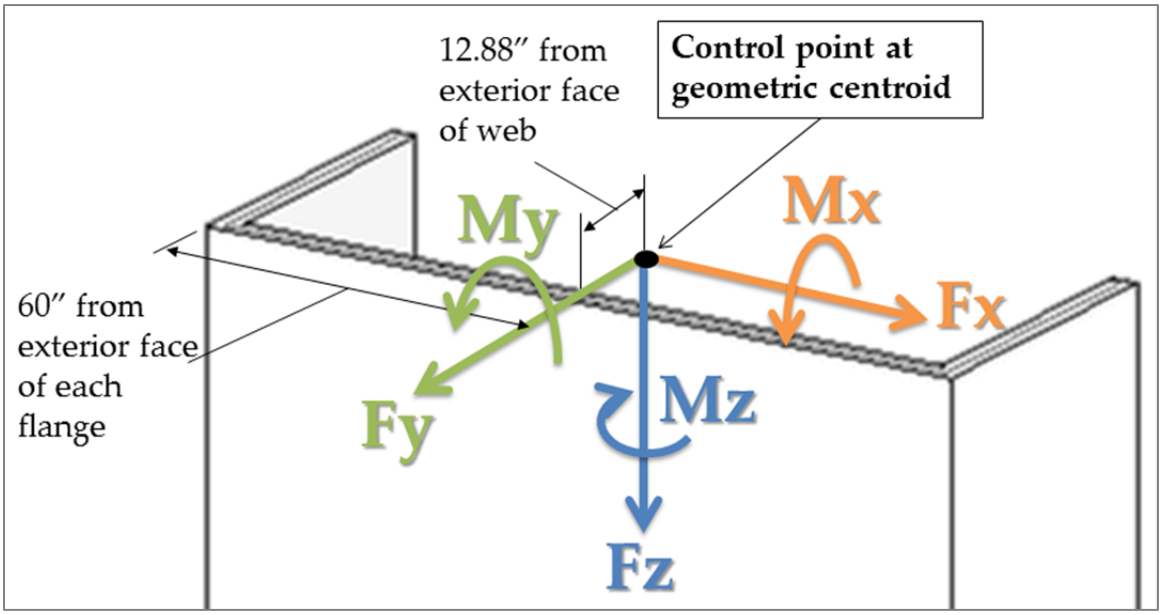

Figure 4.7: C-shaped wall coordinate system

Table 4-2: Loading control DOFs

	Dx / Fx	Dy / Fy	Dz / Fz	Rx / Mx	Ry / My	Rz / Mz
C-Wall 6	Displacement Control	Zero Displacement	Force Control	Zero Displacement	Force Control	Zero Displacement
C-Wall 7	Displacement Control	Displacement Control	Force Control	Force Control	Force Control	Zero Displacement
C-Wall 8	Displacement Control	Displacement Control	Force Control	Force Control	Force Control	Zero Displacement

4.4.1. *Wall 6 Loading Protocol*

The first C-shaped wall test investigated performance of the test specimen under strong-axis bending. A cyclic unidirectional displacement history was executed with an associated constant axial load and moment representative of the prototype structure shown in Figure 4.8. The axial load was held constant at value of 5% of the gross axial capacity of the wall ($0.05f_cA_g$), which is equal to 306 kips. The overturning moment to shear ratio was held constant at 196.8 in; this follows from the ASCE 7-07 ELF distribution. Two cycles of displacement were completed at each drift level in the X-direction, which corresponded to strong axis bending as shown in Figure 4.9. Maximum displacement demands for displacement cycles were intended to target limit states of concrete cracking, yielding of longitudinal reinforcement, nominal flexural strength, concrete spalling and subsequent damage states. The displacement history is shown in Table 4-3 and Figure 4.10.

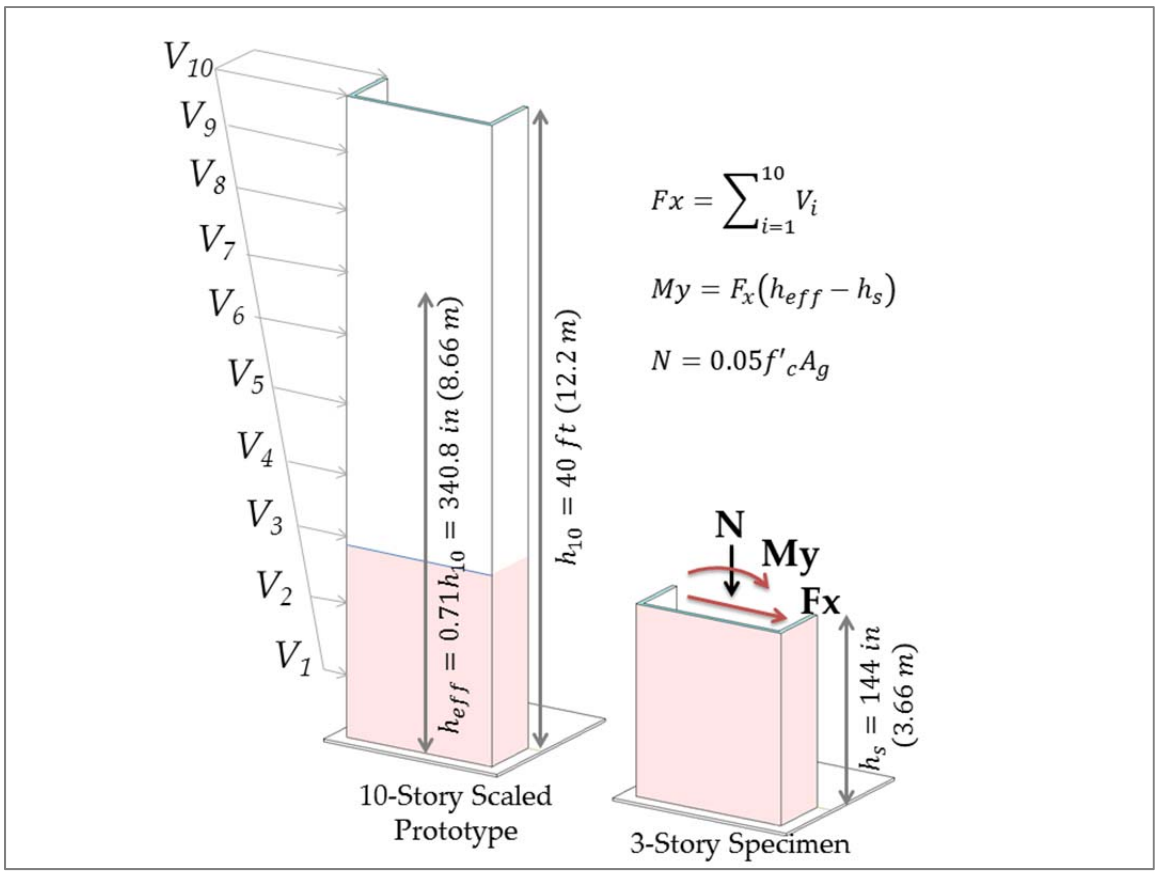

Figure 4.8: Wall 6 loading protocol

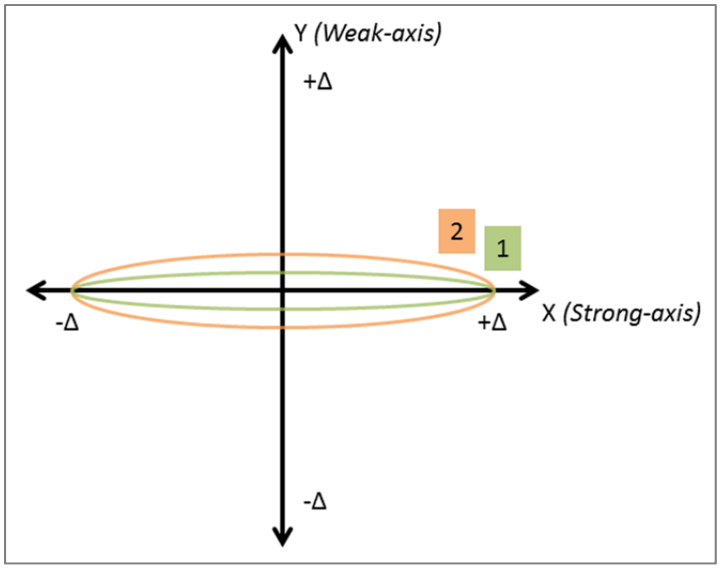

Figure 4.9: Loading pattern 1 - strong axis unidirectional

Table 4-3: Wall 6 Displacement History

Target Limit State	Disp(in)	Disp (% Drift)	# of Cycles
Elastic	0.02	0.014%	1
Cracking	0.04	0.028%	1
25% Yield	0.1	0.069%	2
50% Yield	0.2	0.139%	2
75% Yield	0.3	0.208%	2
100% Yield	0.5	0.347%	2
150% Yield	0.72	0.5%	2
Nominal	1.08	0.75%	2
Damage	1.44	1%	2
Damage	2.16	1.5%	2
Damage	3.24	2.25%	2
Pushover	5.057	3.512%	+X only

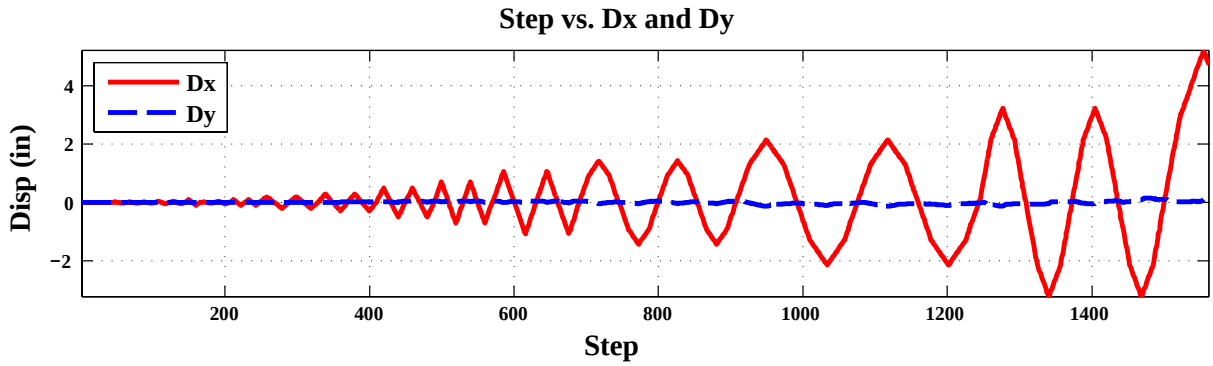

Figure 4.10: Wall 6 plot of displacement history in x- and Y-directions

4.4.2. *Wall 7 Loading Protocol*

The second C-shaped wall test investigated the bidirectional performance of the test specimen. A cyclic cruciform displacement history was executed with an associated constant axial load and constant moment-to-shear ratio as shown in Figure 4.11. The axial load was held constant at 5% of the gross axial capacity ($0.05f_cA_g$), equal to 306 kips . The overturning moment to shear ratio was held constant at 196.8 in., which follows from the ASCE 7-07 ELF distribution, in both principal directions.

For the majority of the test, two displacement cycles were completed in each direction at each drift level following the cruciform history shown in Figure 4.12. Following this cruciform history, cycles 1 and 3 displace the wall in the direction of the web of the wall, which is the X-direction and activates strong-axis bending of the wall; cycles 2 and 4 displace the wall in the directions of the flanges, which is the Y-direction and activates weak-axis bending of the wall. Towards the end of the test, the displacement capacity of the loading apparatus was reached in the positive and negative Y-directions. To enable application of increasing demand on the boundary elements of the wall, which are severely loaded under weak-axis / Y-direction loading, the cruciform displacement history was replaced with the bidirectional displacement history shown in Figure 4.13. This displacement pattern consisted of a full displacement cycle in X-direction while maintaining a constant Y-direction displacement. Maximum displacement demands for displacement cycles in both the x- and Y-directions were intended to target limit states of concrete cracking, yielding of longitudinal reinforcement, nominal flexural strength, concrete spalling and subsequent damage states. The displacement history is shown in Table 4-4 and Figure 4.14.

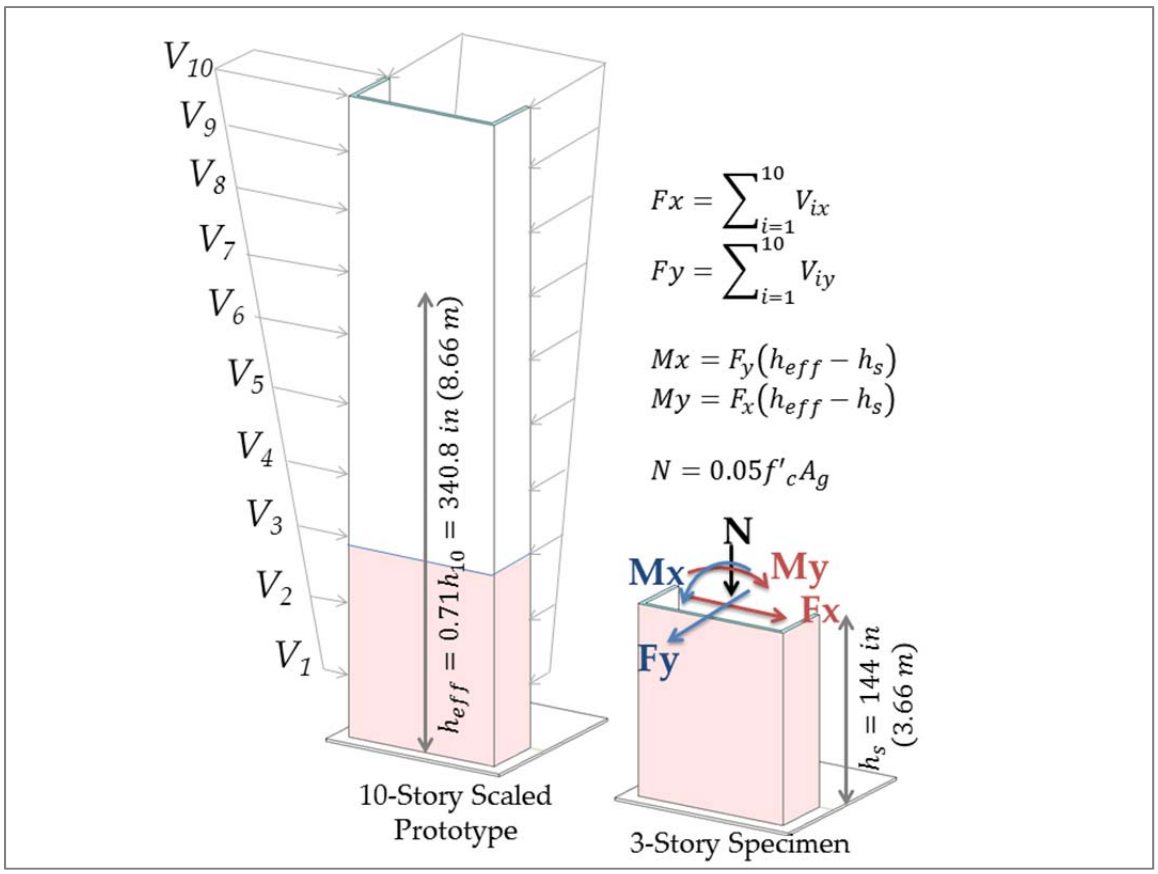

Figure 4.11: Wall 7 loading protocol

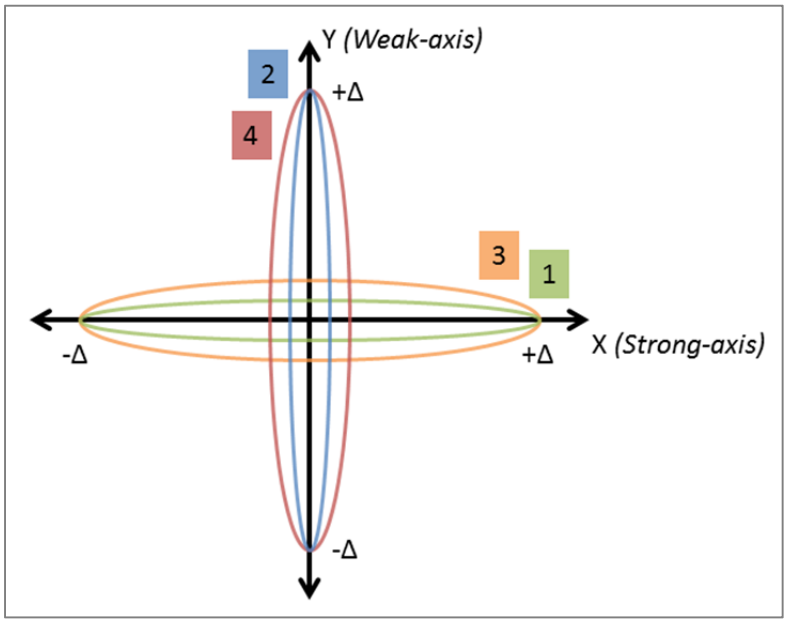

Figure 4.12: Loading pattern 2 - cruciform bidirectional

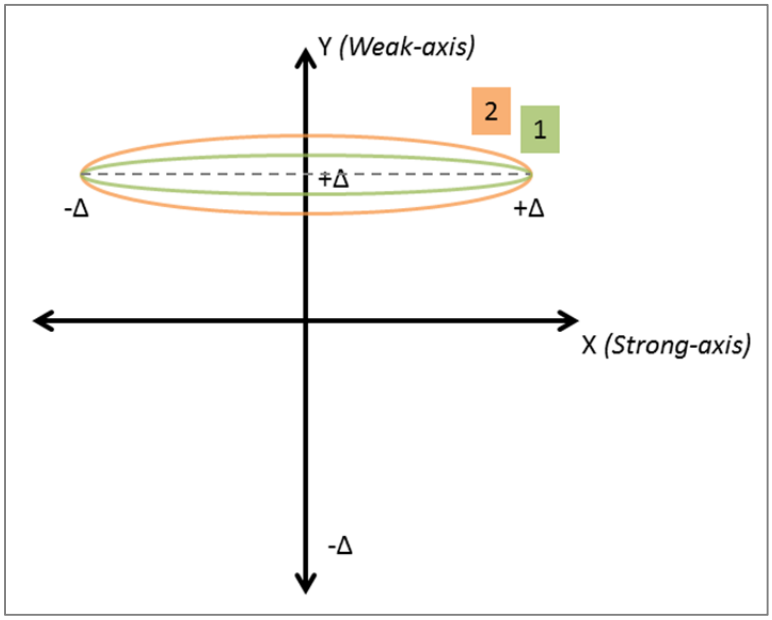

Figure 4.13: Strong axis disp. at given weak axis disp.

Table 4-4: Wall 7 Displacement History

Target Limit State	Loading Pattern	Dx (in)	+Dy (in)	-Dy (in)	Dx (% drift)	+Dy (% drift)	-Dy (% drift)	# of Cycles
Elastic	Cruciform	±0.02	0.02	-0.02	0.014%	0.014%	-0.014%	1
Cracking	Cruciform	±0.04	0.08	-0.12	0.028%	0.056%	-0.083%	2
	Cruciform	±0.1	0.2	-0.3	0.069%	0.14%	-0.21%	2
50% Yield	Cruciform	±0.2	0.4	-0.6	0.14%	0.28%	-0.42%	2
75% Yield	Strong Axis	±0.3	---	---	0.21%	---	---	1
100% Yield	Cruciform	±0.5	0.6	-0.9	0.35%	0.42%	-0.63%	2
1/2 Nominal	Cruciform	±0.72	1.8	-1.05	0.50%	1.25%	-0.73%	2
Nominal	Cruciform	±1.08	3.24	-1.22	0.75%	2.25%	-0.85%	1
	Cruciform	±1.08	3.24	-2.14	0.75%	2.25%	-1.49%	1
Damage 1	Cruciform	±1.44	3.24	-2.14	1%	2.25%	-1.49%	1
	Strong Axis	±1.44	---	---	1%	---	---	1
Damage 2	Constant Dy	±1.44	2.88	---	1%	2%	---	1
	Constant Dy	±1.44	---	-1.584	1%	---	-1.1%	1
Damage 3	Strong Axis	±2.16	---	---	1.5%	---	---	1
Damage 4	Constant Dy	±2.16	2.88	---	1.5%	2%	---	1
Pushover +X	Constant Dy	2.81	2.88	---	1.95%	2%	---	1

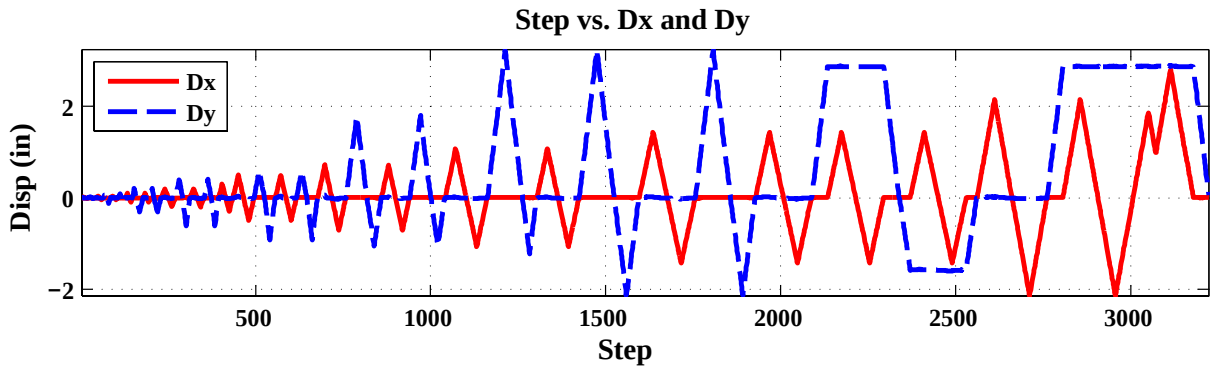

Figure 4.14: Wall 7 plot of displacement history in x- and Y-directions

4.4.3. *Wall 8 Loading Protocol*

The third C-shaped wall test investigated the bidirectional performance of the test specimen when considered as part of a coupled core wall system. A cyclic cruciform displacement history was executed with axial load and moment applied at the top of the specimen determined from the ASCE 7-07 ELF and gravity loads applied to the complete coupled core-wall system as shown in Figure 4.15. For displacement cycles in the X-direction, parallel to the webs of the C-shaped walls, coupling beams are not activated and the response of the C-shaped walls is essentially identical to the response of an isolated C-shaped wall. Thus, for displacement cycles in the X-direction, a constant axial load equal to 5% of the gross axial capacity (0.5fcAg), equal to 306 kips, was applied and a constant moment-to-shear ratio of 196.8 in., which follows from the ASCE 7-07 ELF distribution was used.

Lateral loading of the core wall system in the Y-direction, parallel to the flanges of the C-shaped walls, activates coupling beams resulting in "coupling" of the C-shaped walls. Flexural response of the coupling beams results in tensile loads being applied to one of the C-shaped walls, identified as the tension pier, and compression loads being applied to the other C-shaped wall, identified as the compression pier. These tension/compression loads affect the flexural stiffness and strength of the C-shaped walls and results in the individual wall piers developing very different internal moments and shears at each story. To simulate this in the laboratory test, for displacement cycles in the Y-direction, axial load and moment applied to the top of the specimen were varied. Following is a detailed discussion of the process employed to determine an appropriate protocol for Y-direction loading of the test specimen.

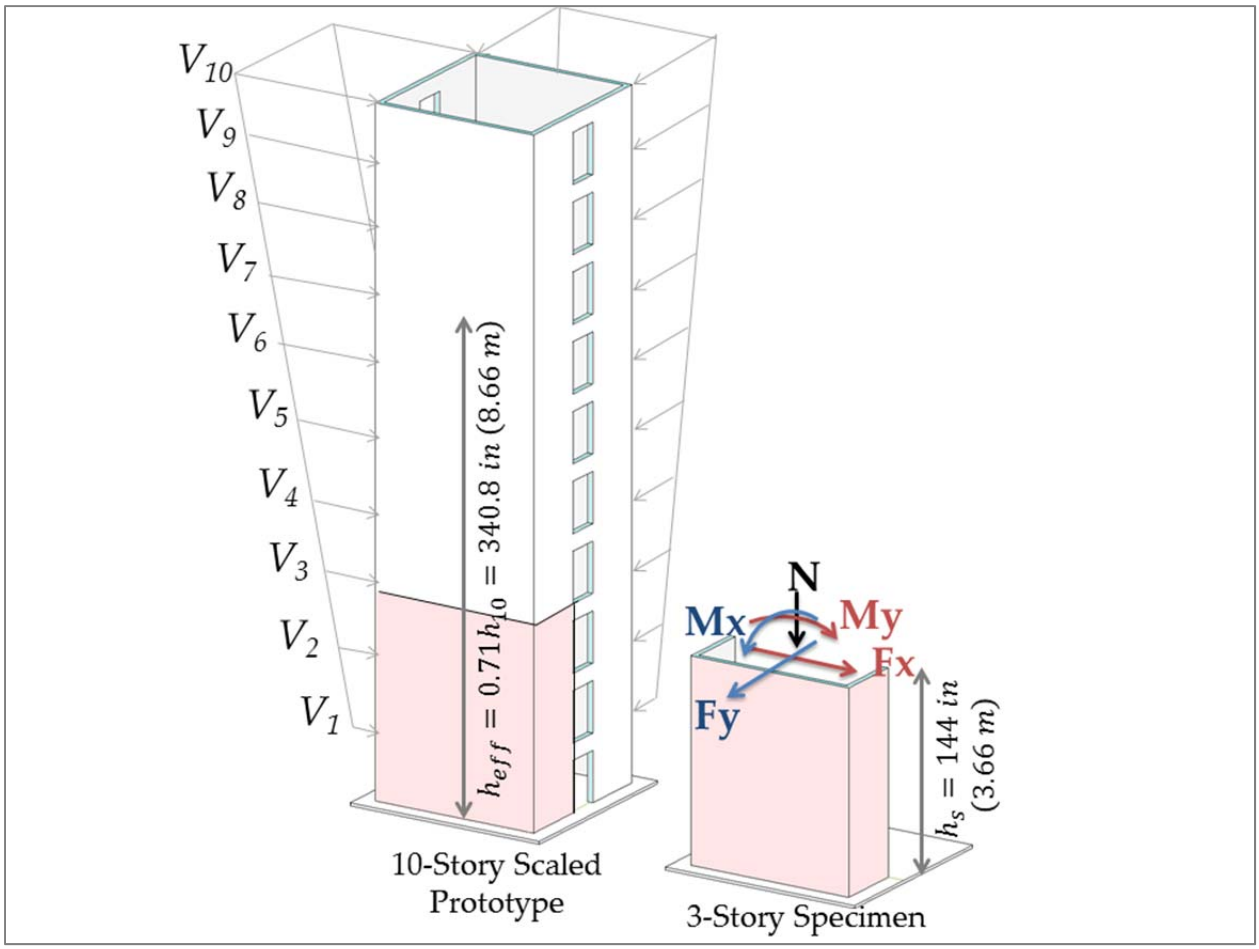

Figure 4.15: Wall 8 loading protocol

Details of Y-direction loading and simulation of demands resulting from coupling

Specification of the Y-direction loading protocol comprised specification of (1) the ratio of shear, axial and moment demand to be applied to the specimen for loading in the positive and negative Y-directions and (2) the maximum displacement demands in the positive and negative Y-directions for each cycle. The following paragraphs explain the process employed to develop these specifications as well as the control logic employed to implement these specifications in the laboratory.

Y-direction loading, which activates coupling between the wall piers, results in the individual wall piers carrying significantly different shear, axial load and moments at each story. The distribution of total

story shear, axial load and moment between the individual wall piers, and thus the ratio of shear, axial and moment demand for an individual wall pier, varies as a function of wall stiffness. To establish appropriate demand ratios (i.e. ratio of shear, axial and moment demand) for use in testing, numerical analyses of the ten-story prototype core-wall system subjected to the increasing lateral load and constant gravity load were conducted. The demand ratio versus roof drift histories developed from these analyses were simplified for use in testing; ultimately seven different ratios were used at different stages of the test. Demand ratios were varied during the test on the basis of measured response quantities and observed damage.

It should be noted that the laboratory test specimen represents the bottom three stories of one C-shaped wall pier *without coupling beams*. Without coupling beams, the demands that develop in a C-shaped wall in the coupled core-wall system cannot be simulated in the laboratory specimen over the entire three-story height of the laboratory specimen. Consequently, demands were applied at the top of the laboratory specimen to achieve representative demands in the critical first story of the specimen. This is illustrated in a free-body-diagram of the coupled walls individual and system demands in Figure 4.16.

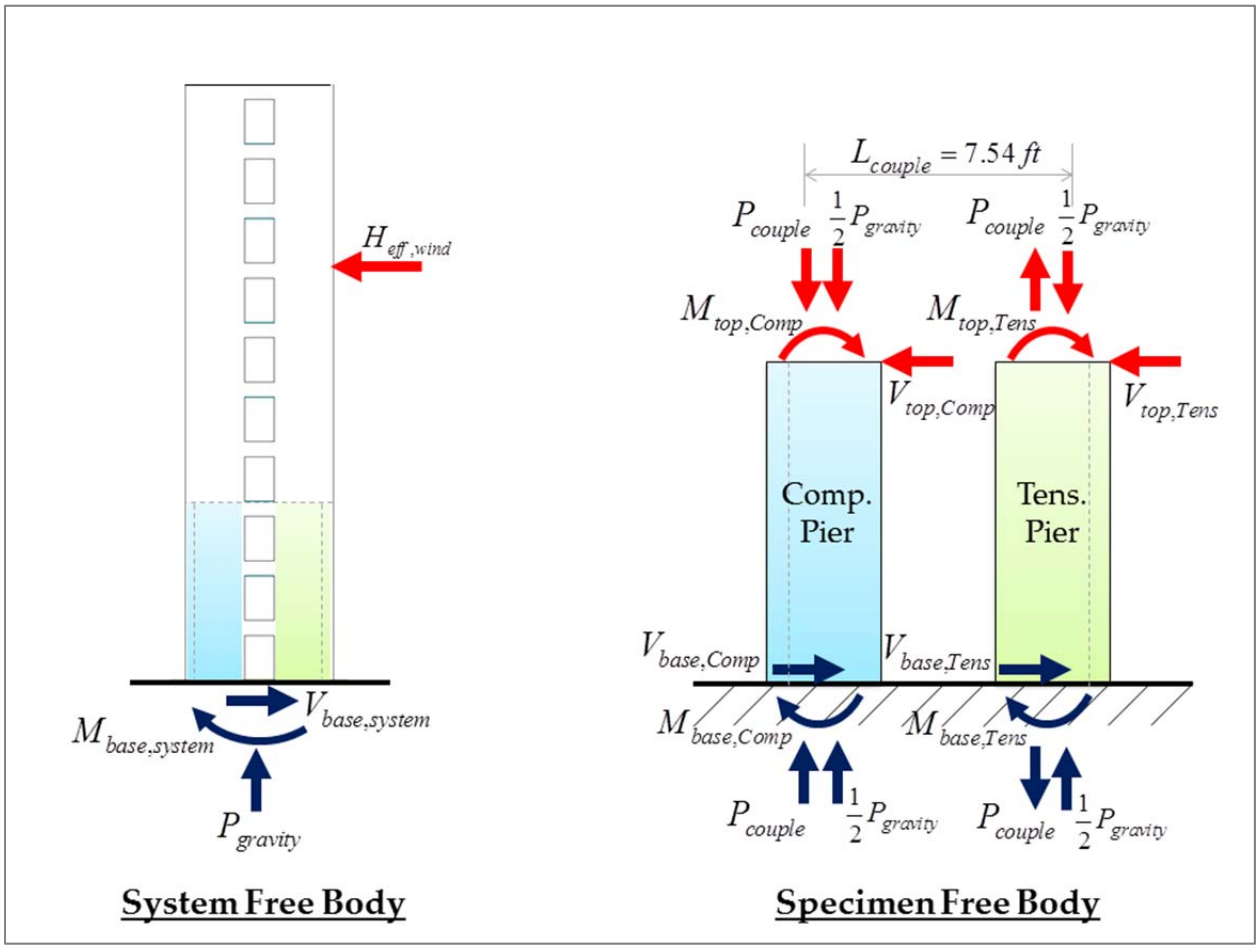

Figure 4.16: Coupled core wall free body diagram

Analysis results indicated that under lateral loading of the core-wall system, lateral displacements for the individual wall piers differed due to axial elongation of coupling beams. Initially, it was assumed that

this difference in wall displacements could be ignored and displacement demands in the positive and negative Y-directions could be of equal magnitude. However, as testing progressed and the stiffness of the specimen under positive Y-direction loading began to differ substantially from the stiffness of the specimen under negative Y-direction loading (this would be analogous to the stiffness of the compression wall pier in the coupled wall system differing substantially from the stiffness of the tension wall pier), it was observed that the loads applied at the maximum and minimum Y-direction displacement demands did not, when combined, represent an equilibrium state for the core-wall system. In the core-wall system, loads applied to the specimen under positive and negative Y-direction loading would be applied simultaneously to the individual wall piers; thus, applied loads, when combined, should approximately represent an equilibrium state for the core-wall system. Thus, for subsequent displacement cycles, a force-based approach was used to determine maximum displacements in the positive and negative Y-directions.

Numerical analyses indicated that for moderate to large displacement demands, the compression pier determines core-wall strength. This is because at these displacement demands the tension pier has minimal stiffness relative to the compression pier and carries relatively little shear and moment relative to the compression pier. Given this, a force-based approach to determining displacement demands was developed in which (1) the test specimen was first loaded to a target drift demand in the positive Y-direction, such that it became the compression pier, (2) the axial force and moment demands at the target drift demand were recorded, and (3) the specimen was loaded in the negative Y-direction until the axial force and moments required for equilibrium of the core-wall system were achieved. No consideration was given to the magnitude of the shear force applied at the peak displacement in the negative Y-direction; thus, this loading protocol did not maintain the moment-to-shear ratio associated with the ASCE 7-07 ELF distribution for the core-wall system.

The displacement history for Wall 8 is given in Table 4-5 and Figure 4.17; Table 4-5 lists also the moment, shear, and axial load ratios for the pier walls, where

$V_{base,CompRatio}$ = Portion of system base shear to the compression pier

$V_{base,TensRatio}$ = Portion of system base shear to the tension pier

$M_{base,CompRatio}$ = Portion of system moment to the compression pier

$M_{base,TensRatio}$ = Portion of system moment to the tension pier

$M_{base,CoupleRatio}$ = Portion of system moment to coupling

Table 4-5: Wall 8 Displacement History

Target Limit State	Loading Pattern	Dx (in)	Dy (in)	Dx (% drift)	Dy (% drift)	# of Cycles	Mbase Couple Ratio	MbaseC Ratio	MbaseT Ratio	VbaseT Ratio	VbaseC Ratio
Elastic	Cruciform	±0.02	±0.02	0.027%	0.027%	1	0.65	0.25	0.1	0.35	0.65
Cracking	Cruciform	±0.04	±0.04	0.027%	0.027%	2	""	""	""	""	""
	Cruciform	±0.1	±0.1	0.067%	0.067%	2	0.65	0.25	0.1	0.2	0.8
50% Yield	Cruciform	±0.2	±0.2	0.14%	0.14%	2	""	""	""	""	""
75% Yield	Cruciform	±0.35	±0.35	0.24%	0.24%	1	""	""	""	""	""
	Weak axis	0	±0.44	0%	0.30%	2	""	""	""	""	""
100% Yield	Cruciform	±0.5	±0.65	0.35%	0.35%	2	""	""	""	""	""
	+Y only	0	0.711	0%	0.49%	1	""	""	""	""	""
	Weak axis	0	±0.8	0%	0.55%	1	0.6	0.32	0.08	0.3	0.7
Logic change to force target for tension pier											
1/2 Nominal	Strong Axis	±0.72	0	0.50%	0%	1	0.6	0.33	0.07	0.15	0.65
	Comp. Pier	0	0.8	0%	0.55%	1	""	""	""	""	""
	Tension Pier	0	-0.178	0%	-0.12%	1	""	""	""	""	""
	Strong Axis	±0.72	0	0.50%	0%	1	""	""	""	""	""
	Comp. Pier	0	1.2	0%	0.83%	1	""	""	""	""	""
	Tension Pier	0	-0.14	0%	-0.09%	1	""	""	""	""	""
Nominal	Strong Axis	±1.08	0	0.75%	0%	1	""	""	""	""	""
	Comp. Pier	0	1.2	0%	0.83%	1	""	""	""	""	""
	Comp. Pier	0	1.6	0%	1.11%	1	0.6	0.28	0.12	0.25	0.65
	Tension Pier	0	0.067	0%	0.05%	1	""	""	""	""	""
	Comp. Pier	0	1.6	0%	1.11%	1	""	""	""	""	""
	Tension Pier	0	-0.4	0%	-0.28%	1	""	""	""	""	""
Damage 1	Strong Axis	±1.44	0	1.0%	0%	1	""	""	""	""	""
	Comp. Pier	0	1.6	0%	1.11%	1	""	""	""	""	""
	Tension Pier	0	-0.223	0%	-0.16%	1	""	""	""	""	""
	Comp. Pier	0	2.4	0%	1.67%	1	""	""	""	""	""
	Tension Pier	0	-0.168	0%	-0.11%	1	""	""	""	""	""
Damage 2	Strong Axis	±2.16	0	1.5%	0%	1	""	""	""	""	""
	Comp. Pier	0	2.84	0%	1.94%	1	""	""	""	""	""
	Tension Pier		-2.84	0%	1.94%	1	0.6	0.28	0.26	0.6	0.65
Damage 3	Strong Axis	±2.56	0	1.777%	0%	1	""	""	""	""	""
	Comp. Pier	0	2.84	0%	1.97%	1	""	""	""	""	""
	Tension Pier	0	-3.01	0%	-2.09%	1	0.6	0.28	0.24	0.6	0.65
Damage 4	Comp. Pier	0	2.95	0%	2.05%	1	0.6	0.2	0.24	0.6	0.8
	Tension Pier	0	-3	0%	-2.08%	1	0.6	0.2	0.23	0.6	0.8
Damage 5	Comp. Pier	0	2.95	0%	2.05%	1			Fz = 1,000 kips		
	Tension Pier	0	-2.745	0%	-1.91%	1			Fz = -250 kips		
	Comp. Pier	0	2.33	0%	1.62%	1			Fz = 1,000 kips		

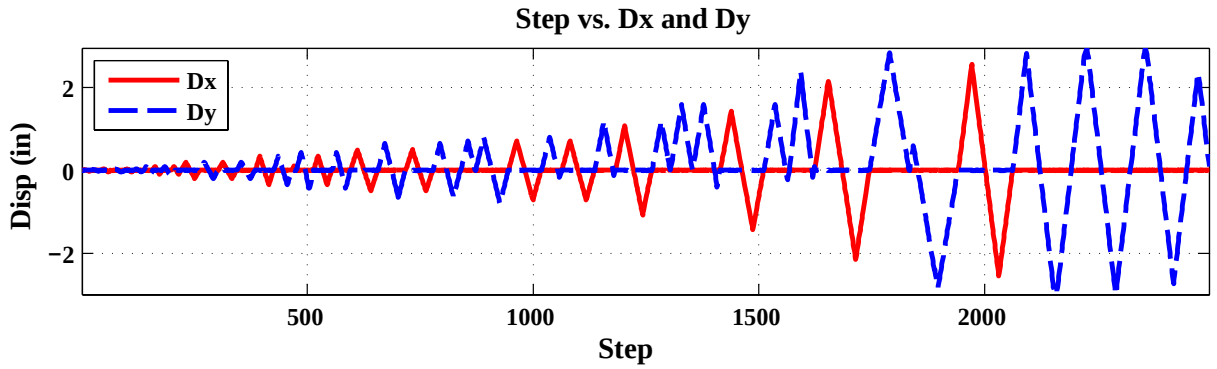

Figure 4.17: Wall 8 plot of displacement history

The Y-direction loading protocol described above was implemented using the following logic. The external control loop performs these steps at each displacement step with iteration as needed to reaching a converged equilibrium state for the specimen:

1. Impose weak axis displacement (*Dy*)

2. Measure base shear of the wall specimen ($V_{base,C}$)

3. Determine if compression pier or tension pier based on measured shear
   If *Fy > 0* then consider as Compression Pier.
   If *Fy < 0* then consider as Tension Pier

4. Calculate equilibrium target
   i. Calculate system base shear from measured shear of the specimen

$$V_{base,system} = \begin{cases} \dfrac{V_{base,C}}{V_{base,CompRatio}} & \text{for compression pier} \\ \dfrac{V_{base,C}}{V_{base,TensRatio}} & \text{for tension pier} \end{cases}$$

   ii. Calculate system base moment from system base shear

$$M_{base,system} = V_{base,system}\left(0.71 h_{eff}\right)$$

   iii. Calculate moment at base of specimen

$$M_{base,C} = \begin{cases} M_{base,system}\left(M_{base,CompRatio}\right) & \text{for compression pier} \\ M_{base,system}\left(M_{base,TensRatio}\right) & \text{for tension pier} \end{cases}$$

   iv. Calculate moment due to coupling

$$M_{base,couple} = M_{base,system}\left(M_{base,CoupleRatio}\right)$$

   v. Calculate axial load from moment due to coupling

$$P_{base,couple} = \frac{M_{base,couple}}{L_{couple}}$$

   vi. Calculate total axial force from gravity and coupling

$$P_{top,C} = P_{base,couple} + P_{gravity}$$

   vii. Calculate total moment to be applied at the third story

$$M_{top,C} = M_{base,C} - V_{base,C}\left(h_{specimen}\right)$$

5. Impose calculated $P_{top,C}$ and $M_{top,C}$ on specimen

5. Section 5 – Instrumentation and Data Collection

5.1. Instrumentation Overview

A unique feature of the C-shaped wall tests is the variety and density of instrumentation used to monitor specimen behavior. The instrumentation consisted of traditional and non-contact systems that capture displacement and strain. The traditional sensors consisted of strain gauges applied externally to the concrete and directly to the steel reinforcement within the specimen as well as displacement transducers such as linear variable displacement transducers (LVDTs) and string potentiometers to measure relative and absolute displacements. To gather full-field deformation data, advanced instrumentation methods were utilized including the Nikon Metrology/Krypton 600 Optical CMM system and photographs from high resolution still cameras to be used with photogrammetric techniques. Throughout the tests, a variety of other documentation equipment was employed to record the progression of damage including the use of a roaming camera as well as video and web cameras.

Figure 5.1 provides a plan view of the laboratory set-up for the C-shaped wall experiment. There are eight reference columns installed around the wall specimen to provide a fixed location to attach absolute displacement transducers as well as a place to mount still cameras used for photogrammetry. The diagram illustrates the location and orientation of the two Nikon Metrology/Krypton cameras, in addition to their field-of-view indicated by a trapezoidal region. Also shown are the positions of the data acquisition (DAQ) hardware cart and the computer stations set up for operating controls and monitoring the various data collection systems.

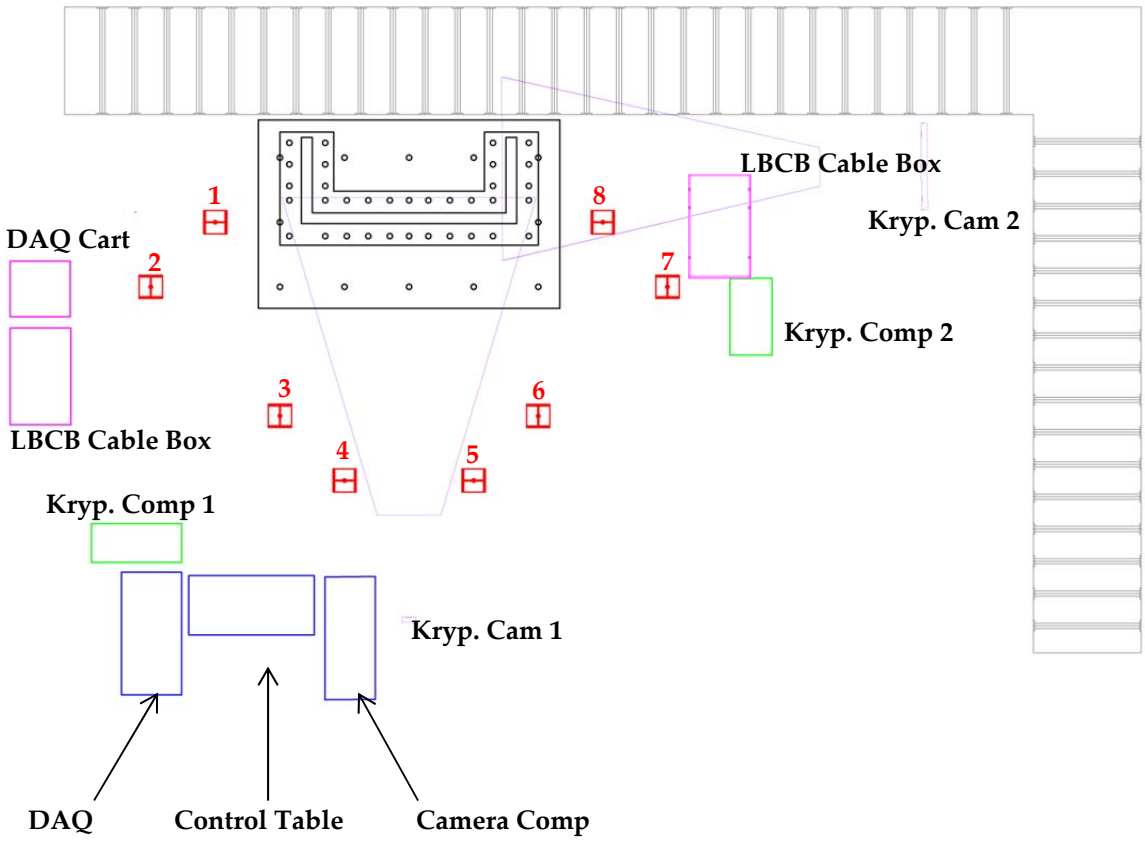

Figure 5.1: Plan View Diagram of Experimental Test Set-up

5.2. Strain Gauges

5.3.1 Introduction

During testing, strain gauge readings can be used as a verification method that the intended loading is being properly applied as the research team intends. Especially during the early elastic region of the testing protocol, examining strain data can indicate that axial load is distributed uniformly across the wall cross-section, that the specimen's response corresponds to the intended direction and magnitude of the top displacement to which it is being subjected.

Beyond this rather basic role as a check for applied loading, strain readings serve as one of the primary indicators that certain limit states have been reached. Observing the increase in strain values can signal when and where cracks are developing in the concrete as forces begin to be carried by reinforcement. In addition, this sensor data provides information about the onset of steel yield and progression of plastic behavior. Much attention is devoted to examining the strain levels across the 120+ gauges at later displacement peaks, especially the differences seen in the more heavily reinforced boundary element regions versus the unconfined areas in the center of the flanges and the web. Particularly in the bidirectional tests (UW 2 & 3), these observed strains played a role in determining any modifications that needed to be made to the displacement level and/or load ratios selected for future test cycles to achieve the desired benchmarks along the path to target limit states (i.e. selected percentage of yield or predicted nominal capacity).

Following testing, the data collected from the wide array of longitudinal, horizontal, and stirrup strain gauges distributed throughout the C-shaped wall specimen provides many analysis opportunities. A few select examples include: researchers will be able to examine the strain distributions that occur along vertical or horizontal cross-sections throughout the entire test history; strain values can be utilized to calculate the variation in curvature over the height of wall; also, the wall can be divided into distinct regions for the flanges and web, using strain to evaluate the moment being carried by each zone. In terms of making comparisons to computational models, many programs allow users to examine the average strain seen in the concrete or within an individual reinforcing bar; results from the strain gauges will enable this type of experimental to analytical comparisons.

5.3.2 Strain Gauge Types

Each C-shaped wall was heavily instrumented with quarter bridge strain gauges. Two types of Texas Measurements Inc (TML) gauges were utilized: high-elongation 5mm gauges were affixed to the reinforcing bars before tying the rebar cage and casting the concrete, and large general purpose 30mm gauges were applied to the concrete surface after curing. These gauge types are shown in Figure 5.2.

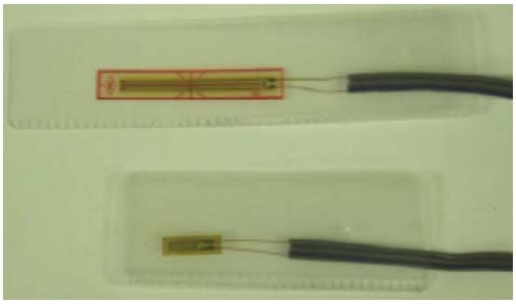

Figure 5.2: Concrete surface gauge (above) and steel reinforcement gauge (below)

5.2.1.1. Concrete Strain Gauge Layout

Concrete gauges are located vertically on the C-shaped walls as shown in Figure 5.3, those indicated in red were added to the instrumentation plan for UW 2 & 3.

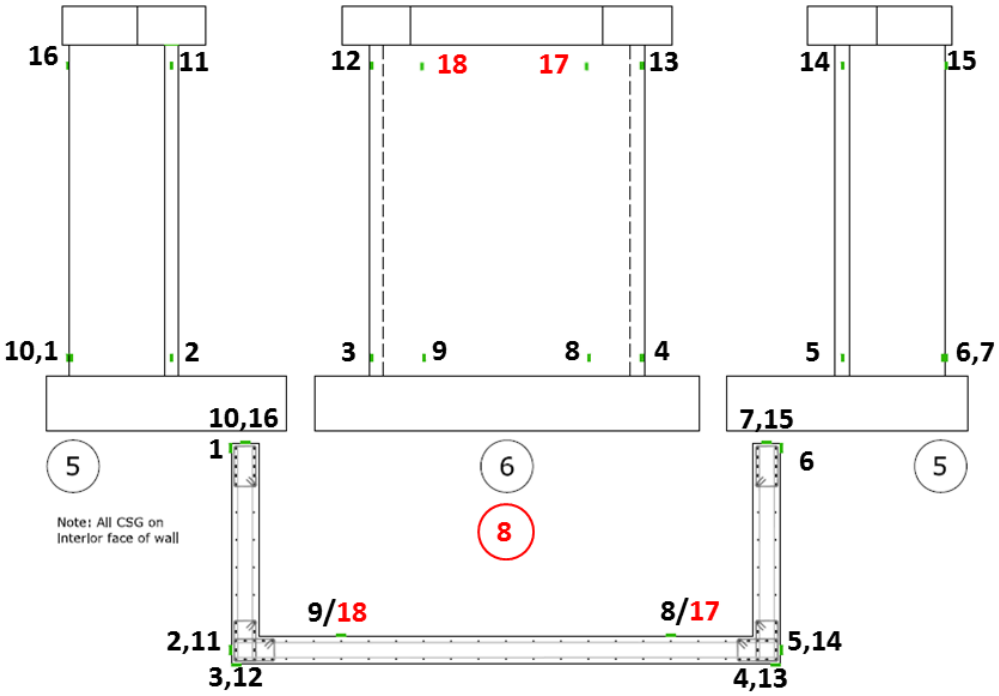

Figure 5.3: Concrete surface gauges (red indicates additions for Wall 6 & 7)

5.2.1.2. Steel Strain Gauge Layout

The internal steel gauges are applied at select locations to the longitudinal, horizontal, and stirrup reinforcement. As seen in Figure 5.4, one vertical bar in the boundary element at the back of each flange is instrumented while at the flange/web interface there are two vertical bars with gauges. In both cases, strain data can be collected at all three floors of the specimen. In the unconfined regions, each flange has gauges on one vertical bar and in the web at every fourth bar (though primarily concentrated in the first floor of the specimen).

The strain gauge layout for horizontal reinforcement can be seen in Figure 5.5, and similarly hoop reinforcement in Figure 5.6. For both these rebar types only the web and east flange were instrumented, as symmetric behavior was expected for the opposing west flange. Also of note is that stirrup gauges were primarily concentrated in the first floor region were the most significant deformations were anticipated.

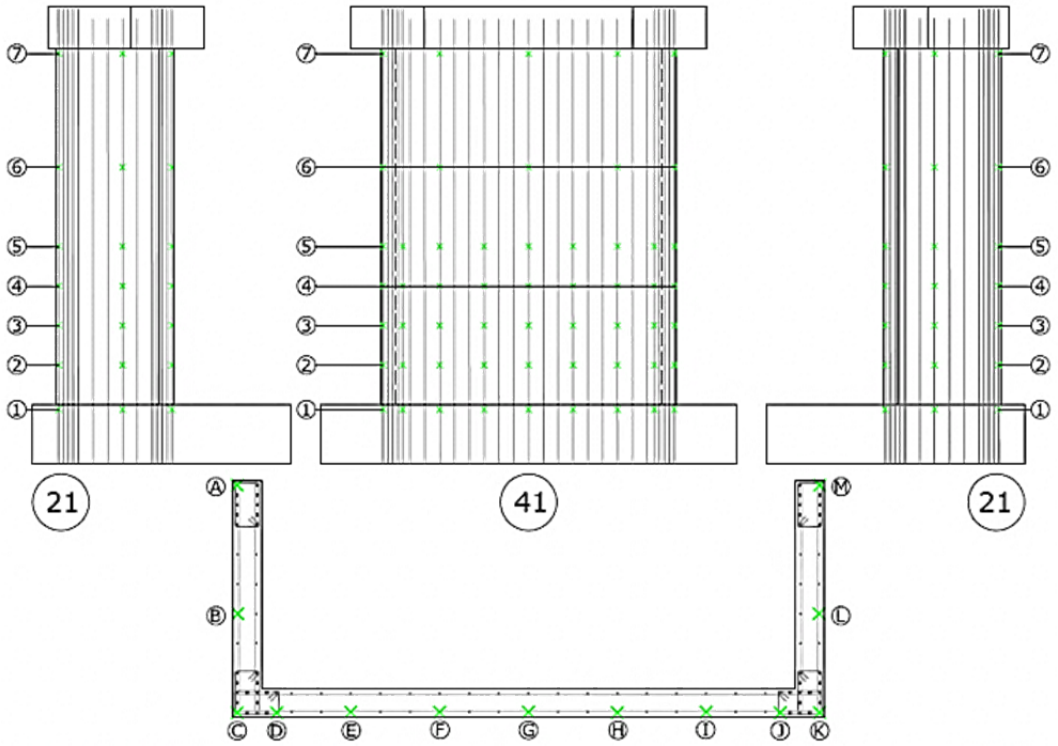

Figure 5.4: Steel gauges on longitudinal reinforcement

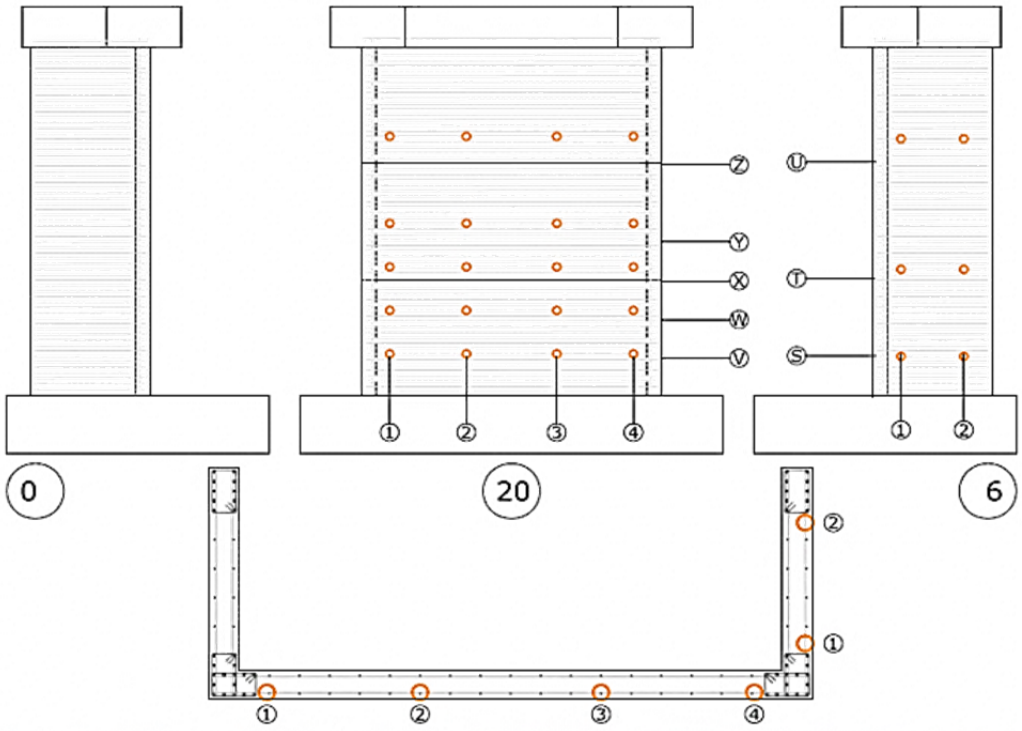

Figure 5.5: Steel gauges on horizontal reinforcement

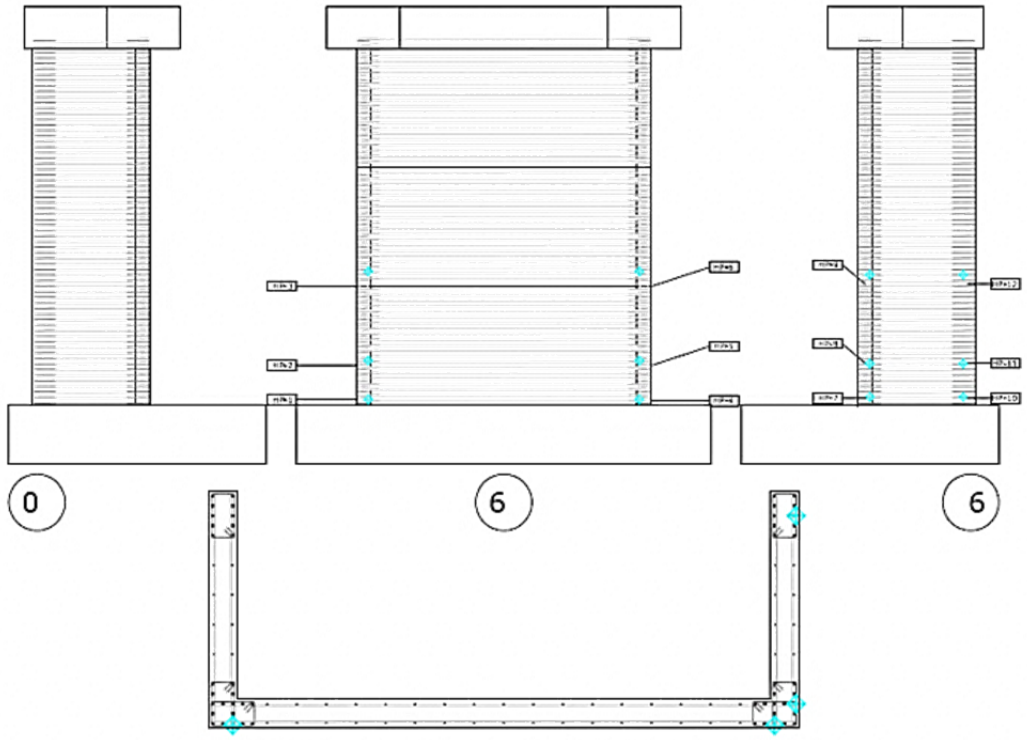

Figure 5.6: Steel gauges on stirrup reinforcement

5.3. Traditional Displacement Transducers

5.3.1. *Introduction*

A variety of traditional displacement transducers including linear variable displacement transducers (LVDTs) and string potentiometers are utilized to measure absolute and relative displacement of the test specimen. Perhaps the most critical application of this sensor type is the high-resolution linear potentiometers –referred to as control sensors - that provide information about specimen movement that can be used to determine elastic deformation in the system and is incorporated into the load control algorithm to reach a displacement target. Other absolute displacements are measured along the height of the wall in the in-plane (strong-axis) and out-of-plane (weak-axis) directions using string potentiometers. Also, LVDTs are applied to the foundation to monitor any occurrences of specimen base slip and rotation. Aside from absolute displacement measurements, relative deformation of the specimen is captured by a grid of linear potentiometers affixed to the rear face of the C-shaped walls at all three floors.

5.3.2. *High-Resolution Linear Potentiometers for Load Control*

The deformations measured in the LBCB boxes may include a component of deformation in the steel reaction frame of the loading unit that is not being realized on the test structure. A series of high-resolution linear potentiometers are placed on the specimen to measure the actual deformation of the test structure. A mathematical transformation of the change in lengths of all sensors can be used to determine the Cartesian six DOF position. The control sensors are strategically located to be able to capture each DOF. This six DOF position is part of an external control loop ensuring the commanded displacement history is realized on the test structure.

The typical control sensor layout for the tests is shown in Figure 5.7.

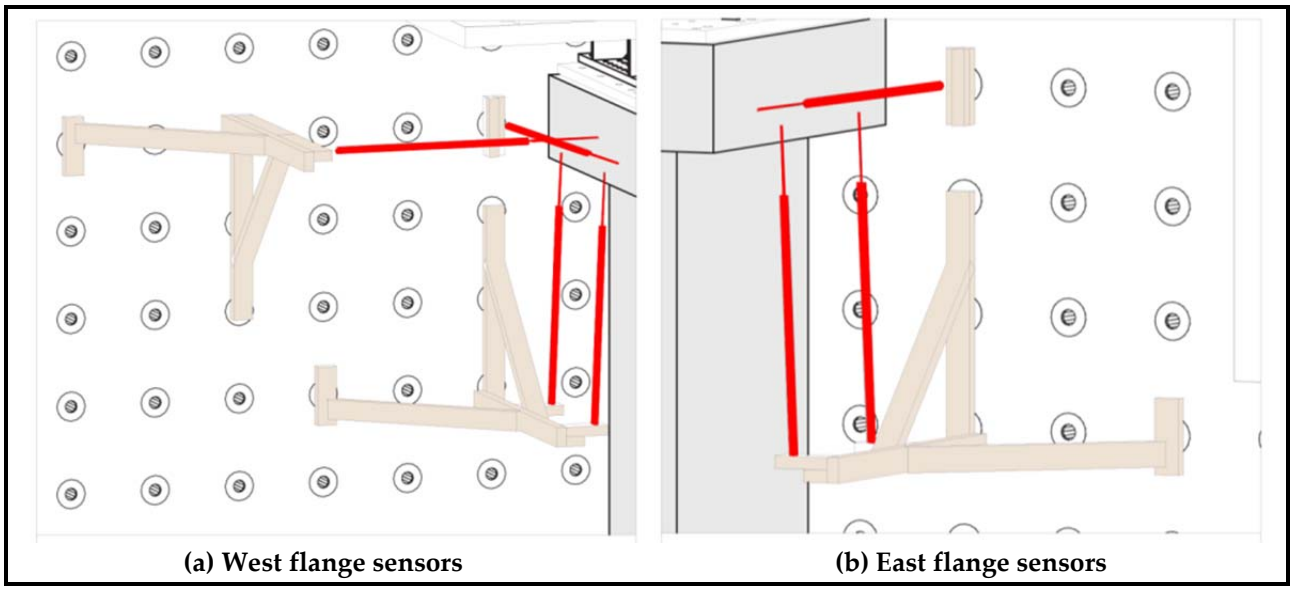

(a) West flange sensors (b) East flange sensors

Figure 5.7: Control sensor diagrams

5.3.3. *Absolute Displacement Measurements*

5.3.3.1. String Potentiometers

A total of twenty string potentiometers were employed in each of the C-shaped wall tests, these have standard tension cables and have a full stroke of either 5 or 25 inches. Five were installed along a vertical line at each flange/web interface and were oriented to measure strong-axis displacement, while five were attached to the back of each flange to monitor weak-axis motion. The layout is illustrated in Figure 5.8.

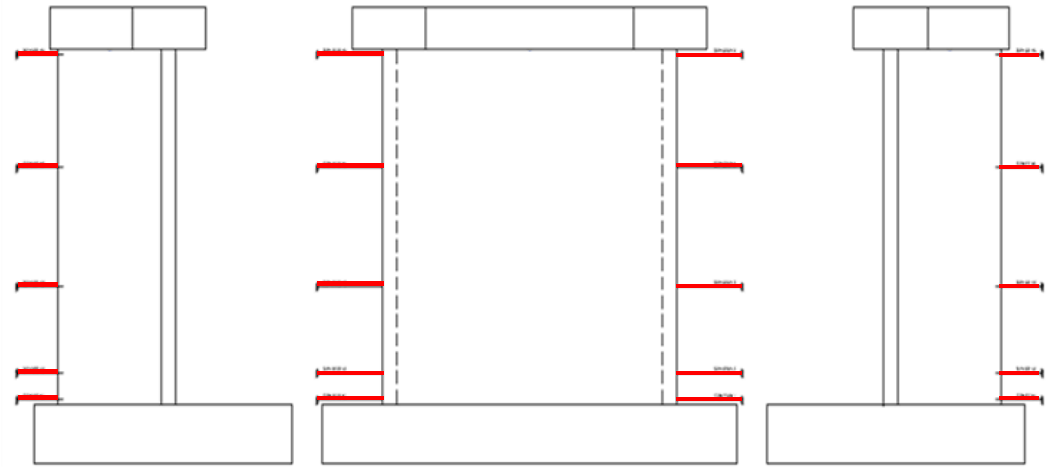

Figure 5.8: String Potentiometers

The string potentiometers have an important role in tracking the global motion of the wall specimens during testing. In particular, the third floor sensors provide the redundancy necessary for researchers to verify that control sensor measurements reflect the correct displacement magnitude and direction. This

is a critical check since the values from the high-resolution linear potentiometers are used in calculating whether the target displacement has been achieved. Furthermore, having these sensors to monitor absolute movement along the two primary axes insures that while cycling in one direction the displacement in the perpendicular direction remains at zero (or at a constant value) based upon the given loading protocol.

With some amount of post-processing, the data gathered from string potentiometers attached to the flanges can provide information about rotation of the specimen and serve as an indicator of undesired torsion. On occasion, researchers were making these evaluations in real-time to insure that the specimen was being loaded and behaving as anticipated. Following testing, absolute displacements from these sensors can provide insight about deformation along the height of the wall throughout the testing history; also, they can be utilized for such tasks as flexural stiffness evaluations.

5.3.3.2. LVDTs to monitor Foundation Slip/Rotation

In total there are four LVDTs mounted to the foundation block, two on each flange side where one is oriented vertically and the other horizontally. These sensors have a spring loaded probe shaft of 2 or 4 inches and are used to monitor any slippage at the specimen connection to the strong floor. In the C-shaped wall tests it is critical to maintain fixity at the base, and any event where movement occurs at this interface would be important to capture. While this event is very unlikely, due to the high clamping force provided by the threaded rods post-tensioned to the strong floor, base displacement would have a significant effect on the test and so these sensors are installed to monitor that displacements remain unchanged.

5.3.4. *Relative Displacement Measurements*

On the reverse of the C-shaped wall, a grid of linear potentiometers was used to measure relative displacements over large gauge lengths. The measurement system was able to capture deformation data for both flanges and the web at all three floor levels. Gauges with a 1, 2, 6 or 8 inch stroke length were used based upon the predicted damage in a certain region and the gauge length that had to be spanned. The sensors are primarily oriented in vertical and diagonal directions, as shown in Figure 5.9. The gauges were mounted to a threaded post that is anchored in the wall using an eyelet fixture, in many cases the gauge length was achieved by fabricating aluminum extensions for these instruments.

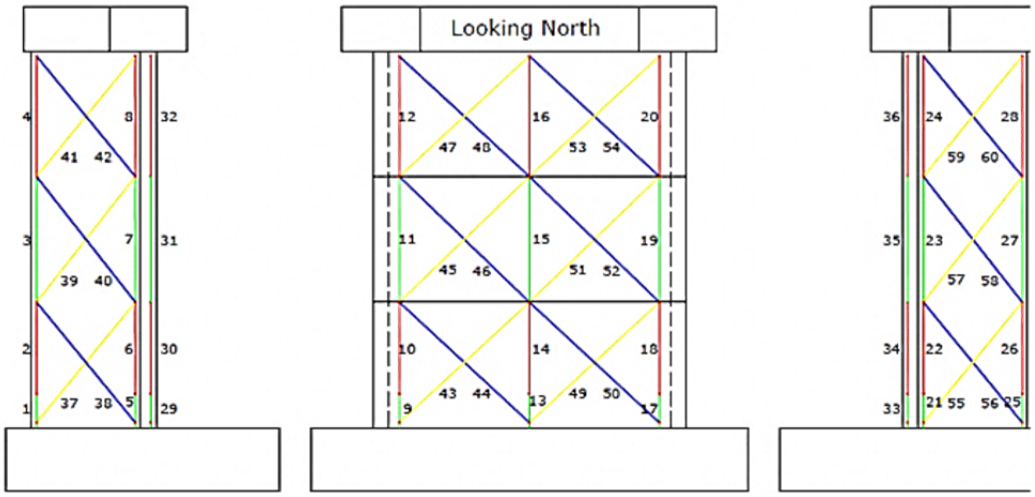

Figure 5.9: Linear Potentiometers for Relative Displacement Measurement

During testing the linear potentiometers provide the most accessible measure of average shear deformation for the wall specimens. With some calculation the difference in displacement readings from vertically oriented linear potentiometers, either comparing those on front and back of flanges or on each side of the web, can be utilized to determine the rotation about the x- or y-axis which can be correlated to the bending behavior in the weak and strong axes. After the test, the relative displacement data can be used to calculate average strains across the wall. This is particularly important for third floor strains since the Krypton system described in Section 5.5.1 does not cover the uppermost floor of the web or east flange of the wall specimens nor were there any photogrammetric targets present during Wall 6 to collect displacement data.

5.4. Advanced Instrumentation Methods

There are two non-contact measurement techniques employed in the C-shaped wall tests: the Nikon Metrology/Krypton Optical CMM system and close-range digital photogrammetry (UW 2 & 3 only). These are both employed to capture full-field displacement data that would not be possible using the traditional systems mentioned previously. By developing a grid pattern on the specimen using both LED emitters and coded photogrammetric targets, the X, Y, and Z coordinates of these points can be determined for each load step along the test history. Each of these targets can be treated as a node in a finite element model where the types of data that can be derived from the absolute displacement measurements can be quite similar to those from FEM analysis such as principal tension, compression, and shear strains.

5.5.1 Nikon Metrology/Krypton Optical CMM System

5.4.1.1. Introduction

There are a variety of benefits to using a dynamic motion measurement system like Krypton in a large-scale structural experimental project. The primary advantage being that researchers can track the three-dimensional displacement of a dense array of points, information that would otherwise not be feasible to capture using the traditional methods mentioned in previous sections. Utilizing Krypton on the bottom two floors of the web and east flange of the C-shaped wall specimens provides real-time data about the deformations that the specimen is undergoing.

During the earlier portions of the test this information can be utilized to insure that axial load is being distributed evenly across the specimen by comparing axial deformations across the wall cross-section. Also, the fact that these sensors are laid out in a uniform grid makes evaluations of rotation and assessment of bending behavior a relatively simple task. Another attribute of this system that the research team capitalized on was the ability to apply sensors while the test was underway. When advancing in the plastic loading regime, there is significant straining in the boundary element reinforcement for which the research team was interested in collecting more detailed data. Therefore, as concrete spalled off these areas and the reinforcement became accessible, sensors were applied directly to the rebar to observe the progression of yielding, buckling, and fracture.

Beyond providing a large density of data that can be readily assessed during testing, the post-test applications of Krypton measurements are vast. Each sensor in the grid array acts as a node would on an FEM model, and therefore one can use the collected measurements to calculate compressive, tensile, and shear strain fields. In previous tests in the Complex Walls project this information has been effectively communicated through videos; not only showing the straining behavior of a wall over the duration of the test, but allows for a way to easily draw comparisons between a set of similar specimen tests. Krypton data has also enabled researchers to evaluate crack widths and angles by coupling strain

information gathered by this instrumentation system with crack map data from still images. Using edge detection software, one can evaluate from a photograph the number of cracks present between rows of Krypton sensors and then utilize the strain data to determine the average crack width. This has been repeated for the entire duration of tests to understand damage progression. A full-field measurement system like Krypton opens the door for many possibilities. Looking beyond data analysis, measurements can be utilized as a method of assessing and validating computational modeling programs for reinforced concrete since the nodal displacements and straining calculated by these tools can be directly compared to those observed in the experiment.

5.4.1.2. Instrumenting with Nikon Metrology/Krypton System

The Krypton system has three cameras mounted to a fixed unit and uses triangulation principles to measure the position of infrared signals emitted by light emitting diodes (LED) mounted to the wall specimen. The Nikon Metrology/Krypton camera and data acquisition unit can be seen in Figure 5.10.

Figure 5.10: Nikon Metrology/Krypton K600 Optical CMM System

On each C-shaped wall two of these camera units were utilized, one that captured the bottom two floors for the web and another for the east flange side. A typical layout for the LEDs on each of this faces can be seen in Figure 5.11; as a note, the coordinate systems for the two Krypton cameras are independent of one another.

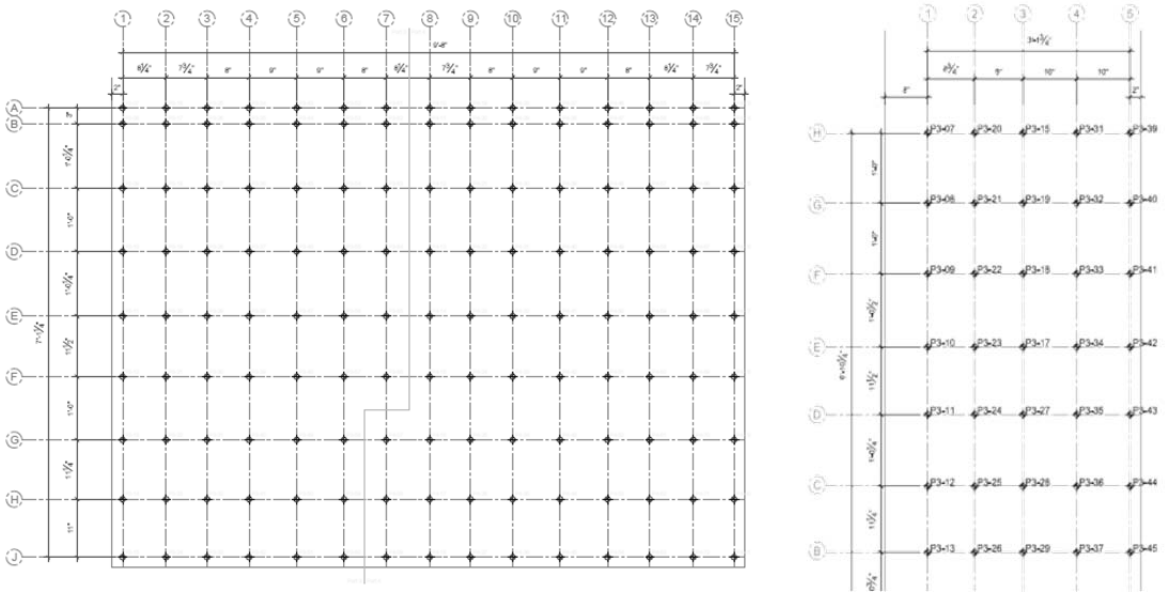

Figure 5.11: Typical Layout of Nikon Metrology/Krypton LEDs (left) web (right) east flange

5.5.2 Close-range Digital Photogrammetry

5.4.1.3. Introduction

Photogrammetry is a method of extracting three-dimensional coordinates of specific points on an object's surface. This technique works based upon the principles of feature recognition and triangulation. The procedure involves obtaining several digital photographs of the object and processing these images through a photogrammetric software package. These programs first recognize the special features in images, then cross-reference photographs to create relationships between corresponding features in at least three other images to be able to finally solve spatial locations for points on the object.

During the test, images are taken of the photogrammetry targets at the completion of each load step and these records are stored for later post-processing. Unlike Krypton where the displacement of the LEDs can be tracked in real-time, this non-contact method requires some effort to associate all the images with the appropriate camera calibration files and batch process all the photographs. On the other hand, it provides valuable information that cannot be captured within the Krypton coverage area. Photogrammetry targets were used to cover all three floor levels of the specimen where Krypton can only monitor the bottom two, and this allows for a more complete record of deformation during the test. Results gathered from earlier tests on the Complex Walls project have validated the accuracy of the photogrammetric system, and having access to XYZ displacement data from a uniform grid of targets has enabled researchers to develop videos to illustrate various types of straining behavior and illustrate the global displacement of the structure over the course of the loading.

Furthermore, photogrammetry enables the vital task of creating crack maps. In reinforced concrete, cracking is an important indicator of the flow of forces, and during the test researchers pause when entering new displacement levels to manually mark these cracks on the wall. Using the targets that appear on the wall as reference points, a series of photographs can be stitched together for a particular load step. After merging the images, it is necessary to eliminate the noise in the image and trace over the cracks using a photo-editing tool. Then using the displacement information for the initial position of

the targets on the wall, these cracks can be transformed back from their currently deformed to the original undeformed coordinate system. Not only can the crack maps be used to create films that provide insight into damage progression, the still images can also be examined and used to extract information such as crack angles and width.

5.4.1.4. Instrumenting for Photogrammetry

For C-shaped wall tests UW 2 & 3 a photogrammetric software package called PhotoModeler was utilized. This system as a library of target types from which researchers selected the ringed automatically detected (RAD) coded type as allows for a greater number of unique targets and exhibits more robustness in the solution process. Both the west flange and web were instrumented with a grid of these 2-3/4 by 3 inch targets that were generally spaced at 9 inches horizontally and 11-12 inches vertically along the height of the wall, resulting in a total of 260+ measurement locations. The target itself consists of a 12mm diameter high contrast dot that has a distinct ring pattern around it which can be automatically detected and referenced between photos by PhotoModeler. To capture the movement of these targets throughout the test required eleven calibrated high-resolution still cameras. Six Nikon D90s took images of the web, while four Nikon D80s were used to cover the west flange. Also critical to the photogrammetric project is the use of reference targets, both for the web and flange a fixed bracket is set up with three targets oriented perpendicularly to establish the x- and y-axis of the target coordinate system. These targets remain stationary throughout the duration of the test and are utilized in the solution process to determine the motion of the measurement points on the wall specimen. Figure 5.12 shows snapshots of the PhotoModeler solution for camera locations and target layout used for Wall 8. While Figure 5.13 shows the actual photographs taken by each still camera and how it contributes to solving the positions of the points on the specimen.

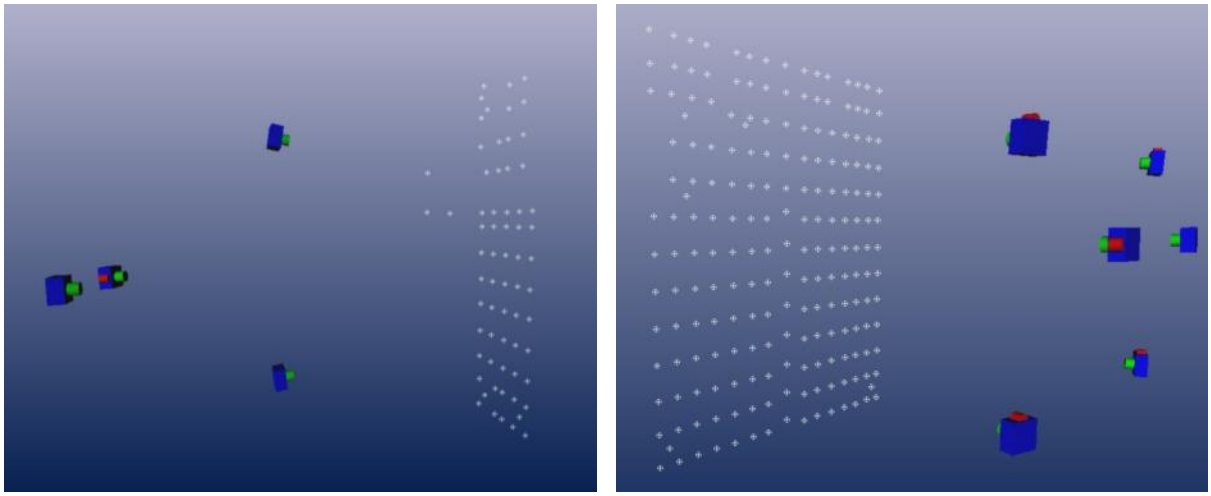

Figure 5.12: PhotoModeler Solution for camera statations and targets (left) west flange, (right) web

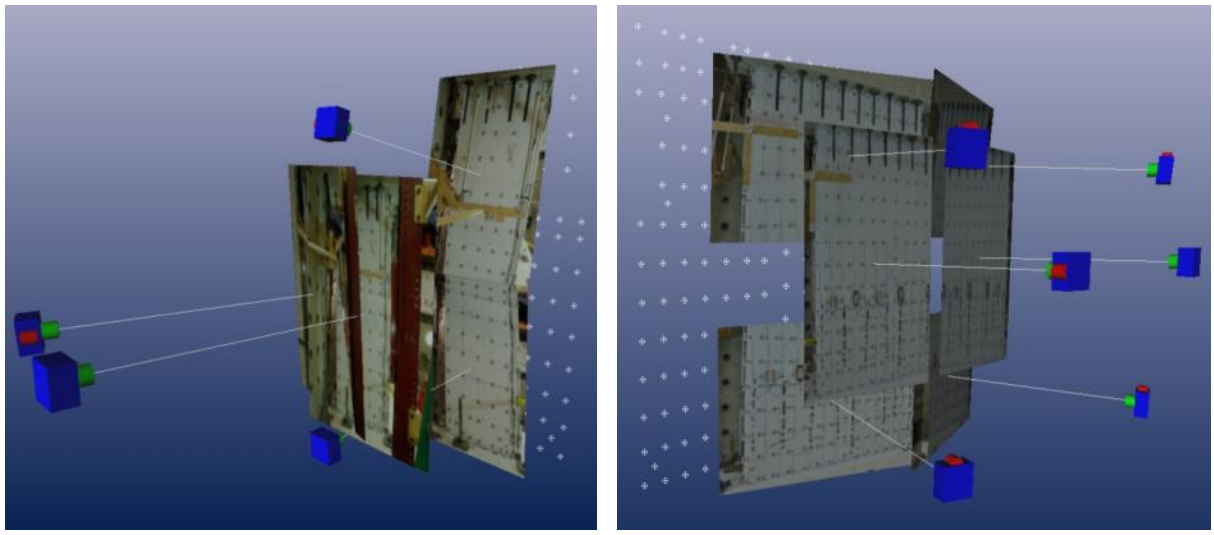

Figure 5.13: PhotoModeler Solution showing individual image contribution (left) west flange, (right) web

5.5. Other Documentation Methods

5.6.1 Introduction

Aside from the instrumentation techniques, previously mentioned in Section 5, that collect quantitative data regarding specimen performance, the research team has also taken advantage of array of photography and video equipment to monitor and document changes in specimen behavior.

These records are used during testing by the research team to track progression of damage over the loading history, at times even making comparisons between current and prior C-shaped wall tests to contribute to decisions regarding the loading protocol. They are also of value when critical team members cannot be present in the lab, but need to examine specimen behavior to participate in vital discussions. Following the test, it is these forms of visual documentation that provides the most insight when presenting to the larger research community, and supplements the quantitative measurements that have been recorded and analyzed.

5.6.2 Roaming Camera

One of the primary forms of recording critical events was using a roaming camera. This is a Nikon D90 variable focal length lens that enabled the researchers to track the location, orientation, and widths of significant cracks that developed on the wall; document the separation at the wall/foundation interface; monitor the onset and progression of concrete spalling or delamination; and capture reinforcement buckling or fracture. These close-up images were of particular value to inform off-site PIs in the development of damage and aid in determining future load cycles; furthermore, roaming camera photographs have been used extensively in presentations to share the observed damage seen in these wall tests with the greater research community.

5.6.3 Still Cameras

As already mentioned in Section 5.3.2 regarding close-range digital photogrammetry, still cameras play an important role in recording cracking and spalling throughout the test. Beyond the cameras used for photogrammetry on the web and west flange, three additional Nikon D80 cameras employed in C-

shaped wall tests UW 2 & 3: one which captures the overall behavior of the web and two positioned on the east flange. These are also used for a similar purpose of the roaming camera images- to inform off-site team members and share test results with other researchers – but provide a more global, rather than localized, view of damage.

5.6.4 Web and Video Cameras

During C-shaped wall test UW 2 & 3 two web cameras were positioned behind the C-shaped wall to allow researchers to monitor the damage that occurred at the interior corner of the boundary elements, at the base of the web/foundation interface, as well as any spalling that may affect the performance of the linear potentiometers mounted in these regions. Due to the limited clearance to see behind the wall and the fact that safety concerns prohibits researchers from making physical observations of the rear of the wall during loading, these two stationary web cameras were dedicated to this region. Additionally the NEES laboratory is equipped with multiple web cameras that can be maneuvered by the research team to point out or examine damage. This is especially valuable to make observations during loading steps or for off-site PIs to stay abreast of any new developments.

In the C-shaped wall tests video cameras were utilized upon entering the plastic regime of the loading protocol. These are primarily focused on the boundary elements located at the web/flange interface to capture yielding, buckling, and fracture of reinforcement; spalling and subsequent loss of confined concrete in these regions. Essentially this is a method of tracking damage as failure is being approached. Included in these videos is often recorded narration by the researchers to indicate particularly important events.

6. Wall 6 Experimental Results

6.1. Overall observations

The first C-shaped wall test provides great insight into the strong axis behavior of the specimen. The response was governed by flexure as the loss in load carrying capacity was precipitated by rupture of the longitudinal #4 bars in the boundary elements. Nearly all longitudinal #2 bars in the web and center of each flange are believed to have been ruptured. After the #2 bar ruptures a significant portion of the deformation was observed to be carried by sliding along the web. The sliding component is clearly visible in the load-deformation hysteresis and is responsible for a significant damage to the centers of each flange and a very large separation between the web and corner boundary element.

6.2. Overall hysteresis and key points of behavior

The load-deformation hysteresis of Wall 6 is presented in Figure 6.1. The Figure also shows the key points along the load-deformation curve corresponding to first yielding, spalling, buckling and fracture.

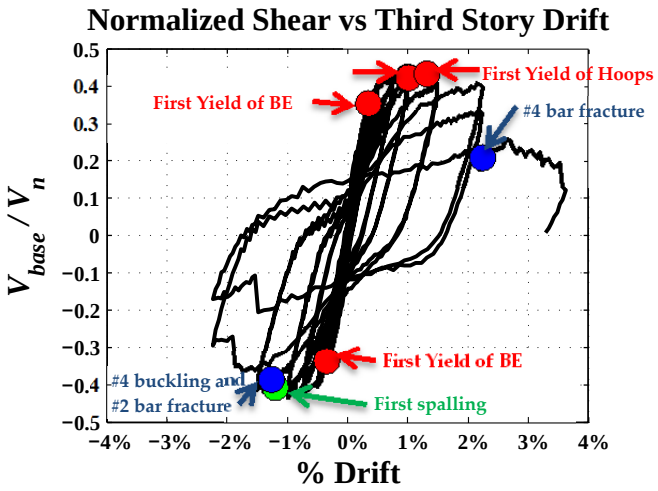

Figure 6.1: Wall 6 load deformation with key points of history

A plot of the base moment normalized to the section nominal moment is shown in Figure 6.2. The calculated nominal moment strengths using the measured material properties are provided in Table 9-1.

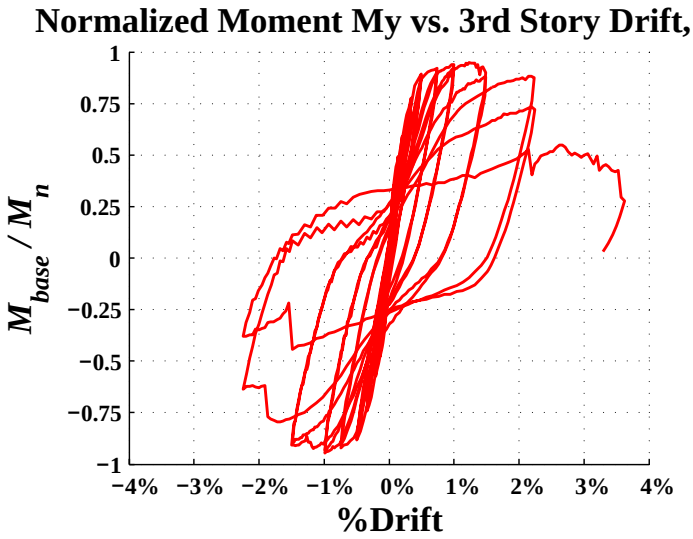

Figure 6.2: Wall 6 normalized moment hysteresis

6.3. Damage Narrative and Photos

6.3.1. ***Substantial Yield at Dx = 0.5" (0.35%)***

Shear, Fx = 177 kips, Base Moment, My = 4,979 kip-ft

The cracking pattern developed primarily in the cycles up to yielding. Cracking was initiated by flexural cracks in the first and second stories of the flanges. Inclined shear cracking then developed shortly after as well as additional uniformly spaced flexural cracks along the boundary elements in the web. The 0.35% drift cycle marked yielding of multiple #4 bars in the boundary elements in each direction as well as #2 bars in the flanges.

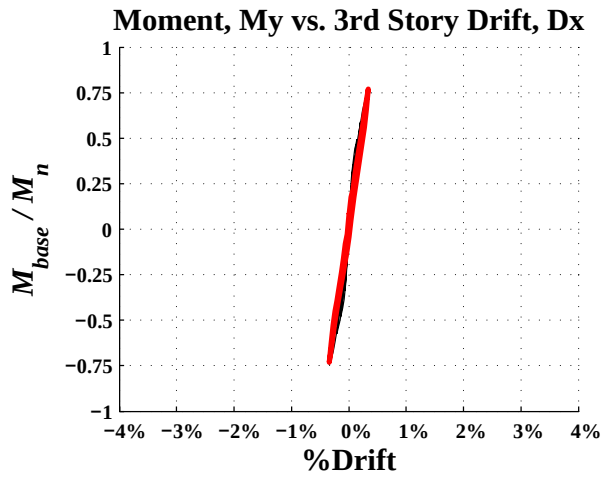

Figure 6.3: Wall 6 substantial yield hysteresis

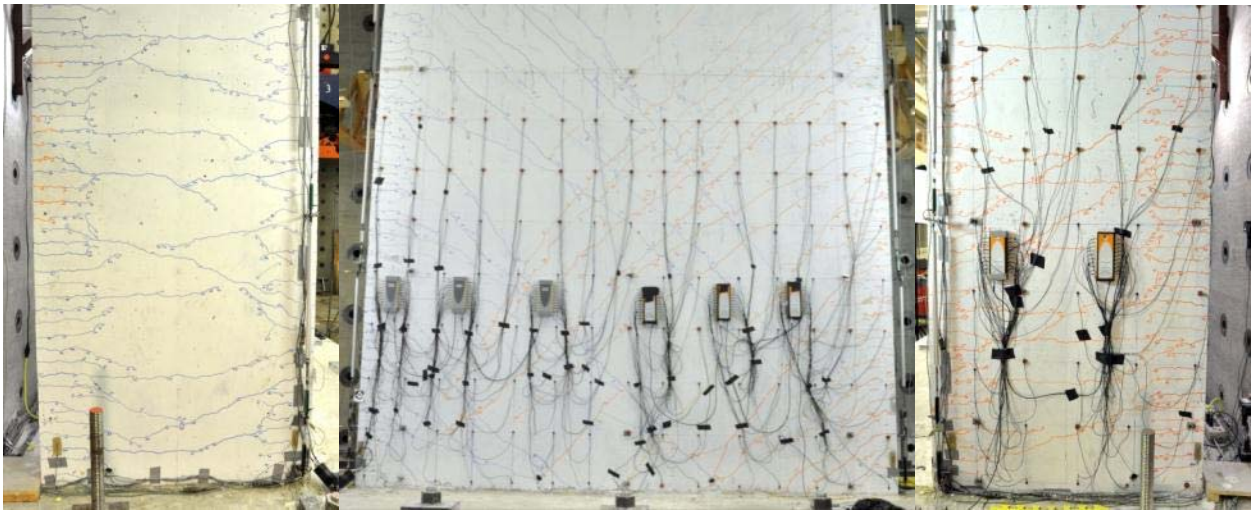

(a) West Flange ***(b) Web*** ***(c) East Flange***

Figure 6.4: Wall 6 substantial yield photos

6.3.2. ***Nominal at Dx = 1.08" (0.75%)***

Shear, Fx = 212 kips, Base Moment, My = 5,914 kip-ft

The nominal cycle at 0.75% drift marked flattening of the load-deformation curve and first significant softening of the wall specimen. The crack pattern is now fully developed and new steeply inclined compressive cracking was marked heading into each corner boundary elements. Vertical cracking has developed along the interior edges of the flange boundary elements; also, seperation at the wall and footing interface was observed.

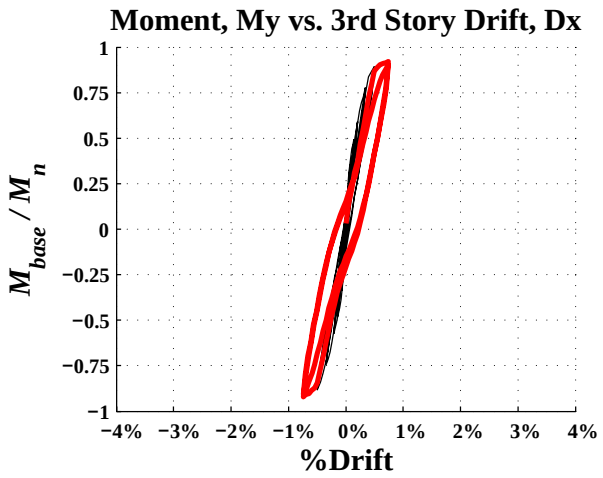

Figure 6.5: Wall 6 nominal hysteresis

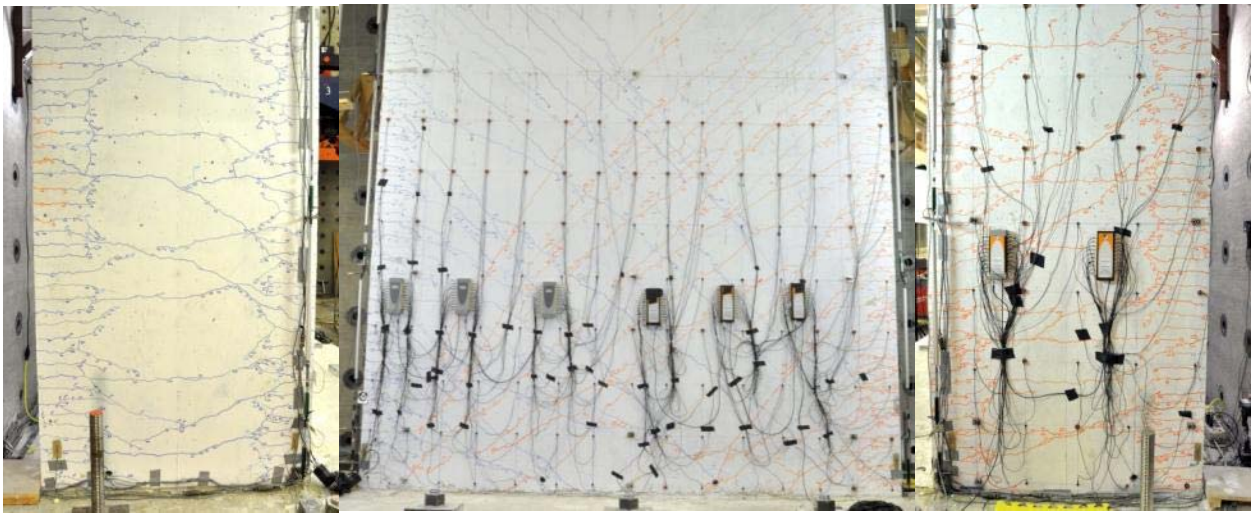

(a) West Flange ***(b) Web*** ***(c) East Flange***

Figure 6.6: Wall 6 nominal photos

6.3.3. ***Onset of Spalling at Dx = 2.16" (1.5%)***

Shear, Fx = 201 kips, Base Moment, My = 5,765 kip-ft

The cycle to 1.5% drift was highlighted by numerous ruptures of #2 vertical reinforcing bars along the web and centers of the flanges. Some loss of strength was associated with these ruptures. A significant component of the deformation was observed as sliding along the web and a pronounced separation between the web and Southwest boundary element. The horizontal bars ruptured along this separation. Significant spalling of cover was removed along both corner boundary elements; at this point #4 bars have begun to buckle in the East flange boundary element

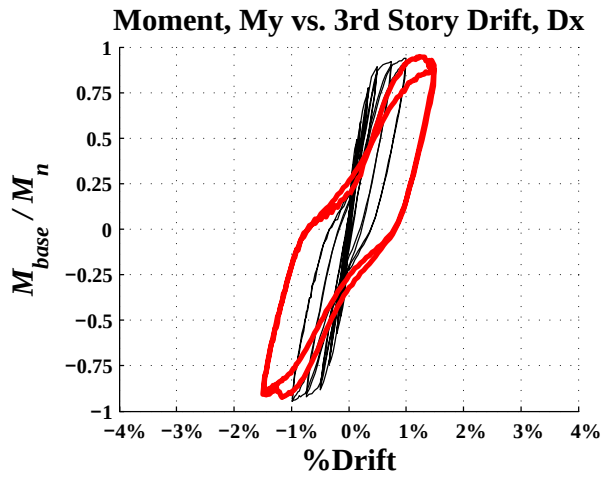

Figure 6.7: Wall 6 onset of spalling hysteresis

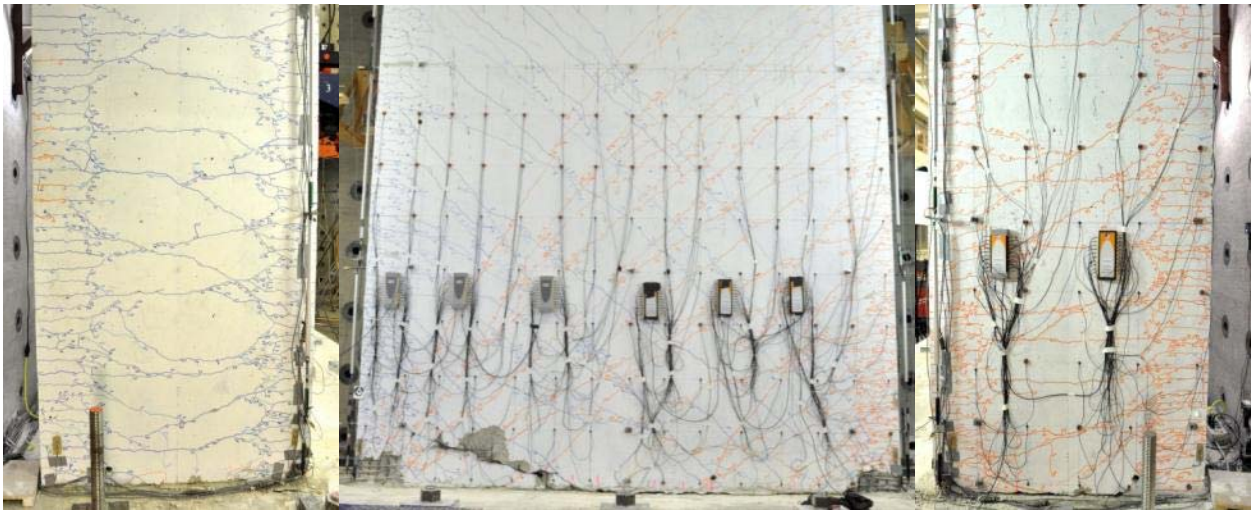

(a) West Flange ***(b) Web*** ***(c) East Flange***

Figure 6.8: Wall 6 onset of spalling photos

6.3.4. ***Bar buckling and rupture at Dx = 3.24" (2.25%)***

Shear, Fx = 198 kips, Base Moment, My = 5,612 kip-ft

The cycle at 2.25% drift marked the rupturing of #4 longitudinal bars and a failure of the specimen on the second cycle in the negative X direction. Continued buckling of longitudinal rebar in the spalled portions of the corner boundary elements and some loss of confinement was observed. New vertical compressive cracking is marked along the flanges flowing into the corner boundary elements. Spalled cover was removed at the boundary element toes and along the web. Significant sliding along the web resulted in spalling along the middle of the flanges due to out of plane shear. On the second cycle of 2.25% drift in the negative direction a large number of #4 bars were ruptured in the East flange resulting in the a significant drop in lateral load carrying capacity.

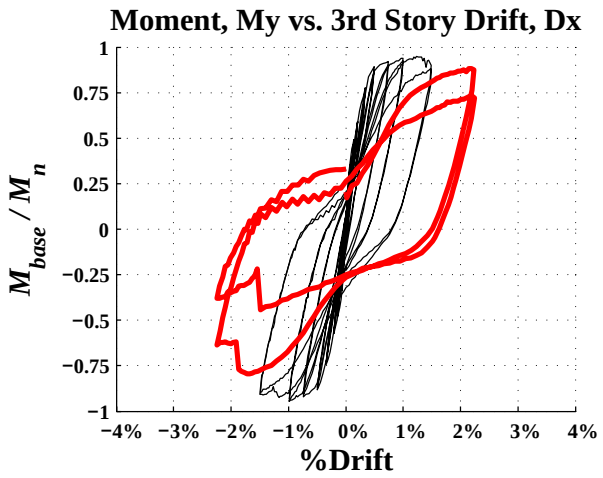

Figure 6.9: Wall 6 bar buckling and rupture hysteresis

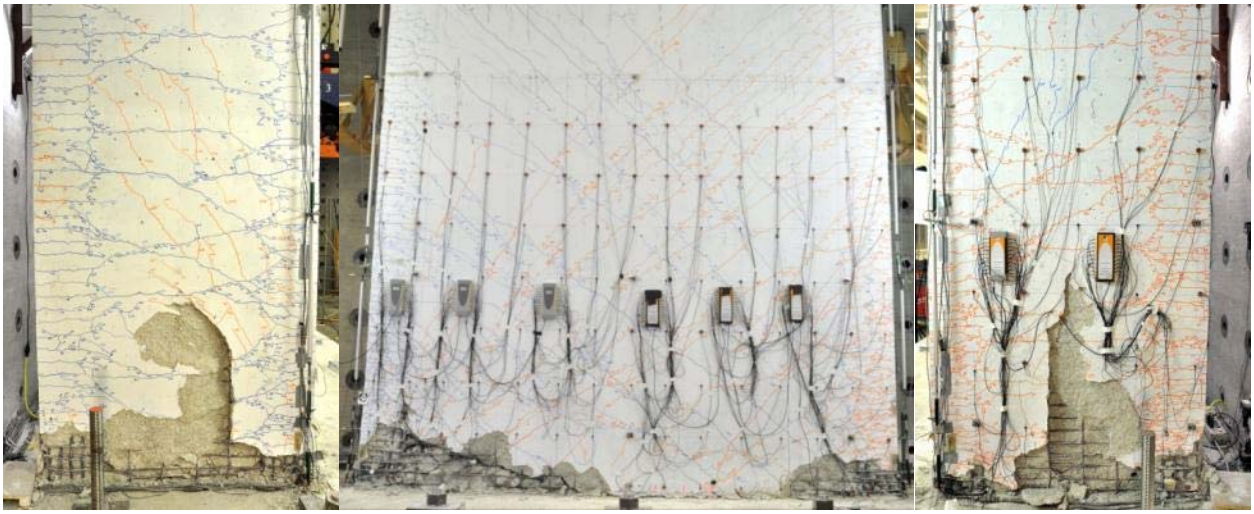

(a) West Flange ***(b) Web*** ***(c) East Flange***

Figure 6.10: Wall 6 bar buckling and rupture photos

6.3.5. ***Pushover failure at Dx = 5.1" (3.52%)***

After observing a failure in the negative X-direction during the second cycle at 2.25% drift, a pushover was performed in the positive X-direction until reaching failure at 3.5% drift. The separation between the web and Southwest boundary element grew large enough to see through the specimen with all horizontal bars ruptured in the bottom foot of the wall. The sliding behavior is evident in the offset between the bottom and top portion of fractured #2 bars along this diagonal opening. The wall exhibited severe buckling of longitudinal rebars along the East flange and a loss of confinement in both the corner and toe boundary elements. Successive rupturing of longitudinal rebars in the West flange resulted in the loss of load carrying capacity.

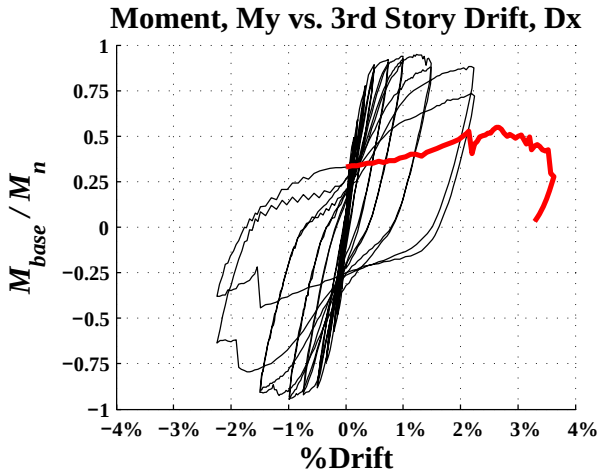

Figure 6.11: Wall 6 failure hysteresis

(a) West Flange ***(b) Web*** ***(c) East Flange***

Figure 6.12: Wall 6 failure photos

7. Wall 7 Experimental Results

7.1. Overall observations

The second C-shaped wall test provides great insight into the bidirectional behavior of the specimen. The response was governed again by flexure with the loss in load carrying capacity precipitated by the rupture of longitudinal #4 bars in the boundary elements. Nearly all longitudinal #2 bars in the web and center of each flange are believed to have been ruptured. The specimen exhibited less ductility in the X-direction due to the Y-direction loading and the fact that the boundary elements were subjected to twice as many cycles of loading as compared to the first test.

7.2. Overall hysteresis and key points of behavior

The load-deformation hysteresis of Wall 7 is presented in Figure 6.1. The figure also shows the key points along the load-deformation curve corresponding to first yielding, spalling, buckling and fracture.

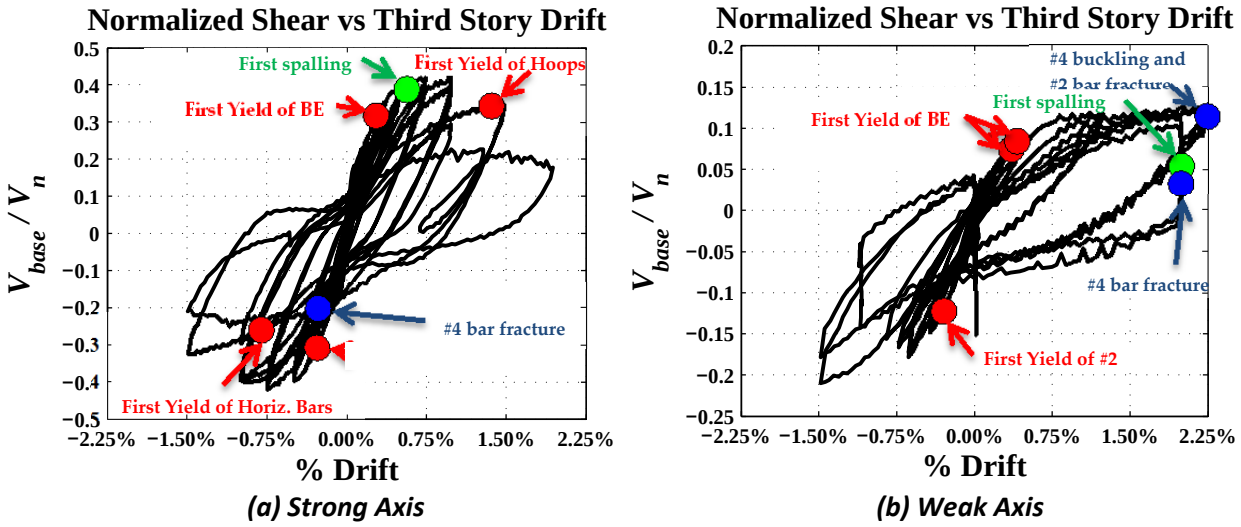

Figure 7.1: Wall 7load deformation with key points of history

A plot of the base moment normalized to the section nominal moment is shown for each direction in Figure 7.2. The calculated nominal moment strengths using the measured material properties are provided in Table 9-1.

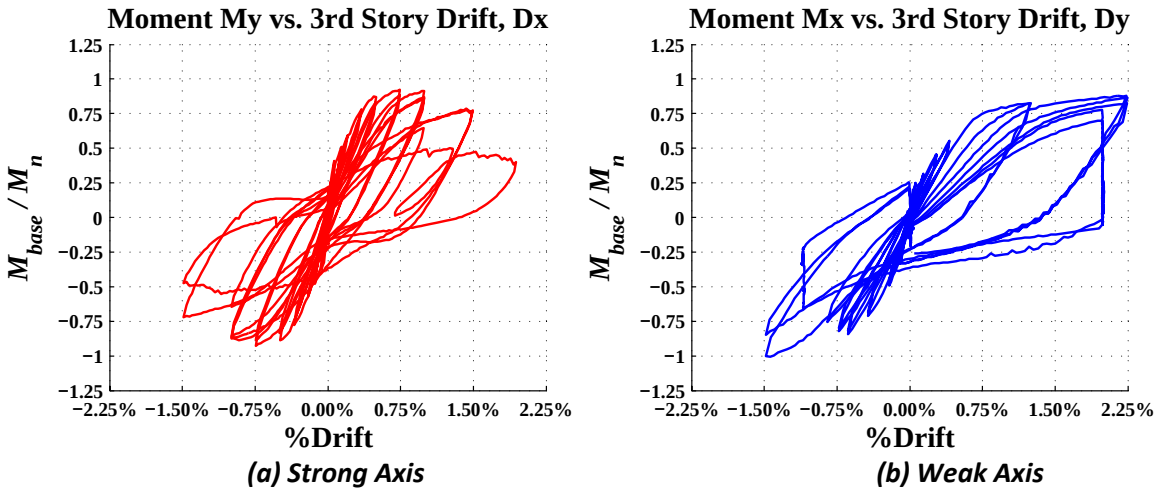

Figure 7.2: Wall 7 normalized moment overall hysteresis

7.3. Damage Narrative and Photos

7.3.1. *Substantial Yield*

Dx = 0.5” (0.35%), +Dy = 0.6” (0.42%), -Dy = -0.9” (-0.63%)

The cracking pattern developed primarily in the cycles up to yielding. Cracking was initiated by flexural cracks in the lower two floors of the flanges in the X-direction. The cracking pattern in both Y-directions consisted of reopening of X-direction flexural cracks. The 0.35% drift cycle marked yielding of multiple #4 bars in the lower two floors of the boundary elements in each direction as well as #2 bars in the

flanges and web. Seperation at the wall and footing interface across the entire span of the web was observed.

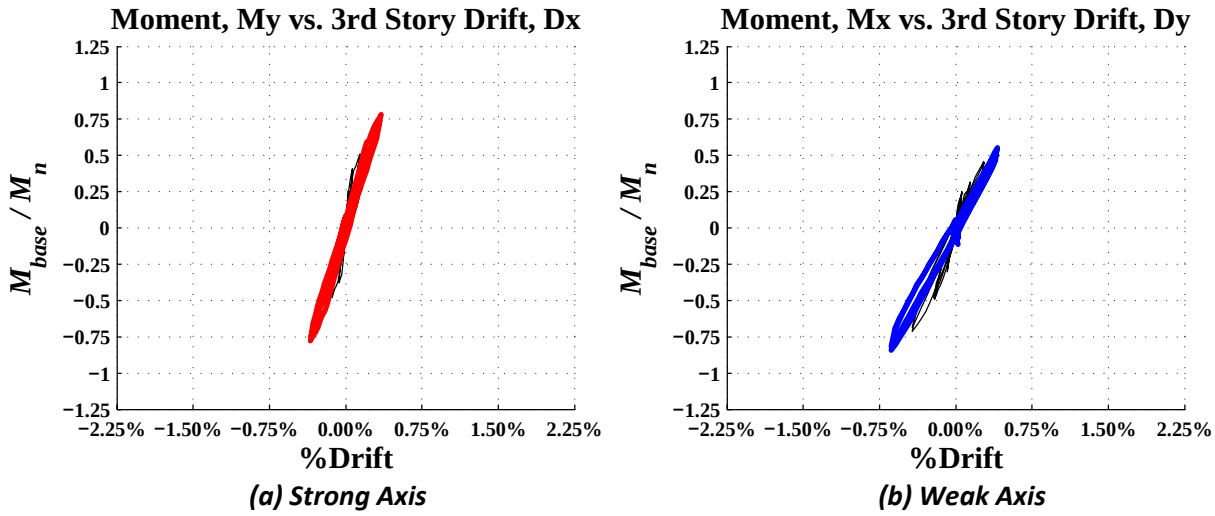

Figure 7.3: Wall 7 substantial yield hysteresis

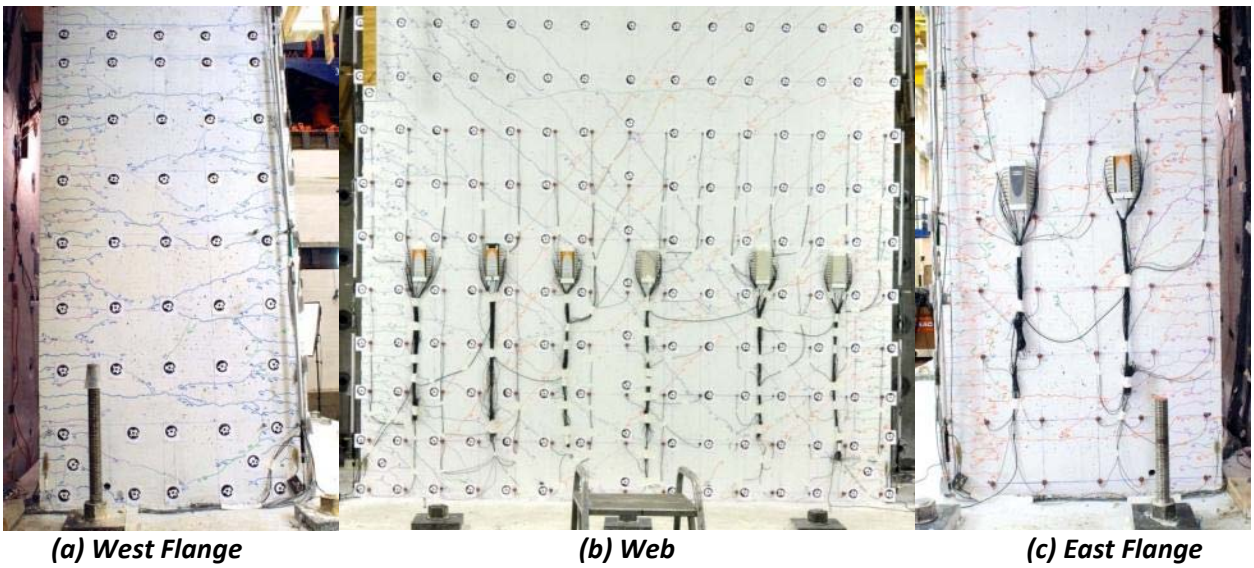

Figure 7.4: Wall 7 substantial yield photos

7.3.2. ***Nominal***

Dx = 1.08” (0.75%), Dy = +3.24” (2.25%), -Dy = -2.135” (-1.49%)

The nominal cycle at 0.75% drift marked flattening of the load-deformation curve in the X-direction and positive Y-direction, but no significant flattening in negative Y-direction. Significant softening of the wall specimen was observed in both directions. The nominal cycle resulted in spalling on both toes of the flanges at approximately two feet from the base. Some #2 bar buckling noted at the rear of the wall resulting in spalling of cover.

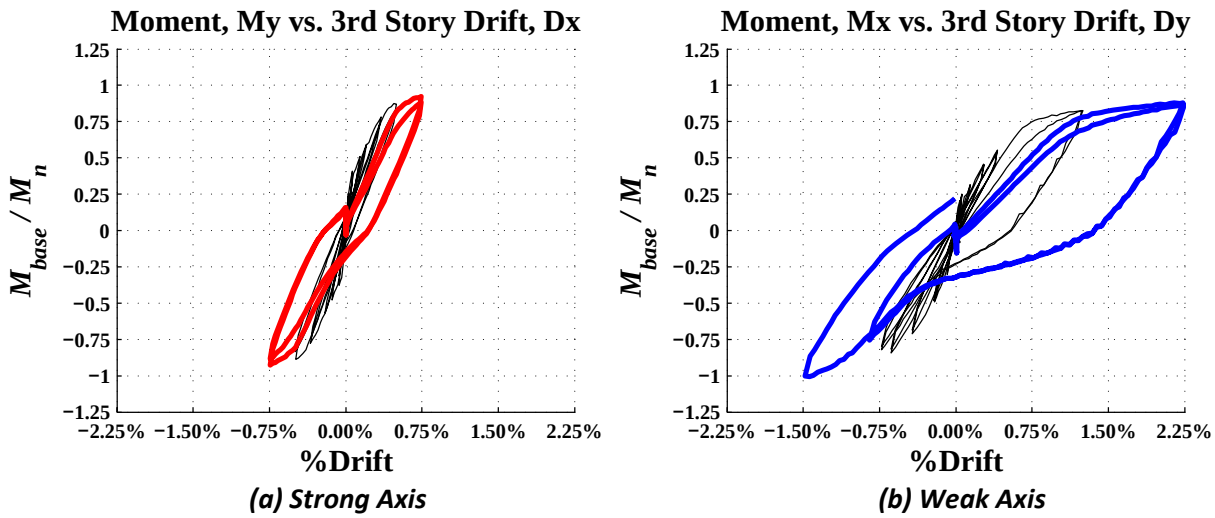

Figure 7.5: Wall 7 nominal hysteresis

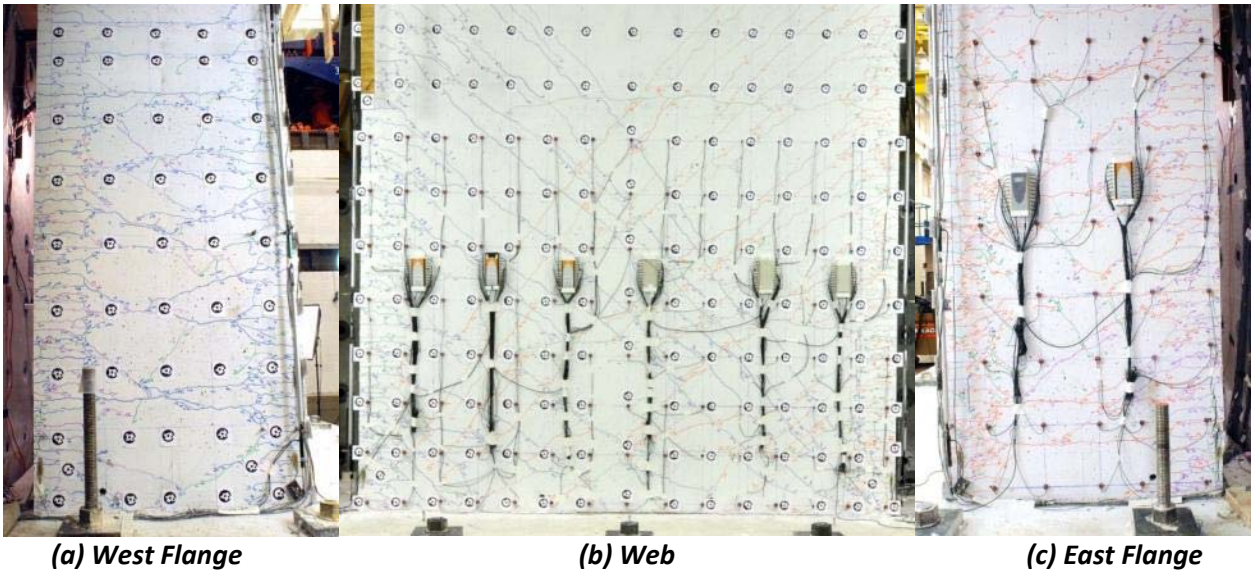

Figure 7.6: Wall 7 nominal photos

7.3.3. ***Bar buckling and rupture***

Dx = 1.44" (1.0%), Dy = +2.88" (2.0%), -Dy = -1.584" (-1.1%)

Due to reaching displacement capacity in the Y-direction, a cycle in the X-direction was completed at a constant Dy of 2.0% drift and a second cycle at a constant Dy of -1.1% drift to further increase the demand on the corners and toes. During the X-direction cycle additional separation was noted interface between the flanges and the footing. There was also significant spalling on the corner boundary elements during the cycle at positive Dy. Additional spalling was also observed on the toes of the flanges during the cycle at negative Dy, particularly on the East flange. Furthermore, this cycle showed significantly less stiffness than when completing at zero Dy and positive Dy. Rupturing of #2 bars observed along the center of the web, and buckling began to occur in the vertical bars of the boundary

elements. Sliding of the web at the interface between wall and footing was noted when evaluating Krypton displacement readings.

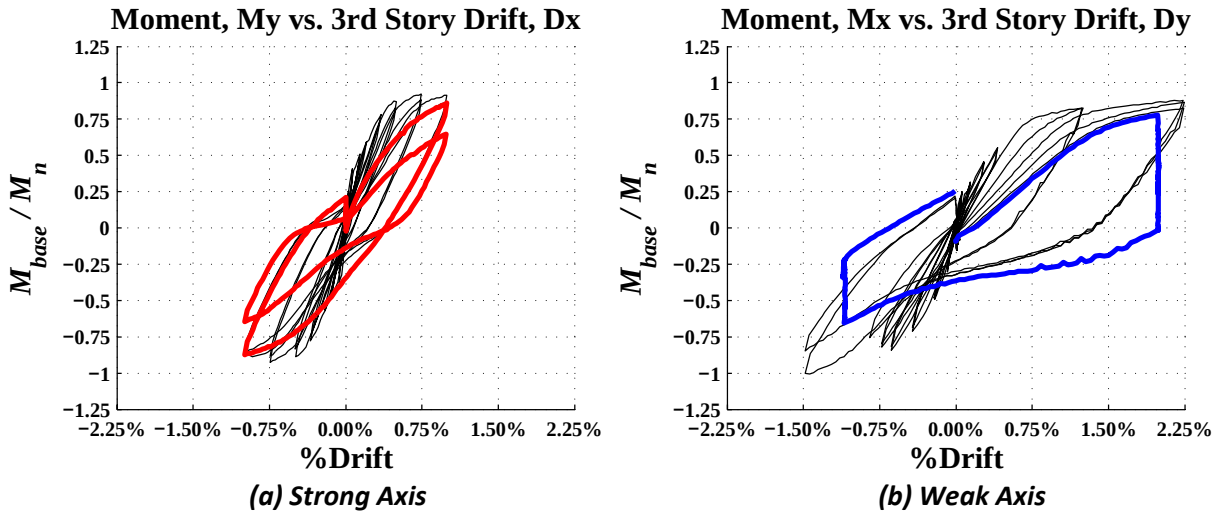

Figure 7.7: Wall 7 bar buckling and rupture hysteresis

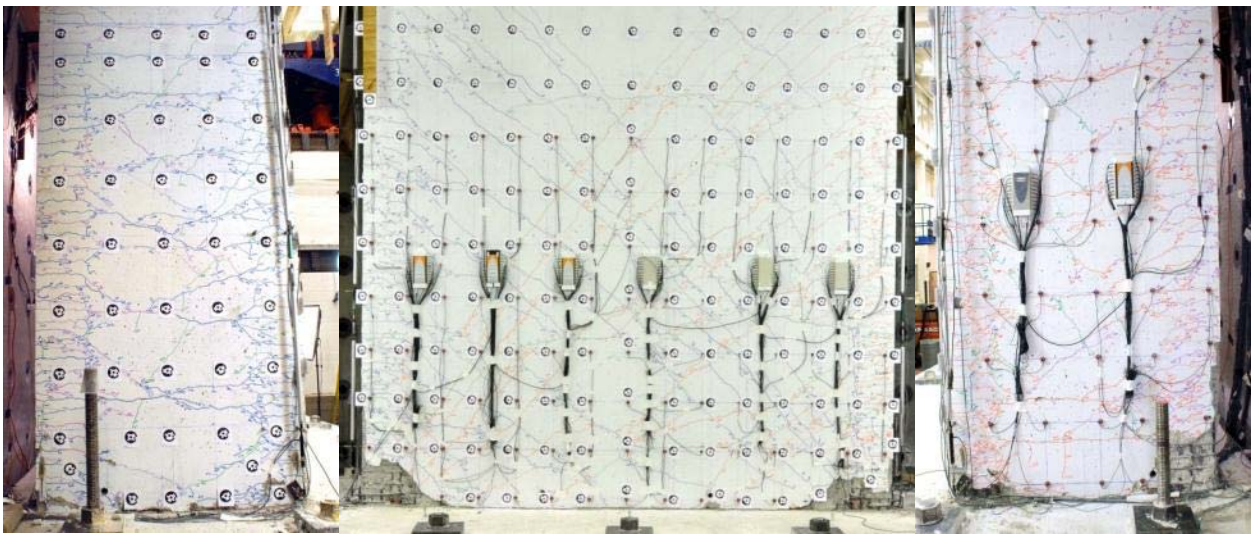

Figure 7.8: Wall 7 bar buckling and rupture photos

7.3.4. ***X Direction Pushover failure***

Dx = 2.80” (1.9%), Dy = +2.88” (2.0%)

The X-direction pushover held at the positive 2% drift in the Y and resulted in the additional rupture of approximately five #4 bars in the West flange boundary elements as well as additional spalling on the East flange. Almost no confined concrete remained in the corner boundary elements and the vertical rebar was extensively buckled; a hoop reinforcement in the Northeast corner boundary element ruptured The toe boundary element exhibited some additional spalling but not the same level of severe buckling or loss of confinement.

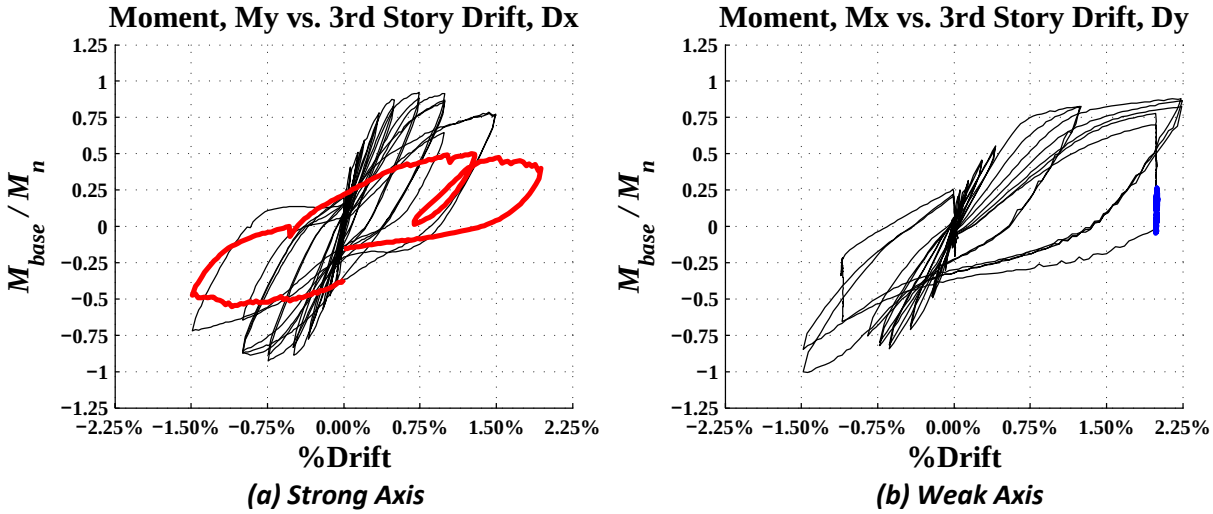

Figure 7.9: Wall 7 failure hysteresis

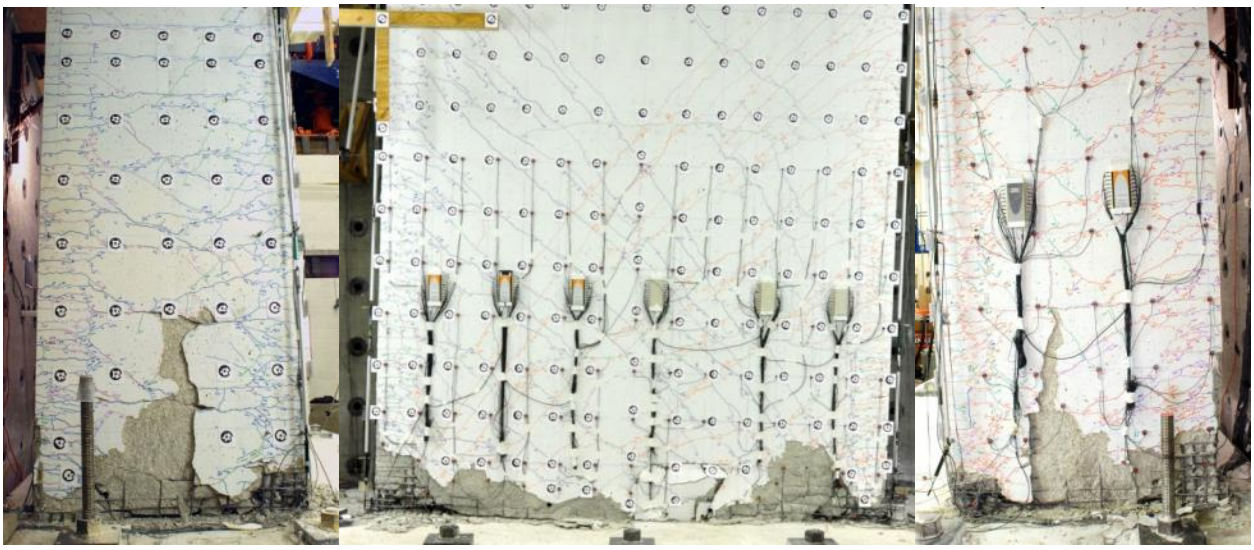

Figure 7.10: Wall 7 failure photos

8. Wall 8 Experimental Results

8.1. Overall observations

The pseudo-hybrid test of a coupled core wall system illustrated the significant impact that straining in the X-direction loading has on degrading the Y-direction stiffness. The X-direction response was unaffected by the Y-direction movements and with a damage pattern consistent with the previous tests. The weak axis response was governed by the compression pier and yielded much higher stiffness than the first bidirectional test due to the high axial load and reduced point of inflection. Failure was precipitated by rupturing of the #4 bars in the tension pier and a minor compressive failure in the compression pier.

8.2. Overall hysteresis and key points of behavior

The load-deformation hysteresis of Wall 8 is presented in Figure 8.1. The Figure also shows the key points along the load-deformation curve corresponding to key damage states of first yielding, spalling, buckling and fracture.

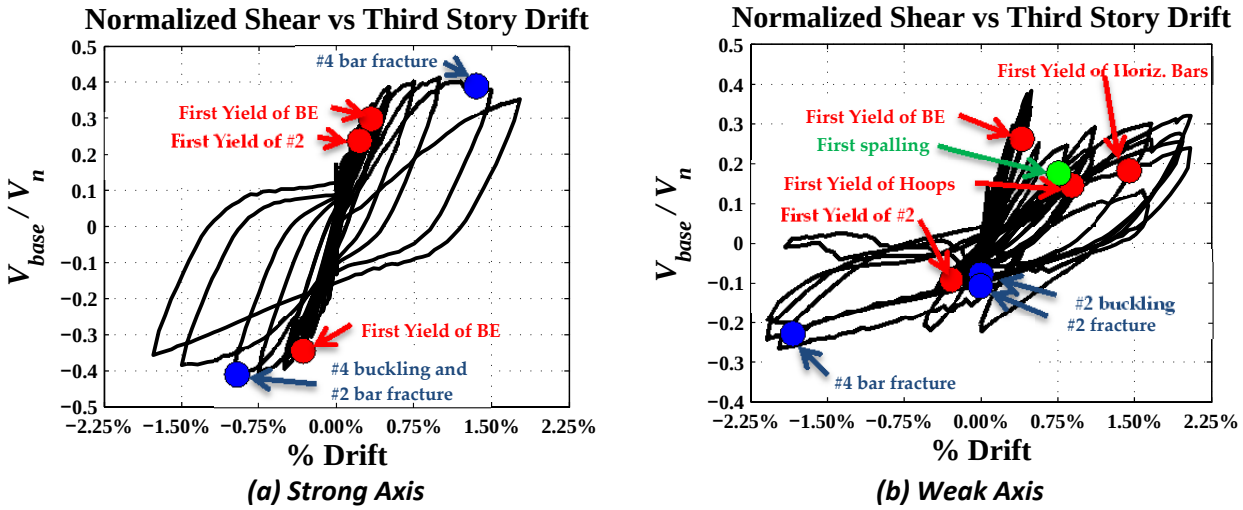

Figure 8.1: Wall 8 load deformation with key points of history

The nominal moment capacity was calculated using a sectional analysis at the applied axial load. For wall 8, the axial load varied in the weak axis direction due to the coupling moment and consequently has a varying nominal moment throughout the history. A moment – axial interaction curve is given in Figure 8.2 for the weak axis response of Wall 8. The heavy red line labeled "Comp. Pier Axial" represents the range of axial load imposed on the compression pier. A line was then fit to the range of axial load imposed on the compression pier to have a continuous function for evaluation of the nominal moment on the compression pier represented by the dashed red line labeled "Comp. Linear Fit". Similarly, the heavy blue line labeled "Tens. Pier Axial" represents the axial load imposed on the tension pier with a dashed blue line of best fit labeled "Tens. Pier Fit".

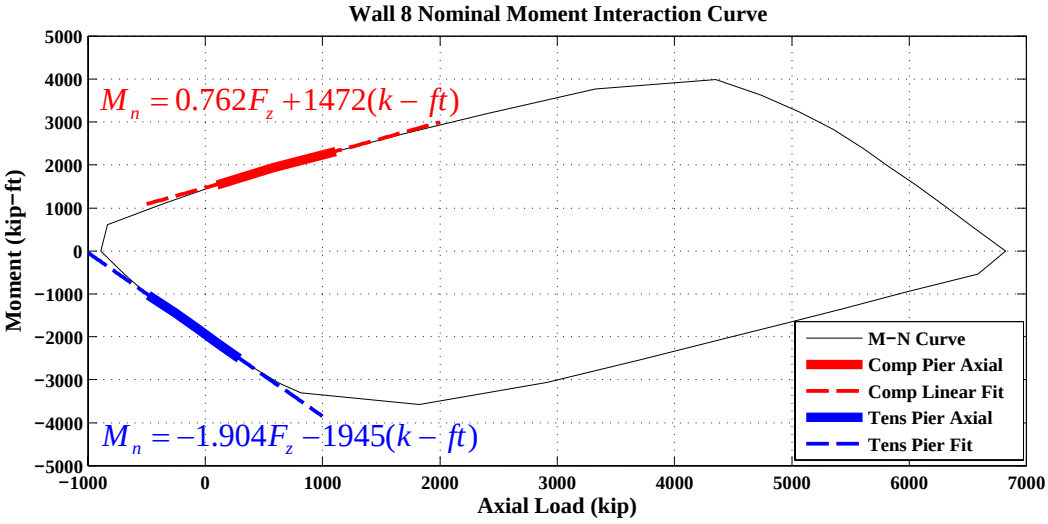

Figure 8.2: Wall 8 M-N Interaction Curve

For each step of the loading history, the normalized moment about for the weak axis was then calculated as follows:

For any load step i:

If compression pier (Fy > 0):

$$Mn_i = 0.762Fz_i + 1472(k - ft)$$

If tension pier (Fy < 0):

$$Mn_i = -1.904Fz_i - 1945(k - ft)$$

$$\text{Normalized base moment} = \frac{Mbase_i}{Mn_i}$$

A plot of the base moment normalized to the section nominal moment is shown for each direction in Figure 8.3.

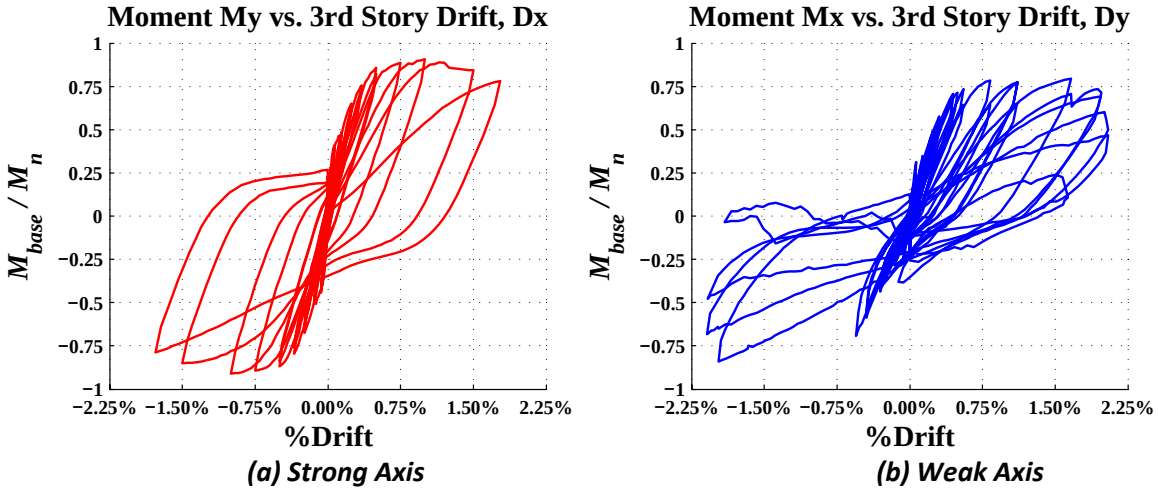

Figure 8.3: Wall 8 normalized moment overall hysteresis

8.2.1. ***Substantial Yield***

Dx = 0.5" (0.35%), +Dy = 0.65" (0.45%), -Dy = -0.65" (-0.45%)

Yielding across the flange boundary element vertical reinforcement was reached at the 0.35% drift level in the X and 0.45% drift in the Y. Higher strains were achieved in the X-direction cycle than the Y-direction. Yield was reached in the #2 bars in the web prior to yielding the boundary elements. The cracking pattern developed primarily in the cycles up to yielding, initiated primarily by horizontal and diagonal cracking from the X-direction loading. The cracking pattern in the positive Y-direction consisted of reopening of X-direction flexural cracks as well as new diagonal cracking.

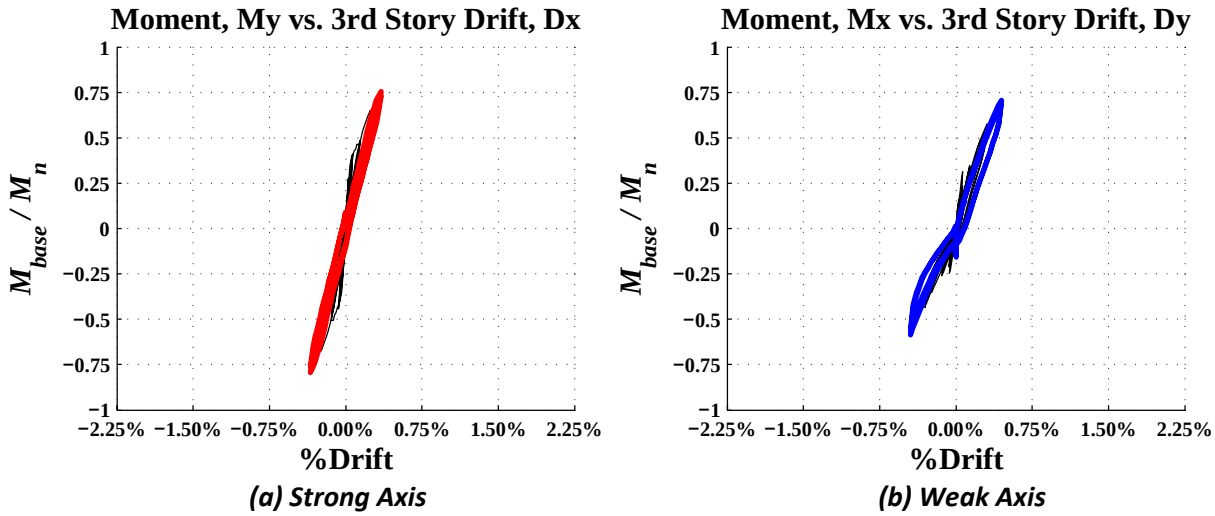

Figure 8.4: Wall 8 substantial yield hysteresis

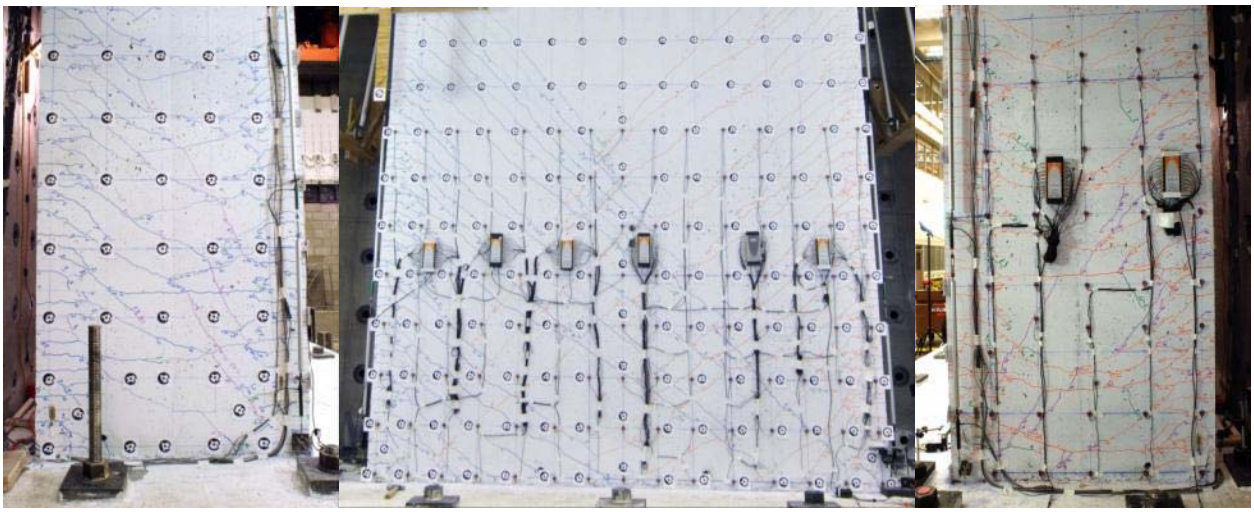

Figure 8.5: Wall 8 substantial yield photos

8.2.2. ***Nominal***

Dx = 1.08” (0.75%), Dy = +1.6” (1.11%), -Dy = -0.4” (-0.28%)

The nominal cycle at 0.75% drift marked reaching the yield plateau of the load-deformation curve in the X-direction, but no significant flattening in Y-direction. Significant softening of the wall specimen was observed in both directions. New inclined compressive and diagonal cracking was marked in the positive Dy cycle as well as the initiation of diagonal cracking in the negative Dy. Minor spalling was also observed on the Southeast corner boundary element where the concrete cover had been patched.

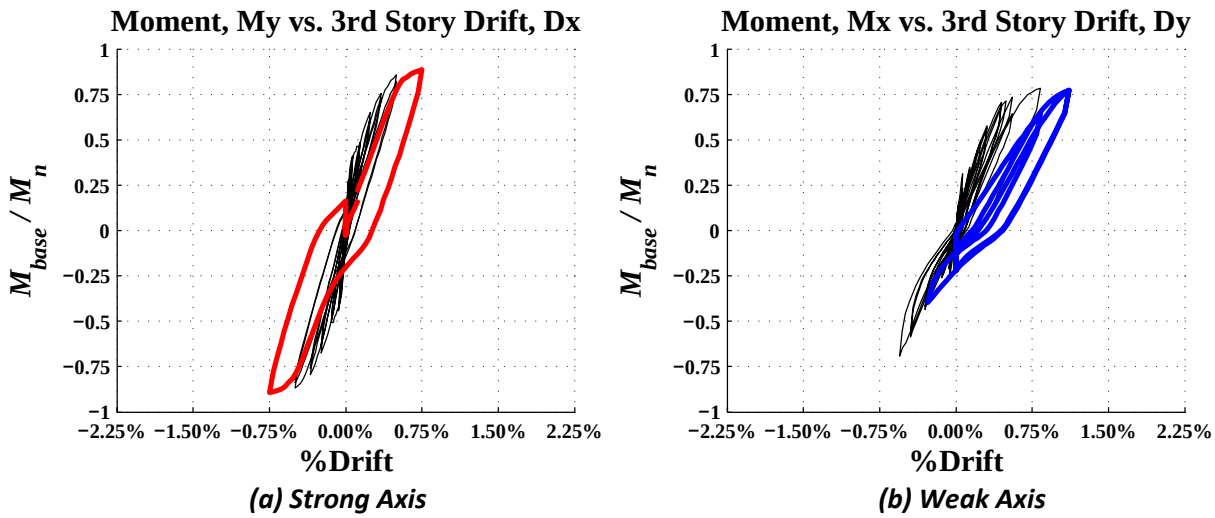

Figure 8.6: Wall 8 nominal hysteresis

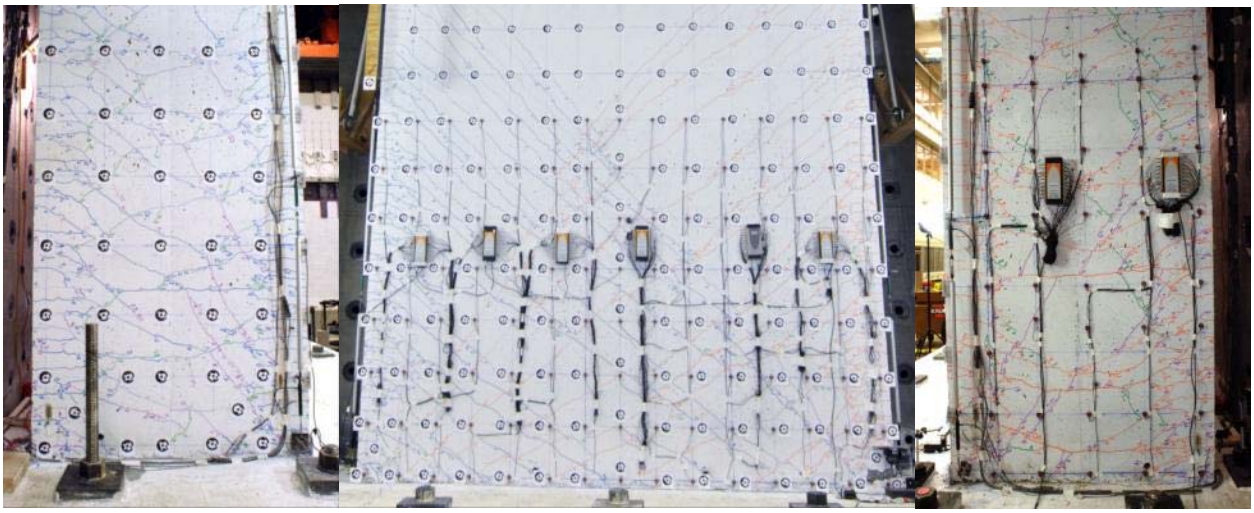

Figure 8.7: Wall 8 nominal photos

8.2.3. ***Significant spalling***

Dx = 2.16" (1.5%), Dy = +2.84" (1.9%), -Dy = -2.84" (-1.9%)

The X-direction cycle to 1.5% drift resulted in additional vertical splitting cracking proceeding into the corner regions of the wall and the onset of significant spalling in the corners and flanges. Similar to previous tests, the sliding of the web caused an out-of-plane shearing between the two boundary element regions on each flange resulting in spalling up the bottom two feet of each side. Bar buckling and rupture was observed in #2 rebar in the center of the web and the west flange.

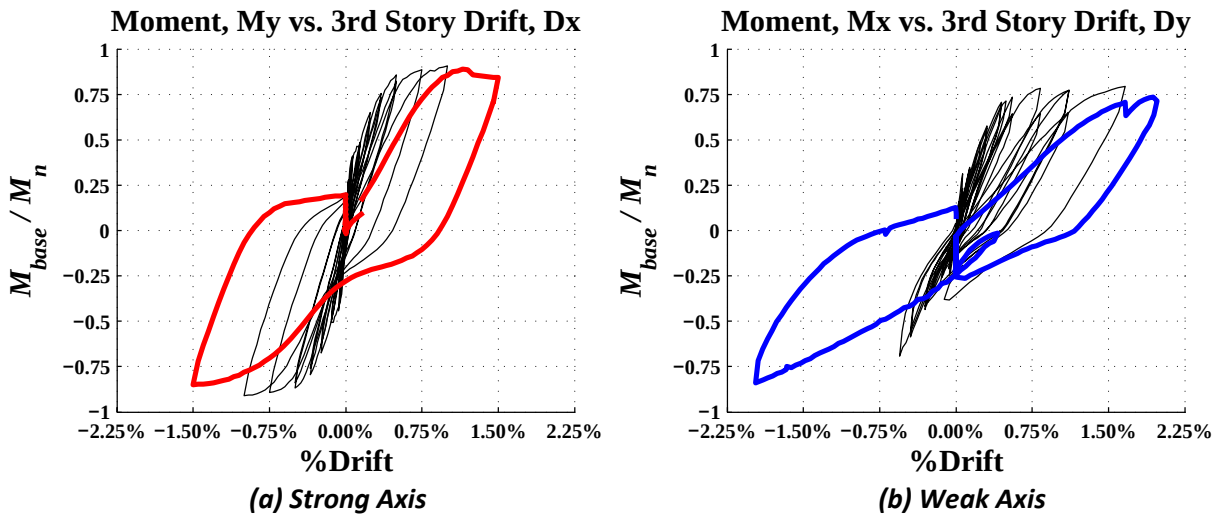

Figure 8.8: Wall 8 spalling hysteresis

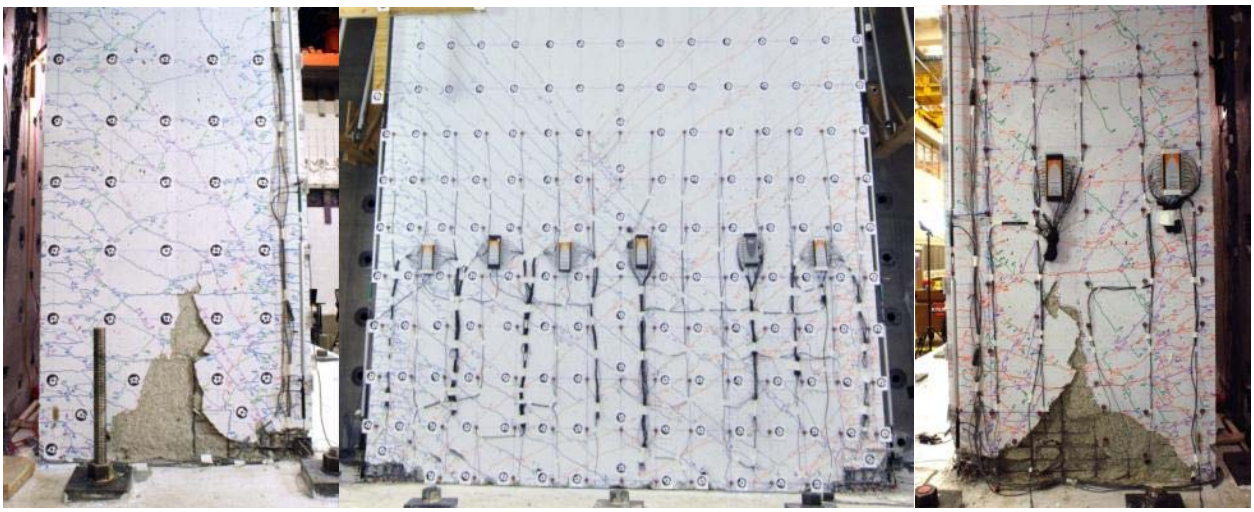

Figure 8.9: Wall 8 spalling photos

8.2.4. ***Bar buckling and Rupture***

Dx = 2.56" (1.78%), Dy = +2.84" (1.9%), -Dy = -2.84" (-1.9%)

The X-direction cycle to 1.8% drift resulted in additional out-of-plane shearing of the flanges with spalling extending over three feet from the base. Additional crushing and loss of confinement was observed in the corners. The cycles to 1.9% drift in Y resulted in spalling along the base of the web and the first spalling of the toe boundary elements. The first negative Y cycles resulted in one #4 rupture. The second negative Y cycle resulted in the rupture of approximately (10) #4 bars.

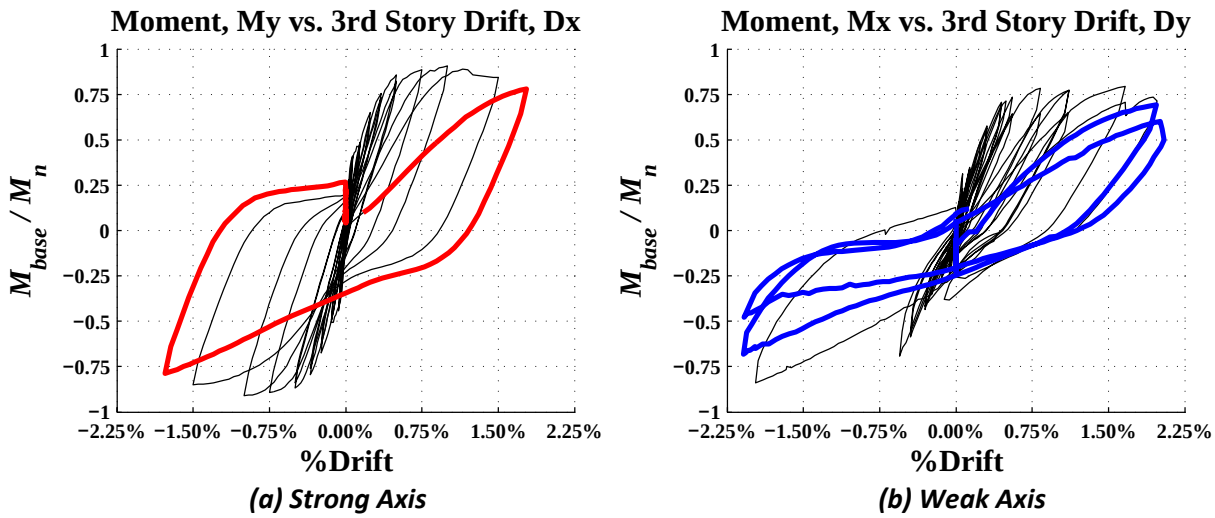

Figure 8.10: Wall 8 bar buckling and rupture hysteresis

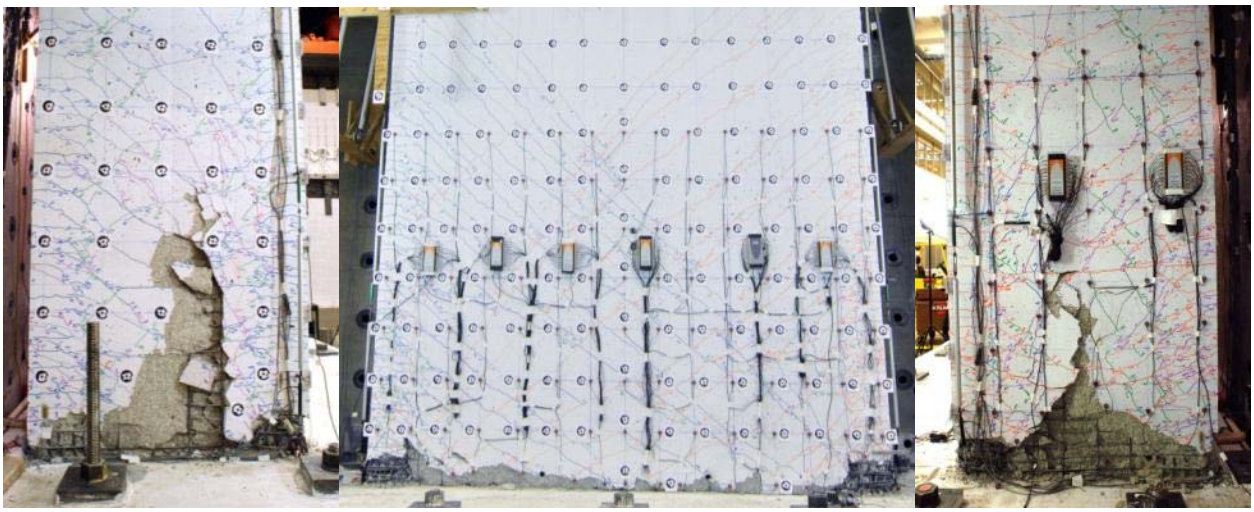

Figure 8.11: Wall 8 bar buckling and rupture photos

8.2.5. ***Failure***

Dy = +2.3" (1.62%), -Dy = -2.75" (-1.9%)

The final cycles in the positive Y direction were completed at a constant axial load of 1000 kips. The positive Y direction cycles resulted in widespread spalling along the face of the web and further loss of confinement and core crushing in the corner regions. In-plane shearing was observed in centers of both flanges causing further spalling and splitting up the height of the flange. The negative Dy cycle was completed with an axial tension of up to 250 kips. At -1.53% drift multiple #4 bars ruptured along the East flange and the specimen could no longer carry the full axial tension. The final positive cycle ended at 1.62% drift where the specimen exhibited a minor compressive failure dropping 133 kips of the axial load and 20 kips of shear.

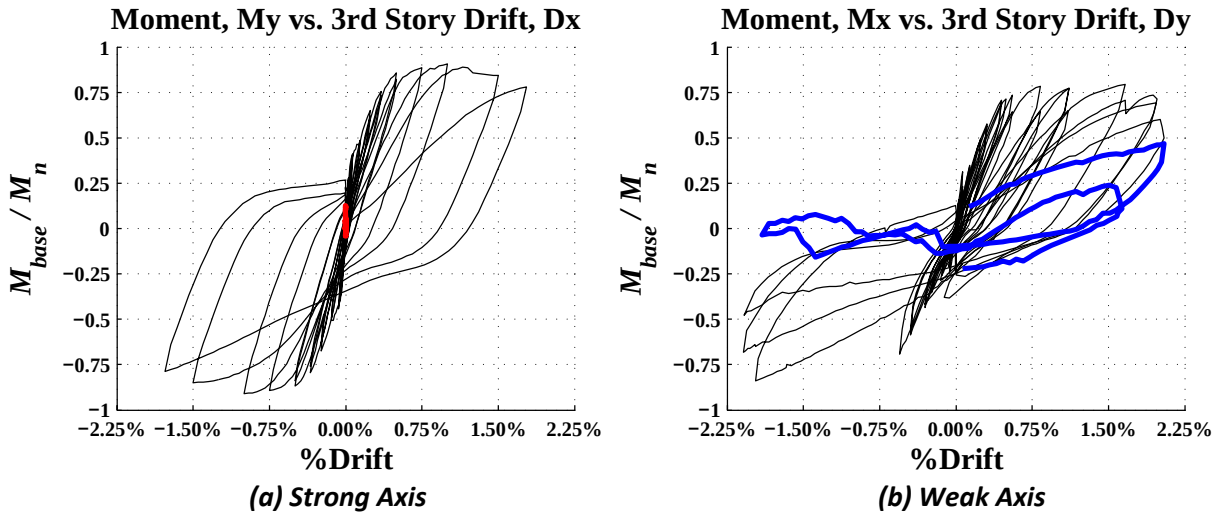

Figure 8.12: Wall 8 failure hysteresis

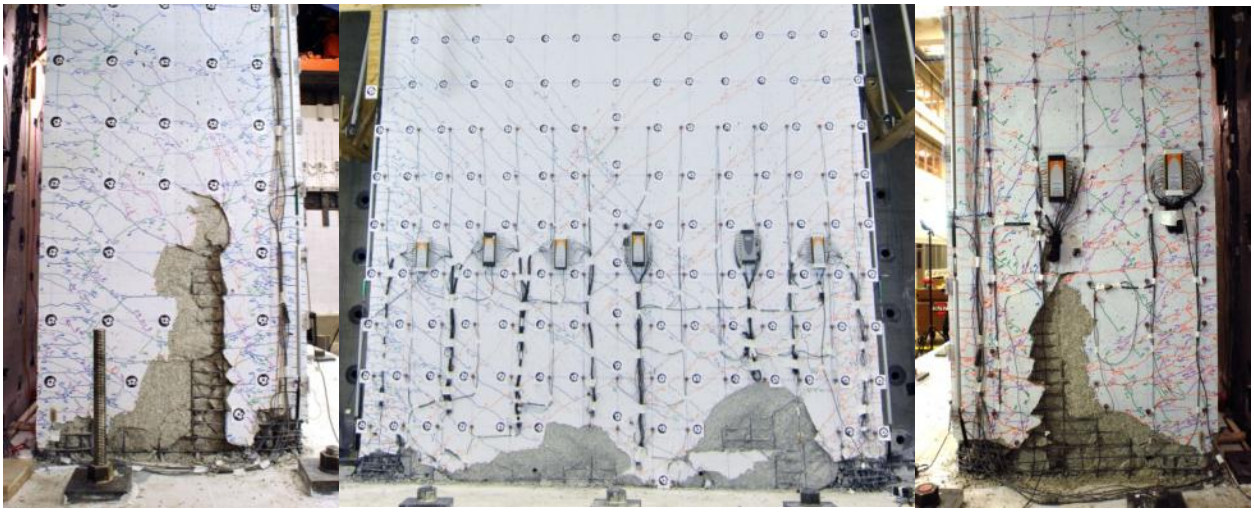

Figure 8.13: Wall 8 failure photos

9. Comparison of Experimental Results

In this section, the results of the three C-shaped wall tests are synthesized and compared. The common patterns of observed damages are identified. The demands and capacities for each wall in each loading direction are presented. The drift levels at initiation of critical damage states are tabulated. Last, a comparison of the global strong-axis response of the three tests is provided.

9.1. Damage comparison

The three wall specimens exhibited some similar damage and failure patterns with some distinct differences resulting from loading. These similarities in the observations can be grouped into three major damage types: deterioration of the boundary elements, effects of web sliding, and rupture of #2 bars accompanied by separation of the wall from footing. The loss of significant lateral loading in all

three tests was ultimately precipitated by rupture of the boundary element #4 bars even after the complete loss of confinement in the corner boundary elements.

9.1.1. *Boundary element damage*

For all of the test specimens, damage to the boundary elements at the end of the test was severe and included yielding and rupture of transverse reinforcement, crushing of cover and core concrete and buckling and rupture of primary, No. 4 longitudinal reinforcement. For all three test specimens, damage to the boundary elements at the ends of the flanges (the "toe" boundary elements) initiated at higher drift levels and was less severe than for corner boundary elements.

For corner boundary elements, compression damage initiated as vertical splitting cracks on both the web and flange faces. This damage pattern was followed by spalling of cover concrete and buckling of boundary element #4 bars. Cyclic action on the longitudinal bar resulted in bar buckling followed by straightening, which ultimately resulted in the permanent extension of the core confinement reinforcement and loss of confining action around the core. Slip and rupture of the boundary element hoops eventually ensued, as shown in Figure 9.1. For all three tests, the bottom one to two hoops in the corner boundary elements were ruptured at the end of the tests.

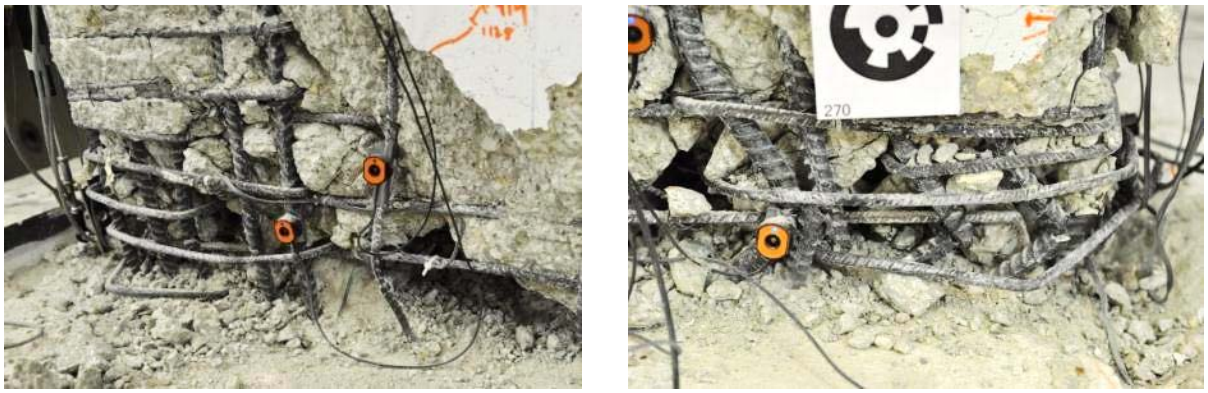

(a) Southwest corner *(b) Southeast corner*

Figure 9.1: Wall 7 ruptured and buckled bars in corner boundary elements

For all three tests, the *toe* boundary elements at the ends of the flanges were not as severely damaged as the corner boundary element. Though, at the end of all of the tests, compression damage to the boundary elements at the ends of the flanges included yielding of transverse reinforcement, crushing of core concrete, and buckling and rupture of #4 longitudinal reinforcement. Damage to the toe boundary elements was worst in the Wall 6 test; Figure 9.2 shows the toe boundary elements for Wall 6 at the end of the test. Figure 9.2(a) shows the four ruptured #4 bars in the boundary element at the toe of the west flange that resulted in loss of load carrying capacity for the specimen. Figure 9.2(b) shows the outward buckling of the #4 longitudinal reinforcement and crushing of core concrete in the boundary element at the toe of the east flange.

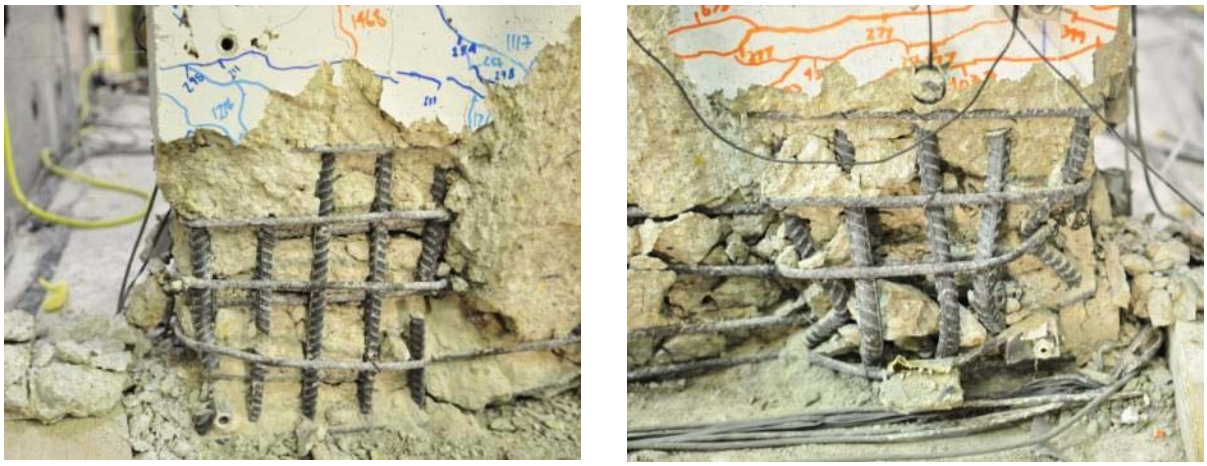

(a) West flange toe *(b) East flange toe*

Figure 9.2: Wall 6 ruptured and buckled bars in toe boundary elements

9.1.2. ***Rupture of #2 bars along the web and flanges***

For all three tests, the majority of longitudinal #2 bars in the web and flanges of the walls had ruptured at the footing and wall interface. Rupture of this reinforcement resulted in a large separation (i.e. wide crack) between the wall and footing. For the flanges, the separation between the wall and footing was most pronounced when the wall was subjected to displacement demands in the X-direction activating strong-axis bending; for Wall 7, measured separation of the East flange and footing exceeded one half inch (Figure 9.3(a)). For the web of the C-shaped walls, the separation between the wall and footing was most pronounced when the wall was subjected to displacement demands in the negative Y-direction. For Wall 8, displacement in the negative Y-direction was accompanied by application of a tensile axial loading and the separation between the wall and footing exceeded one inch (Figure 9.3(b)).

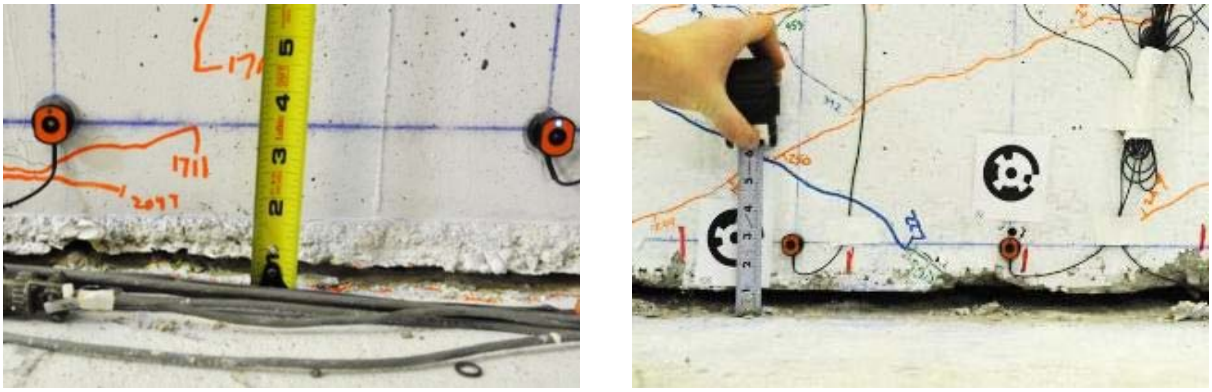

(a) Wall 7 East flange base separation *(b) Wall 8 web separation*

Figure 9.3: Interface separation at base

The rupture of the #2 longitudinal reinforcement was followed by outward buckling of the vertical and horizontal bars and cover spalling. However, for all of the tests, the interior concrete of the web remained largely intact throughout the test. For Wall 8, displacement in the positive Y-direction, which put the web of the C-shaped wall in compression, was accompanied by application of an axial load of up to 1000 kips. Even after core crushing and complete loss of confinement in the boundary elements, the largely intact web of Wall 8 was able to carry this large compressive load. A picture of Wall 8 near the

end of test (Figure 9.4) shows this. Pictures in Sections 7 and 8 show largely intact webs for Walls 6 and 7. For all of the tests, while the web of the wall remained largely intact, the interior of the flanges did not due to the out-of-plane shearing discussed in Section 9.1.3.

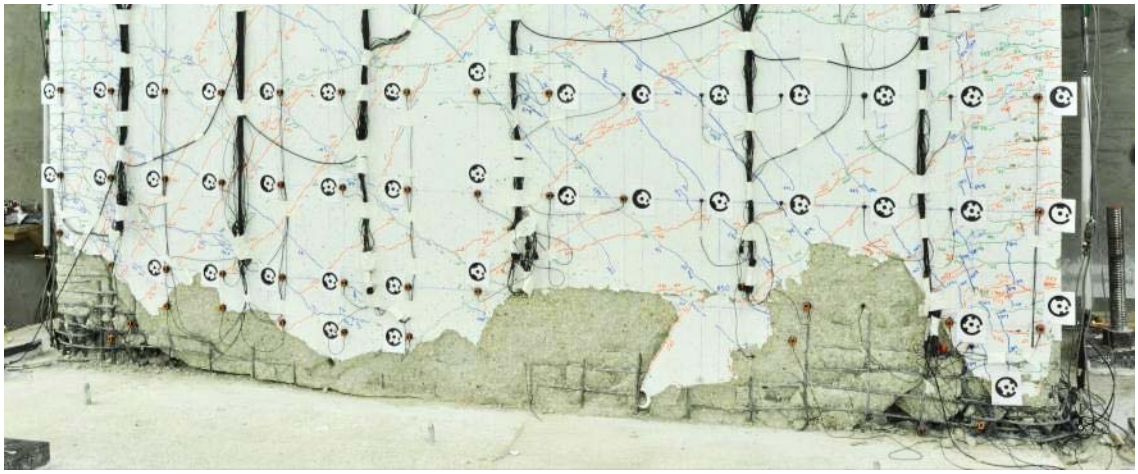

Figure 9.4: Wall 8 web

9.1.3. ***Web sliding***

For large displacement demands in the X-direction, once a large number of #2 longitudinal bars in the web of the wall had ruptured, sliding of the web represented a significant portion of total wall displacement. Rupture of the #2 longitudinal bars allowed the web to slide freely along the wall-footing interface. Three damage patterns were observed in all three tests as a consequence of the sliding: out-of-plane shearing of the flanges, dowel action of the boundary element longitudinal reinforcement, and separation between the corner boundary elements and the web.

Web sliding was resisted by the intact boundary element cores and dowel action of the #4 longitudinal bars in the boundary elements. During cycles in the X-direction, these #4 longitudinal bars could be seen to bend in the direction of loading.

Web sliding was also resisted by the toe boundary elements. However, this resulted in the flange carrying out-of-plane shear load. Ultimately, the flange could not support the out-of-plane shear that developed between the corner and toe, and cover spalling was observed along both flanges from the base of the wall to a height of two to three feet. Figure 9.5 shows spalling of the East flange for each test specimen near the end of the test; Figure 9.6 shows a close-up of the East flange of Wall 8. For all specimens, East and West flange damage was similar.

(a) Wall 6 *(b) Wall 7* *(c) Wall 8*

Figure 9.5: East flange damage attributed to out-of-plane movement

Figure 9.6: East flange damage attributed to out-of-plane movement in Wall 8

For each test, web sliding was also considered to result in separation between the corner boundary element and the interior of the web of the C-shaped wall. The larger drift demands employed in the unidirectional Wall 6 test exacerbated this separation resulting in a large inclined opening in the web and the rupturing of horizontal reinforcing across this interface as shown in Figure 9.7(a). The separation was also present in Wall 7 and 8 although not as pronounced as shown in Figure 9.7(b).

(a) Wall 6 *(b) Wall 8*

Figure 9.7: boundary element and web separation

9.2. Demand/Capacity Ratios

The shear and moment strengths were calculated per ACI 318-11 (ACI 2011) and compared with the maximum shear and moment applied to each C-shaped wall specimen. Given the geometry of the specimen, three capacities/demands can be compared: strong axis response (loading in the X-direction), weak axis response with toe in tension (loading in the positive Y-direction), and weak axis response with toe in compression (loading in the negative Y-direction). The comparison is tabulated in Table 9-1Table 9-3, Table 9-2, and Table 9-3 respectively.

Table 9-1: Strong axis demands and capacities

Specimen ID	ACI shear strength, V_n[A]	Max shear demand, V_{max}[A]	V_{max}/V_n	Design strength, M_n, k -ft (kN m)	Max moment, M_{base}, k -ft (kN m)	M_{base}/M_n
CW6	$5.8\sqrt{f'_c}A_g(0.48\sqrt{f'_c}A_g)$	$2.5\sqrt{f'_c}A_g(0.21\sqrt{f'_c}A_g)$	0.44	6414	6080	0.95
CW7	$5.6\sqrt{f'_c}A_g(0.47\sqrt{f'_c}A_g)$	$2.4\sqrt{f'_c}A_g(0.20\sqrt{f'_c}A_g)$	0.42	6426	5949	0.93
CW8	$5.7\sqrt{f'_c}A_g(0.47\sqrt{f'_c}A_g)$	$2.4\sqrt{f'_c}A_g(0.20\sqrt{f'_c}A_g)$	0.41	6421	5851	0.91

[A] Units: f'_c in psi (f'_c in MPa)

Table 9-2: Weak axis (+Y, toe in tension) demands and capacities

Specimen ID	ACI shear strength, V_n[A]	Max shear demand, V_{max}[A]	V_{max}/V_n	Design strength, M_n, k -ft (kN m)	Max moment, M_{base}, k -ft (kN m)	M_{base}/M_n
CW7	$4.9\sqrt{f'_c}A_g(0.41\sqrt{f'_c}A_g)$	$0.6\sqrt{f'_c}A_g(0.05\sqrt{f'_c}A_g)$	0.13	1733	1525	0.88
CW8	$5.0\sqrt{f'_c}A_g(0.42\sqrt{f'_c}A_g)$	$1.9\sqrt{f'_c}A_g(0.16\sqrt{f'_c}A_g)$	0.38	2048 [B]	1613 [B]	0.79 [B]

[A] Units: f'_c in psi (f'_c in MPa)

[B] Axial load = 746 kip compression

Table 9-3: Weak axis (-Y,toe in compression) demands and capacities

Specimen ID	ACI shear strength, V_n[A]	Max shear demand, V_{max}[A]	V_{max}/V_n	Design strength, M_n, k -ft (kN m)	Max moment, M_{base}, k -ft (kN m)	M_{base}/M_n
CW7	$4.9\sqrt{f'_c}A_g(0.41\sqrt{f'_c}A_g)$	$1.0\sqrt{f'_c}A_g(0.09\sqrt{f'_c}A_g)$	0.21	2538	2549	1.0
CW8	$5.0\sqrt{f'_c}A_g(0.42\sqrt{f'_c}A_g)$	$1.3\sqrt{f'_c}A_g(0.11\sqrt{f'_c}A_g)$	0.27	1717 [B]	1434 [B]	0.84 [B]

[A] Units: f'_c in psi (f'_c in MPa)

[B] Axial load = 114 kip tension

9.3. Damage State Comparison

The cracking response of the wall specimens for the strong and weak axis directions are presented below in Table 9-4. The drift at which flexural cracking was first observed is given in terms of drift of the 3-story specimen in conjunction with a ratio of the base moment demand to calculated cracking moment at this drift. For determination of the cracking moment, the tensile strength was taken as the sum of the concrete strength ($7.5\sqrt{f'_c}$ where f'_c is in psi ($0.63\sqrt{f'_c}$ where f'_c is in MPa)) and the quotient of axial load demand and transformed section area. The moment at which horizontal cracking was first observed was 0.3 to 0.8 of the calculated cracking moment. Diagonal cracking initiated at slightly larger drifts in the strong axis, while much larger drifts were required in the weak axis. A greater number of weak axis diagonal cracks was observed in Wall 8 due to the reduced point of inflection. The strong axis movements dictated the cracking and softening of the wall specimens. Relative to the strong axis, very little cracking was marked for the weak axis movements. The strong axis horizontal and diagonal cracks were observed to reopen when displacing about the weak axis.

Table 9-4: Cracking response of tests

State	Value	Strong Axis			Weak Axis (+Y, toe in tension)		Weak Axis (-Y, toe in compression)	
		CW6	CW7	CW8	CW7	CW8	CW7	CW8
Horizontal Cracks	Specimen Drift	0.02%	0.03%	0.02%	0.06%	0.05%	0.07%	0.07%
	M_b/M_{cr} [1]	0.31	0.54	0.39	0.81	0.82	0.39	0.52
Diagonal Cracks	Specimen Drift	0.10%	0.07%	0.07%	0.14%	0.22%	0.60%	0.42%
	$V_b/(A_g\sqrt{f'_c})$	1.09	1.04	1.06	0.23	1.12	0.85	0.59

Table 9-5 presents the drift at onset of damage states beyond initial cracking, including the initiation of cover spalling, exposed reinforcement, crushing of the confined boundary element core, reinforcement bar buckling, and reinforcement bar fracture in the boundary element. Bar slip and fracture of the longitudinal #2 bars in the web and flanges typically occurred without cover spalling and was difficult to confirm. Drift in Table 9-5 is defined as the drift at the top of the 3-story specimen. The drifts provide in Table 9-5 are the drifts at the first occurrence of each damage state in any of the three loading directions; the loading direction is provided.

Table 9-5: Damage response of tests

Damage State	Value	CW6	CW7	CW8
Cover Spalling	Drift	1.49% X	1.44% -Y	0.75% +Y [1]
Exposed Reinforcement	Drift	1.49% X	1% X and 2% +Y	1.50% +X
Bar buckling	Drift	1.49% X	2.25% +Y	1.50% +X
Core crushing	Drift	2.19% X	1.50% X	1.98% +Y
Boundary Element Bar fracture	Drift	2.19% X	2.50% X	1.64% -Y

[1] Spalling occurred in patched area

9.4. Envelope of loading comparison

The strong axis loading protocol was identical for the three tests allowing for a comparison of the influence of weak axis loading on the strong axis response. To compare the response of all three wall tests, an envelope of normalized base moment was produced using the maximum base moment achieved for each step of displacement and calculated nominal moment capacity for each test. The strong axis envelope shows nearly identical performance of the walls up to nominal capacity at 0.75% drift. The weak axis loading has no significant effect on the strong axis performance until post peak

where the ultimate ductility of the section was reduced. The plot of moment envelope for all three tests is given in Figure 9.8.

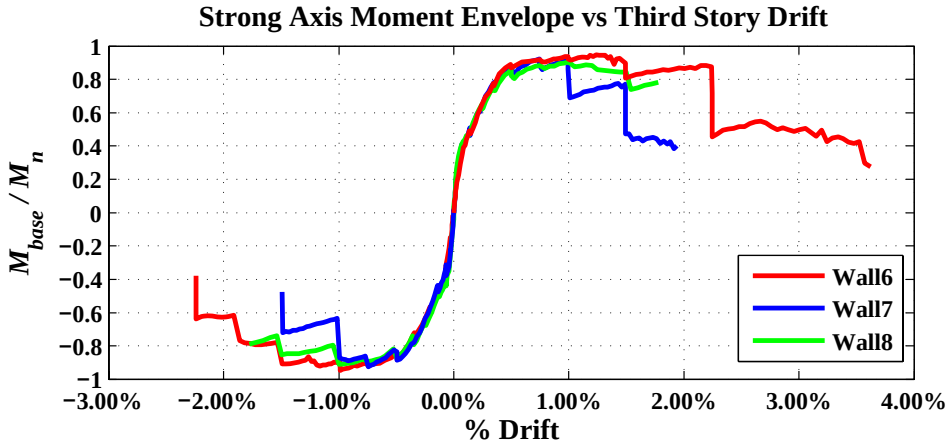

Figure 9.8: Strong axis moment envelope

10. Summary, Observations, and Future Work

10.1. Summary of Experimental Testing

Three nominally identical walls were subjected to quasi-static lateral loading and axial loading to investigate the impact on performance of bidirectional lateral loading and variable axial loading as well as to generate data for model calibration. A 10-story prototype core-wall system comprising two coupled C-shaped walls was designed using current code requirements. A 1/3-scale model of the bottom three stories of one C-shaped wall from this core-wall system was tested in the laboratory. Laboratory loading of the specimen was intended to represent demands in the bottom stories of the 10-story wall.

The three C-shaped specimens were tested as part of a larger experimental test program and are identified as Wall 6, Wall 7 and Wall 8. Wall 6, was subjected to constant axial load ($0.05f_cA_g$) and a unidirectional cyclic lateral displacement history in the direction of the web of the wall, activating strong-axis bending. Wall 7, was subjected to the same constant axial load ($0.05f_cA_g$) and a bidirectional cyclic lateral displacement history. For initial lateral displacement cycles, a cruciform displacement history was employed in which displacement demands in one direction were held at zero while a cyclic displacement history was imposed in the orthogonal direction. For later displacement cycles, displacement demands in the direction parallel to the wall flanges (activating weak-axis bending for the C-shaped wall) were held at the maximum allowed by laboratory equipment (-1.1% and +2.0% drift) and a cyclic displacement history was imposed in the orthogonal direction, activating strong-axis bending. Wall 8 was subjected to a cruciform displacement history in which displacement demands in one direction were held at zero while a cyclic displacement history was imposed in the orthogonal direction. For displacement cycles in the direction parallel to the web of the wall, activating strong-axis bending, a constant axial load of ($0.05f_cA_g$) was applied. For displacement cycles in the direction parallel to the flanges of the wall, axial load was varied from tension to compression to represent the load that could be expected in a C-shaped wall in a coupled core-wall system.

Extensive data were collected for each test. These data included applied loads, specimen displacement at various locations, displacement field data for the entire specimen, specimen deformations, and

concrete and steel reinforcement strains at various locations as well as still camera images and damage data.

10.2. Observations about C-shaped Wall Behavior

The experimental data presented in this document provide improved understanding of the behavior of C-shaped walls subjected to cyclic lateral loading as well as the impact of bidirectional versus unidirectional loading on this behavior.

Experimental data from the three C-shaped wall tests support the following observations about C-shaped walls behavior.

1. The response of a C-shaped wall depends on the direction of loading and the applied axial load. For lateral loading parallel to the web of the wall, activating strong-axis bending, the geometry and reinforcement are symmetric about the axis of bending. For constant axial load and a symmetric displacement history (i.e. positive and negative displacement demands are nominally identical), the progression of damage is approximately symmetric about the axis of bending. For lateral loading parallel to the flanges of the wall, activating weak-axis bending, the geometry and reinforcement are not symmetric about the axis of being. For constant axial load and a symmetric displacement history (i.e. positive and negative displacement demands are nominally identical), local strain demands at the extremes of the wall may be very different and damage accumulation may not be symmetric about the axis of bending. This is exacerbated when axial load varies as a function of loading direction.
2. For cyclic lateral loading applied using a cruciform displacement history, the wall maintained 80% of maximum lateral load carrying capacity to drift demands of approximately 1.5% for strong-axis bending and to drift demands in excess of 1.5% for weak axis bending. For cyclic lateral loading applied using a true bidirectional displacement pattern in which strong and weak axis bending were activated simultaneously, drift capacity was reduced, with wall CW7 exhibiting significant strength loss during cycling to -1.5% drift in the X-direction (strong-axis bending) while a drift demand of 2.0% was maintained in the Y-direction (weak axis bending).
3. For loading parallel to the web of the wall, activating strong-axis being, while crushing of boundary element confined concrete and buckling of boundary element longitudinal reinforcement contributed to strength loss, significant loss in lateral loading carrying capacity was primarily due to fracture of boundary element longitudinal reinforcement.
4. In all wall tests, yielding and rupture of web reinforcement resulted in significant sliding of the wall web at the wall-foundation interface; this sliding was resisted by dowel action of longitudinal reinforcement in the corner boundary elements and by out-of-plane response of the wall flanges.
5. Data from the three C-shaped wall tests show also that, in comparison with walls subjected to unidirectional lateral loading, C-shaped walls subjected to bidirectional loading have essentially the same flexural strength and exhibit essentially the same progression of damage. However walls subjected to bidirectional loading have a reduced stiffness, develop specific damage states at very different drift demands, and have different drift capacities than walls subjected to unidirectional lateral loading.
6. Although the walls were subjected to different displacement histories, the walls with constant axial load demands maintained an axial load of $0.05f'_cA_g$ and moderate lateral load carrying capacity (~40% of maximum strength) to relatively large drift demands (3.5% for Wall 6 and 2.0% for Wall 7).

7. For a severely damaged Wall 8, when axial load was increased to $0.15f_cA_g$ and the wall was subjected to weak axis bending, lateral strength dropped to approximately 10% of maximum strength.

Data in Table 9-1 show that the three wall specimens achieved approximately the same flexural strength for loading parallel to the web of the wall (strong-axis bending with constant axial load). Strong-axis flexural strength for the three specimens ranged from 91% to 95% of the nominal flexural strength as defined per ACI 318-11. The ACI 318 nominal flexural strength was computed using the assumptions provided in Chapter 9, including linear strain distribution along the length of the wall. The walls did not achieve this ideal flexural strength. Data in Table 9-1 and Table 9-3 show that for Walls 7 and 8, the maximum base moment under weak-axis bending ranged from the 79% to 100% of the ACI 318 nominal flexural strength. A review of the base moment versus drift history for Walls 7 and 8 (Figure 7.2 and Figure 8.3) suggests that the imposed displacement history may reduced the flexural strength of the wall when subjected to weak-weak axis bending ("toes" in compression).

Normalized base moment versus drift histories for the specimens (Figure 6.2, Figure 7.2 and Figure 8.3) show that bidirectional loading impacted the response for displacement cycles in excess of the yield displacement. At these displacement levels, bidirectional loading resulted in a significant reduction in the stiffness of the wall in the direction parallel to the web of the wall (loading activating strong-axis bending). That is for post-yield displacement cycles parallel to the web of the wall, the unloading-reloading stiffness of Wall 6 (unidirectional loading) was significantly larger than the unloading-reloading stiffness of Wall 7 or Wall 8 (bidirectional loading). This reduction in stiffness due to bidirectional loading is likely due to concrete damage and inelastic deformation of longitudinal reinforcement that occurs under weak-axis loading.

The drift capacity can be impacted in the weak axis. The base moment versus specimen drift histories (Figure 6.1, Figure 7.1, and Figure 8.1) suggest that drift capacity for strong axis bending is not significantly diminished under a cruciform-type displacement history (Wall 6 exhibited significant strength loss during cycling to 2% drift in the X-direction while Wall 8 did not exhibit significant strength loss during cycling to 1.75% drift in the X-direction) but is diminished by true bidirectional loading (Wall 7 exhibited significant strength loss during cycling to 1.5% drift in the X-direction while the Y-direction drift demand was held at 2%).

For the C-shaped walls tests, performance was characterized on the basis onset of (i) concrete cracking, spalling and crushing, (ii) steel reinforcement buckling and fracture, and (iii) loss of lateral load carrying capacity. Base moment versus drift plots (Figure 6.1, Figure 7.1, and Figure 8.1) and Table 9-4 and Table 9-5 show the drifts at which these damage states were first observed for each of the C-shaped wall specimens. These data show that the overall progression of damage under increasing displacement demands is essentially the same for all specimens although the occurrence is not. The damage progression is as follows: horizontal cracking of concrete, diagonal cracking of concrete, initial spalling of cover concrete, spalling of cover concrete exposing longitudinal reinforcement, buckling of boundary element reinforcement, crushing of boundary element confined concrete and fracture of boundary element longitudinal reinforcement.

These data also show, however, that with the exception of horizontal and diagonal cracking under strong-axis bending, the onset of concrete and steel damage states were entirely dependent on the imposed displacement history (unidirectional versus bidirectional). The stiffness of the wall specimens

vary substantially for different load directions and axial loads. In addition, maximum drift is not a good indicator of damage.

10.3. Future Work

The C-shaped wall tests provide substantial data characterizing wall performance under lateral loading. In the near term, it is expected that the data will be used as follows:

- Determine the contributions of flexure, shear, base rotation and base sliding to total wall deformation. The relative magnitudes of these contributions during the test provide insight into the mechanisms that control response. These data are also appropriate for use in calibrating and validating numerical models.
- Determine effective elastic flexural and shear stiffness at various during the test. Effective elastic stiffness values are used commonly in design. These data can be used to evaluate current recommendations for effective stiffness values for walls as well as to support development of new recommendations.
- Characterize demand at the onset of critical damage states with the objectives of identifying those demand parameters that are most highly correlated with onset of damage. It is expected that demand parameters to be considered will include local concrete and steel strains, rotation within a "hinge-region" at the base of the wall and story drift.
- Use displacement field data to generate strain field. Strain field data provide improved understanding of wall response; these data are also appropriate for use in calibrating and validating numerical models.

Ultimately, the experimental data will be combined with similar data from experimental tests of slender concrete walls conducted by others to accomplish the following:

- Characterize the impact of bi-directional loading on wall performance and identify the implications of this for design.
- Develop recommendations for effective flexural and shear stiffness for use in elastic analysis to support design.
- Evaluate nonlinear response models for walls, including fiber-type beam-column models and develop recommendations for using these walls to assess wall performance under wind and earthquake loading.
- Develop earthquake-damage prediction models, such as those included in ATC-58, for C-shaped walls subjected to unidirectional and bidirectional lateral loading.
- Make recommendations for design of slender walls to improve performance under earthquake loading.

11. Acknowledgements

The authors would like to acknowledge the contributions of UIUC graduate students Christopher Hart and Ken Marley. The authors would also like to acknowledge the contributions of Professor Emeritus Neil Hawkins, University of Illinois; Ron Klemencic and John Hooper of Magnusson Klemencic Associates, Seattle; Andrew Taylor of KPFF, Seattle and Joe Maffei of Rutherford & Chekene, San Francisco in advising the practical aspects of the research program.

The research presented herein was funded by the Charles Pankow Foundation and the National Science Foundation through the Network for Earthquake Engineering Simulation Research Program, Grant CMS-042157 and CMMI-0927178, Joy Pauschke, program manager. Any opinions, findings, and conclusions or recommendations expressed in this material are those of the authors and do not necessarily reflect the views of the Charles Pankow Foundation or the National Science Foundation.

12. References

ACI 318-11 Building Code Requirements for Structural Concrete and Commentary. American Concrete Institute, Committee 318. 2011, 503 pp.

Birely, A. (2012). "Seismic Performance of Slender Reinforced Concrete Structural Walls" *PhD Dissertation*. University of Washington.

Brown, P. Ji, J. Oyen, P, Sterns, A., Lehman, D., Lowes, L., Kuchma, D., Zhang, J. (2006). "Investigation of the Seismic Behavior and Analysis of Reinforced Concrete Structural Walls" *Proceedings of the Eight National Conference on Earthquake Engineering, April 18-22, San Francisco, CA.*

Harries, K. A. (2001). "Ductility and deformability of coupling beams in reinforced concrete coupled walls." *Earthquake Spectra*, EERI, 17(3):457-478.

Pugh, J. (2012). "Numerical Simulation of Walls and Seismic Design Recommendations for Walled Buildings." *PhD Dissertation*, University of Washington, Seattle.